

RICE UNIVERSITY

**Thermodynamic Stability and Phase Behavior of Asphaltenes in Oil and of
Other Highly Asymmetric Mixtures**

by

P. David Ting

A THESIS SUBMITTED
IN PARTIAL FULFILLMENT OF THE
REQUIREMENTS FOR THE DEGREE

Doctor of Philosophy

APPROVED, THESIS COMMITTEE:

Walter Chapman, Professor, Chair
Chemical Engineering

George Hirasaki, A.J.Hartsook Professor,
co-Chair
Chemical Engineering

Clarence Miller, Louis Calder Professor
Chemical Engineering

Matthias Heinkenschloss, Associate
Professor
Computational & Applied Mathematics

HOUSTON, TEXAS

MAY 2003

Copyright

P. David Ting

2003

ABSTRACT

Thermodynamic Stability and Phase Behavior of Asphaltenes in Oil
and of Other Highly Asymmetric Mixtures

by

P. David Ting

Asphaltenes are the polydisperse fraction of heavy organics from petroleum whose phase behavior is important in petroleum production and processing because of its potential to precipitate and plug tubulars.

The molecular framework used in this work is that van der Waals (dispersion) interactions dominate asphaltene phase behavior in oil. Using a proposed reservoir fluid fractionation method and an equation of state (EOS) asphaltene characterization method that requires only ambient condition titration data, the Statistical Associating Fluid Theory (SAFT) EOS was extended to model/predict asphaltene phase behavior in oil. Studies on model asphaltene systems (polystyrene-hexane, polystyrene-toluene-ethane, long-chain and short-chain n-alkanes, and phenanthrene-decane-methane mixtures) show that SAFT can describe the phase behavior of fluids dominated by molecular size and shape interactions.

Comparison between predicted and experimental asphaltene stability and oil bubble point curves of a recombined oil and a model live oil measured in this work show good agreement. The asphaltene stability and the bubble point measurements for the two oils were made under reservoir conditions as functions of pressure, temperature, and dissolved gas concentration. Both theory and experiment show significant temperature effects on asphaltene stability and the asphaltene instability onset pressures are nearly linear functions of dissolved gas concentration at each temperature. Furthermore, both SAFT-calculated and experiment derived mixture solubility parameters/refractive indices along the asphaltene instability curves are nearly constant at each temperature.

A SAFT investigation into the effects of asphaltene polydispersity shows that the lower molecular weight (MW) asphaltenes (including resins) play a significant role in stabilizing higher MW asphaltenes in oil, despite the inclusion of only dispersion interactions in the model. Resin's stabilizing effects on (polydisperse) asphaltene is greatest in the region of incipient asphaltene instability. In n-alkane titrations, SAFT shows that the heaviest asphaltenes will precipitate first, followed by the precipitation of smaller asphaltenes on further oil dilution. The ability to calculate changes in asphaltene MW distribution may be useful in deposition models.

DEDICATION

To my loving parents

For their unwavering support and their sound advice

ACKNOWLEDGEMENTS

I thank my parents and Christine for their love and support and my parents for instilling in me the discipline and work ethics that guided me through the worst times.

I am very grateful for the guidance and advice of Professors Walter Chapman and George Hirasaki, my two co-advisors. This work would have been impossible without their insights, their patience and their encouragements. I especially enjoyed the many Blimpie's and Wendy's runs with Dr. Chapman.

I thank the Chapman research group for their help and support, and am especially grateful for the friendships of Sharon Sauer, Prasanna Jog, and Auleen Ghosh. I would like to thank Steve Yang, Raymond Joe, and T-C Lee for their friendship and for many fruitful discussions on a variety of topics from critical scaling to surface physics.

I am grateful to the many people that made my stay here so enjoyable. These include: Rebecca Daprato, Ming He, Elizabeth Hedberg, Erik Hughes, Johnna Temenoff, and Heidi Thornquist.

I would like to thank our collaborators at New Mexico Institute of Mining and Technology, especially Jill Buckley and Jianxin Wang, for fruitful discussions

on asphaltenes and for providing us with valuable experimental data. I also like to thank Ahmed Hamammi, John Ratulowski, Kunal Karan, and Kurt Schmidt of DB Robinson and Nancy Burke and Jeff Creek of ChevronTexaco for many discussions concerning my thesis research. The experimental portion of this thesis would have been impossible without the equipment and support of the people in these organizations. I especially enjoyed the company of Kunal and Kurt in the brew pubs of Edmonton.

I gratefully acknowledge the Department of Energy, DeepStar, ChevronTexaco, DB Robinson, and the Consortium of Processes in Porous Media at Rice University for their financial support. The financial, equipment, and technical supports of ChevronTexaco and DB Robinson were especially valuable.

TABLE OF CONTENTS

CHAPTER 1. INTRODUCTION	1
CHAPTER 2. BACKGROUND INFORMATION	4
2.1 Physical Properties and Characteristics of Asphaltenes	4
2.2 Economic Significance	9
2.3 The Phase Behavior of Asphaltenes in Crude Oil	10
2.4 Our Hypothesis	13
2.5 Asphaltene Thermodynamic Models	15
2.5.1 Classical Thermodynamic Models	16
2.5.2 Colloidal Models	19
CHAPTER 3. EXPERIMENTS OF ASPHALTENE STABILITY	23
3.1 Introduction	23
3.2 Experimental	26
3.2.1 Stock Tank Oil Properties	26
3.2.2 Model Oil Preparation	28
3.2.3 Recombined Oil Preparation	29
3.2.4 High Pressure and Temperature Apparatus	29
3.2.5 Procedure	31
3.3 Results	34

3.4 Discussions	38
3.5 Summary	45
CHAPTER 4. EQUATION OF STATE ALGORITHMS	47
4.1 Introduction	47
4.2 The SAFT Equation of State	48
4.3 Reference State Conversions	57
4.4 SAFT Equation of State Parameters	58
4.5 Phase Stability and Flash Algorithm	62
CHAPTER 5. APPLICATION OF SAFT TO MODEL SYSTEMS	77
5.1 Introduction	77
5.2 Long-Chain Short-Chain Alkane Mixtures	78
5.2.1 Background Information	78
5.2.2 Results and Discussions	82
5.2.3 Section Summary	87
5.3 Polystyrene-Solvent/Precipitant Mixtures	88
5.3.1 Background Information	88
5.3.2 Results and Discussions	89
5.3.3 Section Summary	97
5.4 Phenanthrene-Solvent/Precipitant Mixtures	98
5.4.1 Background Information	98
5.4.2 Results and Discussions	99

5.4.3 Section Summary	102
CHAPTER 6. MODELING OF ASPHALTENE PHASE BEHAVIOR	103
6.1 Introduction	103
6.2 Model Oil Investigations	104
6.2.1 Determination of Asphaltene SAFT Parameters	104
6.2.2 Comparison of Predicted and Measured Asphaltene Instability Onsets	110
6.3 Recombined Oil Investigations	113
6.3.1 Separator Gas Characterization	114
6.3.2 Stock-Tank Oil Characterization	115
6.3.3 Recombined Oil Properties	127
6.3.4 Comparison of Predicted and Measured Asphaltene Instability Onsets	130
6.4 Summary	131
CHAPTER 7. ASPHALTENE SAFT PARAMETER SELECTION RULES ..	133
7.1 Introduction	133
7.2 Effects of Variations in SAFT Parameters on Solubility Parameter	133
7.3 Effects of Variations in SAFT Parameters on Molar Volume	135
7.4 Effects of Variations in Asphaltene SAFT Parameters on Mixture Composition at Asphaltene Instability Onset	136

7.5 Uniqueness of the Asphaltene SAFT Parameters	140
7.6 Summary	143
CHAPTER 8. EFFECTS OF ASPHALTENE POLYDISPERSITY	
(INCLUDING RESIN ADDITION)	146
8.1 Introduction	146
8.2 Selection of SAFT Parameters for Polydisperse Asphaltenes & Resins	147
8.3 Effects of Asphaltene Polydispersity and Resin Addition	155
8.4 Summary	161
CHAPTER 9. REFORMULATION OF THE SAFT DISPERSION TERM	
FOR POLYDISPERSITY	163
9.1 Introduction	163
9.2 Algorithm Extension	164
CHAPTER 10. MODIFICATIONS TO THE SAFT ASSOCIATION TERM –	
IMPLICATIONS TO MIXTURES CONTAINING WATER ...	172
10.1 Introduction	172
10.2 Theory Modifications	175
CHAPTER 11. CONCLUSIONS AND FUTURE RESEARCH	186

REFERENCES 193

LIST OF TABLES

CHAPTER 3

Table 3.1	Properties of the oil samples used in this study.	24
Table 3.2	Precipitant volume fractions ($\phi_{\text{ppt}}^{\text{V}}$) and mixture refractive indices (P_{RI}) at the onset of asphaltene instability for the stock-tank oil mixture and the model oil.	24
Table 3.3	Stock-tank oil and separator gas compositions.	27
Table 3.4	Asphaltene instability onset and bubble point pressures of the model live oil.	34
Table 3.5	Asphaltene instability onset and bubble point pressures of the recombined oil.	36
Table 3.6	Comparison of molar refractions of some compounds of interest calculated using measured refractive indices and densities and using group contribution method.	40

CHAPTER 4

Table 4.1	SAFT pure component parameters.	58
Table 4.2	SAFT pure component parameters correlations.	61
Table 4.3	Comparison of flash algorithms on some nonideal systems.	73

CHAPTER 5

Table 5.1	Experimentally obtained and regressed pure component parameters for the Peng-Robinson and SAFT equations.	83
Table 5.2	Optimum binary interaction parameters for the tested EOS and average absolute percent deviations between experimental and calculated phase compositions.	84
Table 5.3	Average absolute percent deviations between experimental and predicted phase compositions for SAFT with $k_{ij} = 0$.	87
Table 5.4	SAFT parameters used to model polystyrene phase behavior.	90
Table 5.5	Select solid, solid-solid, and solid-liquid phase transition properties of pure phenanthrene.	100
Table 5.6	Pressure-solubility behavior of phenanthrene in toluene at 293K.	102

CHAPTER 6

Table 6.1	Composition of the separator gas and the pseudo-component SAFT parameters.	115
Table 6.2	Binary interaction parameters for the separator gas sub-fractions.	115
Table 6.3	Estimated compositions of each stock-tank oil sub-	118

fraction.

Table 6.4	SAFT parameters for the non-asphaltene stock-tank oil pseudo-components.	119
Table 6.5	SAFT parameter correlations for the saturates and aromatics+resins oil sub-fractions.	121
Table 6.6	Binary interaction parameters used to fit the stock-tank oil asphaltenes in SAFT.	125
Table 6.7	Comparison of stock-tank oil SAFT asphaltene parameters and the n-C ₇ insoluble model oil SAFT asphaltene parameters.	126
Table 6.8	Binary interaction parameters between pseudo-component species in SAFT.	128
CHAPTER 8		
Table 8.1	SAFT Parameters for the various asphaltene sub-fractions (including resins).	152
Table 8.2	Oil and asphaltene properties of four representative model oils tested to study the effects of asphaltene polydispersity and resin addition.	157

LIST OF FIGURES

CHAPTER 2

- Figure 2.1 Fractionation of stock-tank oil into saturates, aromatics, resins, and asphaltenes according to the ASTM D2007-80 method. 5
- Figure 2.2 Relationship between crude oil sub-fractions and coke. The polydisperse nature of petroleum asphaltenes is also shown. 6
- Figure 2.3 One group's proposed structures of asphaltene molecules. 6

CHAPTER 3

- Figure 3.1 P_{RI} and ϕ_{ppt}^V at asphaltene instability onsets for the model oil and the stock tank oil mixture as a function of the square root of the precipitant molar volume ($v_p^{1/2}$) at 20°C. 25
- Figure 3.2 Diagram of the DB Robinson PVT apparatus used in this study. 31
- Figure 3.3 The onset of asphaltene instability for the model oil at 65.5°C as detected by the light transmittance apparatus. 32
- Figure 3.4 Experimental procedure used in the high pressures asphaltene instability studies. 33

Figure 3.5	(a) Asphaltene instability onsets and bubble points for the model live oil at 20.0°C and 65.5°C. (b) Asphaltene instability onsets and bubble points for the recombined oil at 71.1°C.	35
Figure 3.6	Comparison of asphaltene instability onsets and bubble points for model oil at 65.5°C and recombined oil at 71.1°C.	37
Figure 3.7	Effects of pressure on mass density for (a) model live oil at 20.0°C and 65.5°C and (b) recombined oils.	38
Figure 3.8	Mixture refractive indices on the asphaltene instability boundaries (P_{RI}) for model oil at 20.0°C, model oil at 65.5°C, and recombined oil at 71.1°C.	42
Figure 3.9	Measured P_{RI} vs. $v_p^{1/2}$ of n-alkane titrants for the model oil and calculated P_{RI} vs. $v_p^{1/2}$ of methane for the model live oil at 20.0°C.	43
Figure 3.10	Mixture refractive indices during pressure depletion for the model live oil at 20.0°C with 0.143 mass fraction methane above the bubble point. Asphaltenes are unstable below the asphaltene instability line.	45
CHAPTER 4		
Figure 4.1	Assumptions and limitations of the SAFT EOS.	50
Figure 4.2	In SAFT, fluids are initially considered to be a mixture of independent segments that are then bonded to form	51

chains.

Figure 4.3	Comparison of SAFT-predicted compressibility factor Z as a function of packing fraction η with simulation results.	53
Figure 4.4	Comparison of SAFT-predicted and experimental solubility parameters at 25°C and 1 bar.	56
Figure 4.5	Comparison of SAFT-predicted, Peng-Robinson EOS-predicted, and experimental liquid molar volumes at 1 bar.	56
Figure 4.6	Plots of SAFT pure component parameters with molecular weight.	61
Figure 4.7	Variation of m with molecular weight for various compounds.	62
Figure 4.8	Calculation procedure in a typical TP flash algorithm.	65
Figure 4.9	Change in the Gibbs energy of mixing for a binary mixture at various pressures and compositions. The pressure-composition diagram is given on the left and the energy-composition diagrams for various pressure cuts on the right.	67
Figure 4.10	Proposed phase equilibria calculation procedure.	70
Figure 4.11	Illustration of the tangent plane distance approach to determine phase stability.	75

CHAPTER 5

- Figure 5.1 Peng-Robinson fits to C_6-C_{16} , C_6-C_{24} , and C_6-C_{36} mixture phase equilibria data at 622 K or 623 K. The vapor compositions are expanded on the right and the mixture critical points are filled. 85
- Figure 5.2 SAFT fits to C_6-C_{16} , C_6-C_{24} , and C_6-C_{36} mixture phase equilibria data at 622 K or 623 K. The vapor compositions are expanded on the right and the mixture critical points are filled. 85
- Figure 5.3 Experiment and SAFT-predicted cloud point pressures for 4% polystyrene solution in n-hexane. The molecular weights of the polystyrene range from 8,000 to 50,000. 90
- Figure 5.4 Experiment and SAFT-predicted cloud point pressures for 8,000 MW polystyrene in n-hexane. The mass composition of polystyrene range from 1% to 8%. 91
- Figure 5.5 Experiment and SAFT-predicted polystyrene-ethane-toluene phase diagram at 343K and 62 bar or 117.2 bar. 94
- Figure 5.6 SAFT-predicted polystyrene-ethane-toluene phase diagram at 500 K and 300 or 500 bar. 95
- Figure 5.7 Experiment and SAFT-predicted pressure-temperature diagrams for the system polystyrene-ethane-toluene with 17.8% mass ethane (78.3% mass toluene) and 97

with 22.5% mass ethane (73.8% mass toluene).

Figure 5.8	Experiment and SAFT+solid fugacity model-calculated solid-liquid-vapor equilibria for the system phenanthrene-decane-methane at various pressures and temperatures.	101
CHAPTER 6		
Figure 6.1	Asphaltene SAFT parameters fitting procedure.	107
Figure 6.2	SAFT fits to model oil asphaltene aggregates P_{RI} and volume fraction precipitants data.	109
Figure 6.3	Ternary phase diagram at 20°C and 1 bar for a mixture of asphaltene, toluene, and n-pentane.	110
Figure 6.4	Experimental and SAFT-predicted asphaltene instability onsets and bubble points for the model oil at 20.0°C and 65.5°C.	111
Figure 6.5	Calculated refractive index and SAFT calculated mixture solubility parameter during pressure depletion for the model live oil at 20.0°C with 0.143 mass fraction methane above the bubble point. Asphaltenes are unstable below the asphaltene instability line.	113
Figure 6.6	Molecular weight distribution of the C_{10+} saturates.	117
Figure 6.7	Comparison of SAFT-calculated densities for the mixture of saturates using the one-fluid treatment and the 26-components treatment.	120

Figure 6.8	Relationship between solubility parameter (at 25°C) and refractive index (at 20°C) for some select compounds.	124
Figure 6.9	SAFT fits to stock-tank oil asphaltene aggregates P_{RI} data.	126
Figure 6.10	Experimental and SAFT-predicted one-phase recombined oil densities with two different gas-oil ratios.	129
Figure 6.11	Comparison of SAFT-predicted and measured bubble points for the recombined oils	130
Figure 6.12	SAFT-predicted and measured asphaltene instability onset and mixture bubble points for the recombined oil at 71.1°C.	131
CHAPTER 7		
Figure 7.1	Effects of variations in m , σ , and ϵ/k on the calculated solubility parameters at 20°C and 1 bar.	134
Figure 7.2	Effects of variations in m , σ , and ϵ/k on calculated molar volumes at 20°C and 1 bar. All else being equal, molecules with lower ϵ/k have larger molar volumes.	136
Figure 7.3	Effects of changing (a) m , (b) ϵ/k , and (c) σ for asphaltenes on the amount of n-alkane precipitants needed to induce asphaltene instability in the	137

asphaltene-toluene-n-alkane mixtures.

Figure 7.4	Effects of m and ϵ/k for asphaltenes on calculated volume fraction of precipitants at the onset of asphaltene instability at 20°C and 1 bar.	140
Figure 7.5	Calculated precipitant volume fractions at asphaltene instability onset using different sets of asphaltene SAFT parameters. $m = 54$ in all cases.	141
Figure 7.6	ϵ/k vs. σ for six sets of asphaltene SAFT parameters ($m=54$ in all cases). Different sets of SAFT parameters that give similar ϕ_v^{ppt} vs. n-alkane carbon number curves are connected by lines.	142
Figure 7.7	Asphaltene-toluene-n-heptane ternary phase diagram for two different asphaltenes that give similar ϕ_v^{ppt} vs. n-alkane carbon number curves at 20°C and 1 bar.	143
CHAPTER 8		
Figure 8.1	Fitting procedure for polydisperse asphaltenes with polydispersity captured using three asphaltene pseudo-components.	150
Figure 8.2	Comparison of SAFT and measured precipitant volume fraction and mixture refractive index at asphaltene instability onset for Lagrave asphaltene-toluene-n-alkane mixtures at 20°C and 1 bar. The initial asphaltene/toluene ratio is 1g/100mL.	151

Figure 8.3	Comparison of SAFT and experimental mass distribution of each asphaltene sub-fraction in Lagrave asphaltenes.	153
Figure 8.4	Plot of ϵ/k vs. m for the various SAFT asphaltene sub-fractions and resin.	155
Figure 8.5	Solubility of monodisperse asphaltenes in model Lagrave oil (7.5g asphaltenes/100mL toluene) mixed with n-alkanes at 20°C and 1 bar.	158
Figure 8.6	Solubility of polydisperse asphaltenes (with or without resins) in model Lagrave oil (7.5g total asphaltenes/100mL toluene) mixed with n-alkanes at 20°C and 1 bar.	159
Figure 8.7	Normalized distributions of the asphaltene sub-fractions in the precipitated phase as a function of volume fraction precipitant in the model oil mixtures.	161
CHAPTER 10		
Figure 10.1	Intermolecular potential model for molecules with square-well sites with angular cutoffs.	177
Figure 10.2	The hard spheres + association model of water used in this work can qualitatively describe the local structure of bulk water.	178
Figure 10.3	Comparison of the pair correlation functions obtained from different methods at a reduced density of 0.39 ($\eta=0.2042$).	182

CHAPTER 1. INTRODUCTION

The ability to model the thermodynamic phase behavior of mixtures with large disparities in molecular size and/or shape dominated by nonpolar dispersion interactions is of considerable interest because of the large number of industrial processes associated with the mixing and separation of these mixtures. While the reader can probably think of a few polymer systems as examples of mixtures with large size/shape disparities, it is not often that one will associate asphaltenes in crude oil as an example in this category. However, asphaltene phase behavior in crude oil is an important area of research because crude oil is the feedstock to most petrochemical processes and asphaltenes are one of the main culprits behind production and transportation delays. The main focus of this work is to model and predict the phase behavior of asphaltenes in crude oil under ambient and reservoir conditions using a statistical mechanical perturbation theory called SAFT (the Statistical Associating Fluid Theory).

This study contains an experimental and a theoretical component. In the experimental work (Chapter 3), asphaltene stability boundaries of a model live oil and a recombined oil were measured under reservoir conditions as functions of pressure, temperature, and dissolved gas concentration. While much had been reported on asphaltene stability, most of the studies reported in literature were performed under ambient conditions. In the theoretical work, an algorithm that is both robust and efficient was developed (Chapter 4) to calculate phase

equilibrium compositions. Using a proposed reservoir fluid fractionation method and a monodisperse SAFT asphaltene characterization method that requires only ambient condition titration data, SAFT-predicted asphaltene phase stability boundaries were compared with experimental data in Chapter 6. In Chapter 7, the sensitivity and the uniqueness of the fitted SAFT asphaltene parameters were investigated and a set of asphaltene parameter selection guidelines was formulated. Since asphaltene exists in nature as a polydisperse mixture of structurally related molecules, an analysis of the effects of resins (which are essentially the lowest molecular weight asphaltenes) and asphaltene polydispersity on SAFT-calculated asphaltene phase behavior in oil is given in Chapter 8. In Chapter 9, we reformulated the various terms in SAFT so that the equation of state can more robustly and efficiently account for molecular polydispersity. Finally, in Chapter 10, a more rigorous implementation of the SAFT equation of state was introduced to improve SAFT's ability to model systems containing water and hydrocarbons.

As the title suggests, a considerable amount of work in this thesis (Chapter 5) deals with other systems with large disparities in molecular size and shape. One goal of these investigations is to show that SAFT can be used to describe the phase behavior of a variety of systems with large size/shape discrepancies dominated by nonpolar dispersion interactions. The other, more important, reason for these investigations is to show the reader the connection between asphaltene and polymer phase behaviors; many "peculiar" behaviors of

asphaltenes in oil can be described in terms of the much better understood polymer thermodynamics.

CHAPTER 2. BACKGROUND INFORMATION

2.1 Physical Properties and Characteristics of Asphaltenes

The study of the heavy fractions of petroleum known as asphaltenes and resins first garnered interests in the 1930s when it was realized that asphaltenes are widely distributed throughout nature. They are found in native asphalts, crude oil, bitumen, tar mats, and in dispersed organic matters in sediments. Coined in 1837 by Boussingault,^[1] asphaltene was used to describe the black, alcohol-insoluble and essence of turpentine-soluble material from crude oil distillation residues. In modern operations, its definition evolved to loosely describe the fraction of heavy organics from carbonaceous sources such as petroleum, coal, and shale oil that is insoluble in low molecular weight n-paraffins and soluble in aromatic solvents such as benzene and toluene.^[2]

The currently accepted definition of asphaltenes is an operational one based on solubility (Figure 2.1). As such, it reveals little about the structure of asphaltenes. Considering that oil can contain 100,000+ different molecules^[3], the exact structural definition may never be known. However, most researchers agree that asphaltenes are a polydisperse mixture of molecules containing polynuclear aromatics, aliphatics, and alicyclic moieties with small amounts of dispersed heteroelements such as oxygen, sulfur, vanadium, and nitrogen. Furthermore, asphaltenes are the heaviest fraction of a distribution (in molecular

weight and aromaticity) of compounds that include aromatics and resins in the lower molecular weight sub-fractions. The accepted definition for asphaltenes is, in essence, an arbitrarily divided sub-fraction of this distribution. The relationship between asphaltenes and other classes of compounds in oil is shown in Figure 2.2. As shown in the figure, asphaltenes are more aromatic (low weight percent hydrogen) than the other oil fractions, are larger in molecular weight, and have higher solubility parameters. In terms of solubility, resins are often defined as the propane-insoluble and heptane- and toluene-soluble fraction of the crude oil. Figure 2.3 shows one set of proposed structures for asphaltene molecules; there is considerable disagreement on the size and the degree of aromaticity of these molecules in literature.

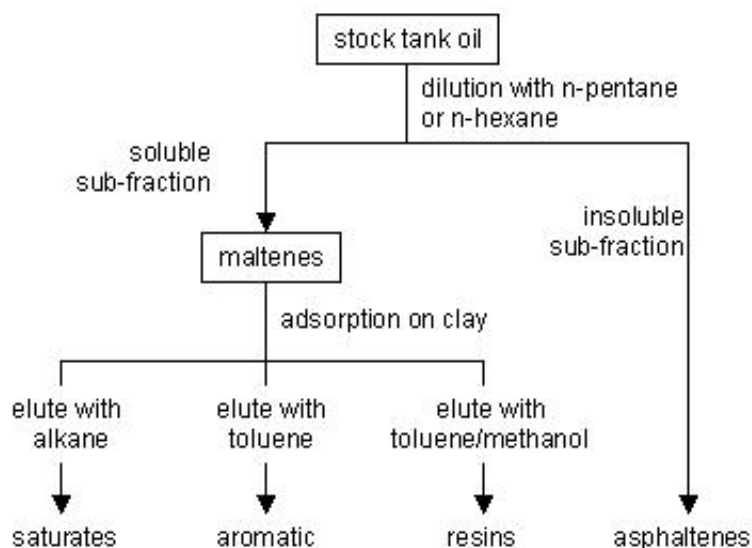


Figure 2.1 Fractionation of stock-tank oil into saturates, aromatics, resins, and asphaltenes according to the ASTM D2007-80 method^[4]. The figure is reproduced from Wang^[5].

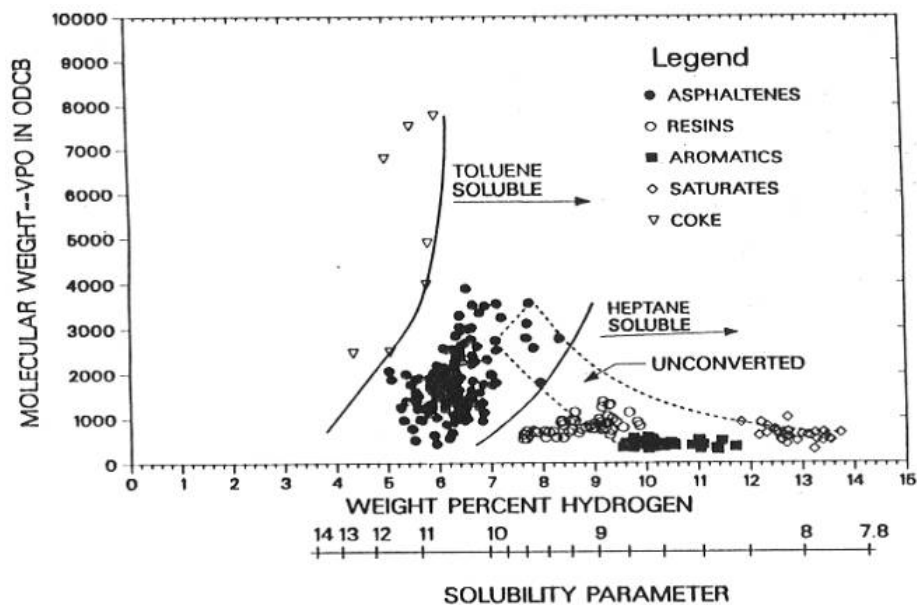


Figure 2.2 Relationship between crude oil sub-fractions and coke from Wiehe and Liang.^[3] The solubility parameter in the figure is given in units of $(\text{calories}/\text{cm}^3)^{1/2}$.

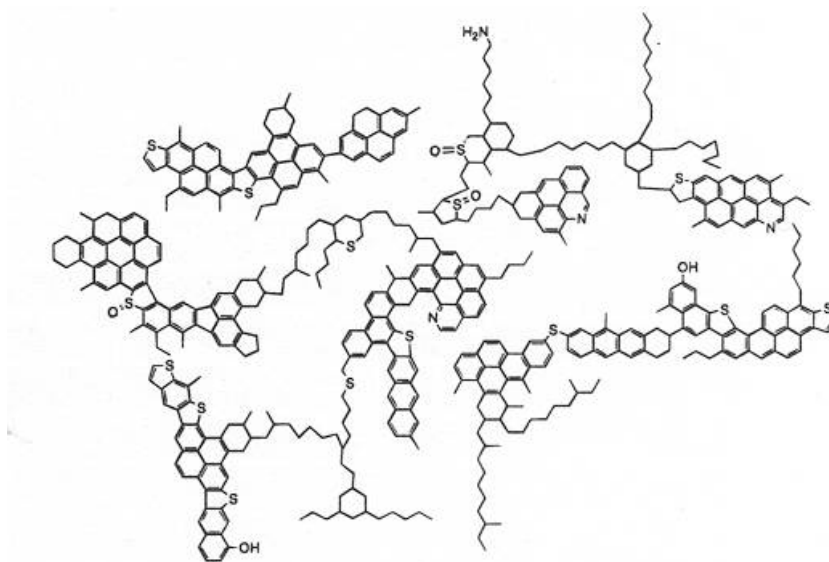


Figure 2.3 One group's proposed structures of asphaltene molecules.^[6]

Unlike other crude oil components, asphaltenes are unique because they have a strong tendency to self-aggregate with changes in temperature, pressure, or mixture composition. Hence, the extent of aggregation may differ depending

on the solvent used in the analyses to determine molecular weights and structures. This (together with asphaltene's polydispersity in composition) is the reason why there is considerable difference in the reported molecular weight and structural properties of asphaltenes. For example, Speight and Plancher^[7] reported an average asphaltene molecular weight of about 2,000 using vapor pressure osmometry, whereby asphaltenes were dissolved in highly polar solvents. On the other hand, Wiehe^[8] reported an average asphaltene molecular weight of between 500 and 4,000 using the same technique but with o-dichlorobenzene as the solvent.

Using fluorescence depolarization (which can detect the size of fused aromatic clusters), Groenzin and Mullins^[9] concluded that each asphaltene monomer (which can be thought of as a tambourine with dangling arms because of its large polynuclear aromatic cores) has an average molecular weight of between 500 to 1,000 and contains 1 or 2 fused polynuclear aromatic clusters per molecule. These monomer molecules form asphaltene "stacks" in toluene solution even with asphaltene concentrations as low as 0.06 g/L.^[9] There is considerable variation in the reported number of asphaltene "monomer molecules" in a stack, and computer simulations show a stack size of about 5 monomer molecules if each monomer molecule is about 10 Angstrom in diameter.^[10]

One of the simple techniques that have been used to estimate asphaltene solubility is to plot the surface tension of a mixture containing asphaltenes against asphaltene concentration. A break in the surface tension vs. asphaltene concentration curve can be measured for solutions containing dissolved asphaltenes.^[11] Some researchers call this point of singularity the critical micelle concentration (cmc) of asphaltenes, with the view that asphaltenes form micelles in solution (to be discussed in more detail in Section 2.4). The occurrence of a point singularity in the surface tension vs. asphaltene concentration curve may simply signal the onset of a phase transition. In either case, the cmc is a measurable quantity that has been used to estimate the stability of asphaltenes in different mixtures (such as crude oil blends) and to investigate the effectiveness of asphaltene inhibitors.

Several other properties of interest include the mass density, the solubility parameter, and the refractive index of asphaltenes. The mass density of asphaltenes is estimated by several authors to be between 1.13 g/cm^3 and 1.20 g/cm^3 using Archimedean techniques, with most authors reporting values closer to 1.20 g/cm^3 than 1.13 g/cm^3 .^[5] Estimated solubility parameters (at 25°C) of between 19 and $24 \text{ MPa}^{0.5}$ have been reported for asphaltenes based on solvent-solute mutual solubility.^[3,12,13] And refractive indices (at 25°C) of between 1.70 and 1.8 have been extrapolated for asphaltenes from diluted asphaltene solutions in toluene.^[5]

2.2 Economic Significance

Asphaltene is suitably termed the “cholesterol of petroleum”^[14] because of its ability to precipitate with changes in crude oil temperature, pressure, and composition. These precipitates may in turn adhere to surfaces or change crude oil rheology. The economic implications of asphaltene precipitation from crude oils are significant in petroleum production and refining because of this precipitation/adhesion potential. Deposition and subsequent fouling, occlusion, or damage have been observed in all aspects of petroleum recovery and processing, from near wellbore formations to well bores and well tubings to pipelines to refinery units. Furthermore, the asphaltene problem shows no geographic boundaries. Asphaltene related problems have been encountered in all parts of the world, from the North Sea to North Africa to the Americas.^[15-18] And depositions may occur even in fields that have very little asphaltenes. For instance, depositions were reported in well tubings and production processing facilities of the Ula reservoir in the North sea despite the crude oil having only 0.57% mass asphaltene.^[17] Finally, asphaltene problems may disappear in later stages of primary depletion (as in the case of Ventura Avenue field in California^[16]) because normal production tends to produce the lighter fractions first (due to higher mobility) and the residual asphaltene fractions are gradually stabilized (the reasons for this will be discussed in the next section).

In spite of nearly 70 years of asphaltene research, our understanding of the material is still at its infancy. This is due partly to the complex nature of

asphaltene and partly to the difficulties involved in conducting asphaltene research in its natural reservoir environment. As the industry moves towards deeper reservoirs and relies more on integrated production systems (both sub-sea and on-shore), the probability of encountering asphaltene precipitation problems will only increase and the economic implications will become more significant.

2.3 The Phase Behavior of Asphaltenes in Crude Oil

The behavior of asphaltenes in oil can be deduced by examining a few representative examples of field experiences with asphaltene problems.^[15,16,19-22] From these experiences, it can be concluded that pressure contribution to asphaltene phase separation is most pronounced for light oil near its bubble point. Asphaltenes are usually stable in highly under-saturated oils. And at pressures well below the bubble point, asphaltenes tend to be stable since most of the precipitants (methane, ethane, nitrogen, etc.) have escaped from the liquid. Furthermore, light oils with little asphaltenes are the most susceptible to asphaltene problems. Compositional changes such as oil blending or miscible flooding sometimes result in asphaltene precipitation. And temperature changes may result in either asphaltene precipitation or solubilization. For instance, in the propane deasphalting process, asphaltenes become increasingly unstable with temperature increase.^[23] However, for n-alkane (n-C₅₊) titrations, asphaltene stability improves with increasing temperature.^[23]

These observations concerning asphaltene precipitation can be explained in terms of changes to crude oil cohesive energy density (CED) with changes in temperature, pressure, and/or composition. CED is defined by Hildebrand and Scatchard for regular (i.e. nonpolar) fluids as the square of the solubility parameter δ and can be approximated as^[24]

$$CED_i \equiv \delta_i^2 = \frac{-U_i^{rsm}}{v_i} \quad (2.1)$$

where U_i^{rsm} is the residual internal energy (the internal energy obtained by subtracting the ideal gas contribution from that of the real fluid) and v_i is the liquid volume of pure species i . For binary mixtures, the residual internal energy can be approximated as^[24]

$$U_{mix}^{rsm} = -\frac{CED_i v_i^2 x_i^2 + CED_j v_j^2 x_j^2 + 2\sqrt{CED_i CED_j} v_i v_j x_i x_j}{x_i v_i + x_j v_j} \quad (2.2)$$

where x_i is the mole fraction of the i th species. Equations 2.1 and 2.2 show the dependence of mixture CED on density and on the CED (or solubility parameter) of the component species.

Alternatively, from statistical mechanics, we can approximate^[25]

$$U_{mix}^{rsm} = \frac{2\pi}{v} \sum_{\alpha=a}^{a+b} \sum_{\beta=b}^{a+b} N_{\alpha} N_{\beta} \int_0^{\infty} \phi_{\alpha\beta}(r) g_{\alpha\beta}(r) r^2 dr \quad (2.3)$$

where a and b denote species type, N_{α} and N_{β} are the number of α and β molecules, $g_{\alpha\beta}$ is the pair correlation function, r is distance, and $\phi_{\alpha\beta}$ is the molecular interaction potential. Eqn. 2.3 provides more insight to the behavior of

fluids at the molecular level (than Eqn. 2.2) because it relates molecular interaction potentials to bulk properties.

For mixtures dominated by van der Waals' interactions (also called dispersion or non-polar interactions), ϕ_{ab} in Eqn. 2.3 has an attraction contribution proportional to the product of the interacting species' electronic polarizabilities and inversely proportional to the sixth power of molecular distance.^[26] Hence for non-polar mixtures, the mixture's *CED* is a function of density and the electronic polarizabilities of the mixture's constituent species. As a measure of the displacement of a molecule's electron clouds under the influence of external electric fields, electronic polarizability is dependent on the structure of the molecule and on the frequency of the external electric field but is, to the first order, independent of thermodynamic state. The polarizability of molecules dominated by nonpolar interactions are insensitive to the frequencies of the external electric field below those of visible light.^[26]

The behavior of asphaltenes in crude oil can be described in terms of changes to the oil's cohesive energy density. Above the bubble point, further pressure increases lead to increasing oil density, which increases the oil's *CED* and makes asphaltenes more stable. Below the bubble point, there is a net increase in density with pressure decrease due to the release of lighter hydrocarbons from the oil. Again the oil becomes a better solvent for asphaltenes. An increase in temperature decreases the oil density but at the

same time increases the entropy of the solution, resulting in a counter balancing effect. Composition changes that increase density may improve asphaltene solubility, and composition changes that decrease density may have the opposite effect. The inclusion to the oil of species with lower polarizabilities (e.g. addition of methane or blending with lighter oils) will decrease the oil's *CED* and increase the likelihood of asphaltene flocculation. And the inclusion of species that are similar in polarizability (e.g. addition of toluene) will keep asphaltenes from becoming unstable. Because both density and component polarizability affect a mixture's *CED*, opposing effects may be observed. For example, CO₂ may be more dense than oil at high pressures but may act as a precipitant because of its low polarizability. Evidence of the important role of cohesive energy density (or solubility parameter) on asphaltene behavior points to the significance of nonpolar interactions in determining asphaltene phase behavior in crude oil.

2.4 Our Hypothesis

The underlying hypothesis of our approach is that molecular size and nonpolar van der Waals interactions dominate asphaltene phase behavior in reservoir fluids. We have described in the previous section how asphaltene phase behavior can be qualitatively explained in terms of nonpolar interactions. Our hypothesis is also supported by other evidence:

- (1) The intermolecular interaction energies due to the polynuclear aromatic cores (which are plate-like structures with large surface areas) may be

similar or larger in magnitude than the energies due to polar interactions. For instance, Khryaschchev, *et al.*^[27] calculated the energy between the polynuclear aromatic cores of asphaltenes to be about 80 kJ/mol, which is much larger than the hydrogen bonding interaction energy in water (~15 kJ/mol).

(2) An investigation of asphaltene solubility in over 40 polar and nonpolar solvents by Wiehe^[8] shows that asphaltenes are soluble in solvents with high field force solubility parameters (which is a measure of nonpolar, mean field interaction strength) and insoluble in solvents with moderate and high complexing solubility parameters (which is a measure of hydrogen bonding and polar interaction strengths).

(3) One traditional viewpoint on asphaltene behavior relies on a micellar model in which asphaltenes are stabilized by resins via polar-polar interactions. The basis of this viewpoint is that asphaltenes and resins are the most polar fractions of crude oil because they contain heteroatoms of various proportions. When resins are added, less asphaltenes will precipitate. And when n-alkanes are added, asphaltenes will precipitate because of the dilution of resins in the mixture. The argument is similar to the explanation given for the addition of surfactants (resins) to an oil/water mixture to stabilize the dispersion; stable micro-emulsions would form with sufficient surfactant addition. However, nonpolar diluents of similar size and structure can be either precipitants or solvents for asphaltenes. For instance, toluene ($C_6H_5CH_3$) is a good nonpolar

solvent for asphaltenes while n-heptane (C_7H_{16}) is a nonpolar precipitant. Similarly, both carbon disulfide (CS_2) and carbon dioxide (CO_2) are nonpolar and of similar molecular structure but CS_2 is a good solvent for asphaltenes while CO_2 is a precipitant.

In a few situations, the role of polar or hydrogen bonding interactions may become important. For example, asphaltenes may aggregate on the water-oil interface and stabilize water emulsions.^[28] And addition of a sufficiently large amount of alkyl-benzene derived amphiphiles (such as dodecyl benzene sulfonic acid) would inhibit asphaltene aggregation.^[29] While polar interactions may play a role, our hypothesis is that asphaltene phase behavior in the reservoir is shaped to a larger extent by the nonpolar interactions in the oil.

2.5 Asphaltene Thermodynamic Models

Thermodynamic models of asphaltene phase behavior in crude oil generally fall under one of two molecular thermodynamic frameworks, mirroring the two prevalent schools of thought regarding how asphaltenes are stabilized in crude oil. The first approach assumes that asphaltenes are solvated in crude oil and that these asphaltenes will precipitate if the oil solubility drops below a certain threshold. The Flory-Huggins-regular-solution based models and the cubic equation of state based models are some examples of this approach.^[5,13,30-32] Thermodynamic models in the second category take the colloidal approach to describe asphaltene behavior and the presence of resins

becomes critical in stabilizing asphaltenes. The solid-asphaltene colloidal model proposed by Leontaritis and Mansoori^[33], the reversible micellization model proposed by Victorov and Firoozabadi^[34], and the McMillan-Mayer-SAFT based theory proposed by Wu^[23] are some examples in this category.

2.5.1 Classical Thermodynamic Models

One of the most widely used classical thermodynamic models to describe asphaltene behavior is the Flory-Huggins-regular-solution theory:^[24]

$$\frac{\Delta G_{mix}}{RT} = N_1 \ln \Phi_1^* + N_2 \ln \Phi_2^* + \frac{v_1}{RT} (\delta_1 - \delta_2)^2 \Phi_1^* \Phi_2^* (N_1 + rN_2) \quad (2.4)$$

where

$$\Phi_1^* = \frac{N_1}{N_1 + rN_2}; \quad \Phi_2^* = \frac{rN_2}{N_1 + rN_2} \quad (2.5)$$

In Eqn. 2.4, ΔG_{mix} is the change in Gibbs energy on mixing, R is the gas constant, T is temperature, v_1 is the molar volume of the solvent, N_1 , N_2 are the number of solvent and solute molecules, respectively, r is the ratio of solute to solvent volume, and δ_1 , δ_2 are the solubility parameter of the solvent and solute at T . Φ^* in Eqn. 2.5 is the volume fraction of either the solvent or the solute species.

The application of this model to describe asphaltene phase behavior was first proposed by Hirschberg, *et al.*^[13] In the Hirschberg implementation, the asphaltene-rich phase is assumed to be pure asphaltenes (i.e. $\Phi_2^* = 1$ where the subscript 2 denotes asphaltenes). Furthermore, the amount of asphaltenes in the asphaltene-lean phase is assumed to be very small (i.e. $\Phi_2^* \ll 1$). With

these assumptions and applying the condition of chemical potential equality at equilibrium (see Chapter 4), the composition of asphaltenes in the asphaltene-lean phase becomes

$$\Phi_{2,\text{asphaltene-lean}}^* = \exp\left[-1 + r - \frac{rv_1}{RT}(\delta_2 - \delta_1)^2\right] \quad (2.6)$$

If the solvent (crude oil) and asphaltene solubility parameters and the solvent molar volume can be measured, the volume fraction of asphaltenes in the asphaltene-lean phase becomes a function of asphaltene molar volume only.

Other models based on the Flory-Huggins-regular-solution theory change/relax the assumptions made by Hirschberg, *et al.*^[13] For instance, in the implementation of Cimino, *et al.*^[31], a pure solvent phase is assumed to form upon phase separation. And in the implementation of Wang^[5], each of the coexisting phases can have asphaltenes as well as solvents.

While the Flory-Huggins-regular solution based approaches have been used with varying success to model asphaltene solubility with n-alkane titrations under ambient conditions, it is difficult to extend the approach to model asphaltene solubility under reservoir conditions. In a sense, the theory is not a “complete” equation of state; unless the volumes and solubility parameters are measured under reservoir conditions, these values must be obtained from another equation of state or estimated from empirical correlations. Furthermore, the model cannot reproduce/predict certain classes of phase diagrams unless extremely temperature dependent energy modification parameters are

introduced. For instance, the model is incapable of showing lower critical solution behavior in systems of large size differences unless extremely temperature dependent binary interaction parameters are used.

Another popular approach in the classical thermodynamics framework to model asphaltene behavior is to use the cubic equations of state. A description of one of the cubic equations (the Peng-Robinson equations) is given in Chapter 5. In the method proposed by Nghiem, *et al.*^[35], the C₃₁₊ heavy end of crude oil is first divided into nonprecipitating and precipitating sub-fractions. Different interaction parameters (between these sub-fractions and light ends) are then assigned to reproduce experimental results. In another example, Akbarzadeh, *et al.*^[30] modified the Soave-Redlich-Kwong cubic equations by adding an additional aggregation size parameter to asphaltenes.

The cubic equations have relatively simple functional forms and are easy to implement into existing reservoir simulators because cubic equations have been used extensively to describe the thermodynamic behavior of reservoir fluids. However, their major shortcomings are that the equations of state cannot describe the phase behavior of systems with large size disparities and that they cannot accurately describe fluid densities. While the calculated densities can be modified using volume translation techniques, volume translations do not affect phase equilibria calculations. These issues will be addressed in more detail in Chapter 5.

As mentioned above, the Flory-Huggins-regular-solution model is not a “complete” equation of state because it requires as input physically-based parameters that must be obtained using other methods. Hence the Flory-Huggins-regular-solution model has been often used in conjunction with other equations of state to model asphaltene solubility. For example, in the work of Chung, *et al.*^[36], the Flory-Huggins-regular-solution model is combined with the Peng-Robinson cubic equations to model asphaltene solubility in oil. And in the work of Burke, *et al.*^[37], the Flory-Huggins-regular-solution model parameters were obtained from the Zudkevitch-Joffe-Redlich-Kwong equations.

2.5.2 Colloidal Models

The colloidal models assume that crude oil can be divided into polar and nonpolar sub-fractions; the saturate and aromatic components make up the nonpolar sub-fraction while asphaltenes and resins comprise the polar sub-fraction. The model due to Leontaritis and Mansoori^[33] is one of the earliest models using this approach. In this model, asphaltenes are assumed to be insoluble solid particles suspended in oil and kept in solution by resins (which adsorb onto the surfaces of asphaltene molecules). For asphaltenes to stay in solution, resins must be present. Dilution of the resins below a certain threshold will cause asphaltenes to precipitate.

In the approach due to Pan and Firoozabadi and Victorov and Firoozabadi^[38] (the reversible-micellization approach), the assumption that asphaltenes are insoluble solid particles is relaxed. In this approach, the total Gibbs energy of a system consisting of a liquid phase and a precipitated phase is minimized to calculate equilibrium phase compositions. The liquid phase consists of a mixture of monomer asphaltenes, monomer resins, asphaltene-resin micelles, and other oil species. And the precipitated phase is assumed to consist solely of asphaltenes and resins that do not associate with each other. An equation of state (such as the Peng-Robinson cubic equations) is used to calculate the fugacity coefficients of each species (including those of asphaltenes and resins).

To calculate the Gibbs energy of the liquid phase, an expression for the energy change due to asphaltene-resin micelle formation is needed:

$$\Delta G_m^{00} = [(\Delta G_a^0)_{tr} + (\Delta G_a^0)_{def}] + (\Delta G_m^0)_{int} + [(\Delta G_r^0)_{tr} + (\Delta G_r^0)_{ads} + (\Delta G_r^0)_{def}] \quad (2.6)$$

$(\Delta G_a^0)_{tr}$ is the Gibbs energy change due to the transfer of asphaltene (subscript a) molecules from an infinitely dilute solution to an aggregated, pure asphaltene state. $(\Delta G_a^0)_{def}$ is the Gibbs energy of deformation of asphaltene molecules and $(\Delta G_a^0)_{int}$ is the interfacial Gibbs energy of the formation of micellar cores. Since resins also take part in the formation of micelles, their energy contributions are accounted for in the terms with the subscript r . Additionally, an energy

contribution due to the adsorption of resins onto asphaltene micellar cores is needed $(\Delta G_r^0)_{ads}$.

While the reversible-micellization model has shown some success in describing the effects of pressure and concentration on asphaltene precipitation^[38], a large number of parameters are needed in the model. Each species in the model (including asphaltenes and resins) requires a set of equation of state parameters. If the cubic equations are used (i.e. the Peng-Robinson equations), 3 pure species parameters plus a set of interaction parameters are needed for each pure component. To calculate the energy of micellization, parameters such as the size of the micellar core, the average characteristic length of the oil (non-asphaltene) molecules, the interfacial tension between the asphaltene in the micellar core and the bulk oil, the thickness of each asphaltenes-resins micelle, and the adsorption energy of the resins onto the asphaltene micellar core, among others, are needed. It is not clear how some of these parameters vary with changes in pressure, temperature, and oil composition.

In a third approach due to Wu and Prausnitz^[23], asphaltenes are assumed to be large spherical molecules with multiple association sites that can bind to other asphaltenes and to resins (which are smaller molecules with only one association site per molecule). The theory is presented in the McMillan-Mayer framework using the Statistical Associating Fluid Theory (SAFT) to describe the

free energy of association between asphaltenes and resins. Hence, only asphaltenes and resins exist as real molecular species; other components in the oil exist solely as “background” contributions to the free energy of the mixture.

An advantage of the McMillan-Mayer-SAFT approach is that the complexity of the problem can be significantly reduced by formulating the theory in the McMillan-Mayer framework. Furthermore, the theory can account for the effects of resins addition and asphaltene solvent addition on the solubility of asphaltenes. The addition of resins would “tie” up bonding sites on asphaltenes that otherwise would bind to other asphaltenes, and the addition of asphaltene solvents would improve asphaltene solubility by changing the magnitude of the “background” energy. One potential issue with this approach is that it is not clear how the McMillan-Mayer approximations affect the energies calculated by SAFT. As a statistical mechanical equation of state based on the perturbation of molecular segment densities (see Chapter 4 and 10), even molecular species that do not associate contribute to the association energy calculations indirectly in SAFT by their contribution to the correlation functions. In the approach proposed by Wu and Prausnitz^[23], only asphaltenes and resins are “real” molecules and the presence of the nonassociating species (that exist in the oil and affect the extent of association) are ignored.

CHAPTER 3. EXPERIMENTS OF ASPHALTENE STABILITY

3.1 Introduction

The objective of this experimental study is to provide a set of data to test models of asphaltene precipitation from crude oil. We performed experiments simulating reservoir depressurization on a model live oil (mixture of toluene, methane, and n-heptane insoluble asphaltenes) and on a recombined oil (stock-tank oil with its separator gas). The asphaltene stability boundaries and mixture bubble point curves of these oils were measured as functions of pressure, temperature, and dissolved gas concentration. The effects of pressure on mixture density were also monitored from constant composition volume expansion measurements.

A set of titration experiments with n-heptane, n-undecane, and n-pentadecane titrants were also performed on the model oil and stock-tank oil described above. These ambient condition titration experiments were performed by J.X. Wang at New Mexico Institute of Mining and Technology (NMT) using different oil samples (but all are from the same reservoir, see Table 3.1). The titration procedure is described in Ting, *et al.*^[39] and the titration results are given in Table 3.2 and Figure 3.1 in terms of the n-alkane precipitant volume fraction (ϕ_{ppt}^V) and the refractive indices at the onsets of asphaltene instability (P_{RI}). Note that equi-volume of α -methyl-naphthalene was added to the stock-tank oil before

the ambient condition titration experiments to dissolve any preexisting solids in the oil. For a given oil/precipitant pair, the addition of asphaltene solvents (such as α -methyl-naphthalene) to the oil changes the amount of precipitant needed to induce asphaltene precipitation but has little effect on the mixture's refractive index at precipitation onset. [40]

Table 3.1 Properties of the oil samples (all from the same reservoir) used in the study.

	stock-tank oil used in this study to make the recombined oil	stock-tank oil used in titration study at ambient conditions ^a	source of extracted asphaltenes used to make the model oil ^a
density at 20°C (g/cm ³)	0.857	0.8673	0.8679
saturates (mass %)	72.3	70.6	70.6
aromatics (mass %)	16	16.3	15
resins (mass %)	9.2	11.4	12.9
asphaltenes (mass %)	2.5	1.7	1.5

a Measured by Jianxin Wang at New Mexico Institute of Technology.

Table 3.2 Precipitant volume fractions ($\phi_{\text{ppt}}^{\text{V}}$) and mixture refractive indices (P_{RI}) at the onset of asphaltene instability for the stock-tank oil mixture and the model oil.^a

precipitant	model Oil		equi-volume stock-tank oil & α -methyl -naphthalene	
	$\phi_{\text{ppt}}^{\text{V}}$	P_{RI}	$\phi_{\text{ppt}}^{\text{V}}$	P_{RI}
n-C ₇	0.45	1.4477	0.66	1.4444
n-C ₁₁	0.42	1.4618	0.65	1.4632
n-C ₁₅	0.36	1.4721	0.59	1.4795

a Measured by Jianxin Wang at New Mexico Institute of Technology.

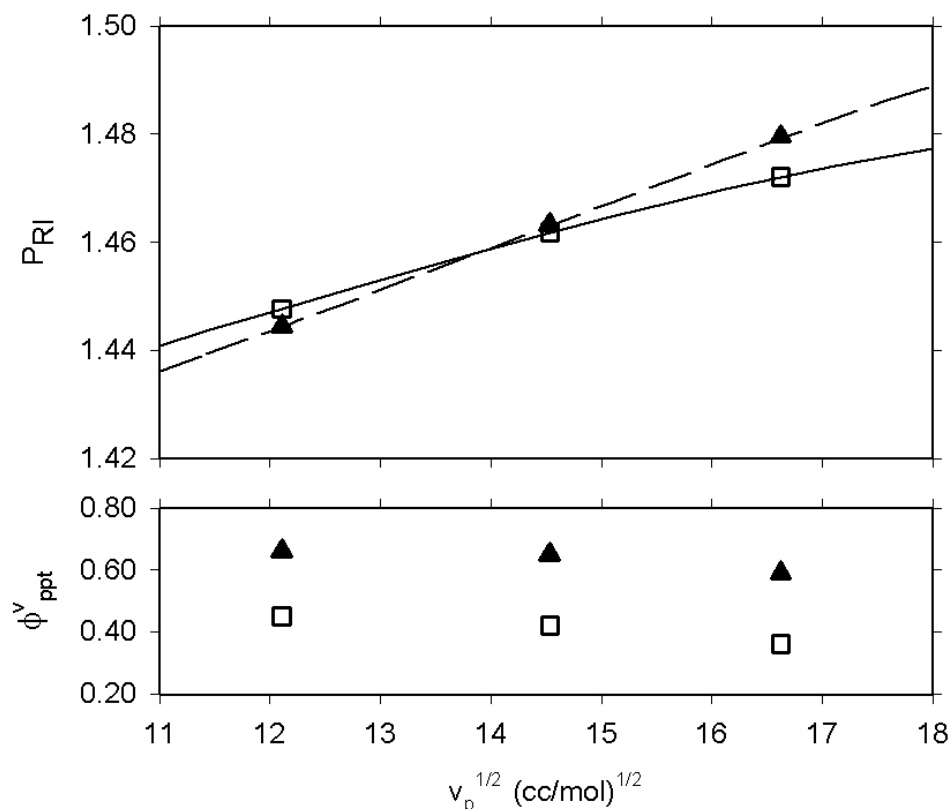


Figure 3.1 P_{RI} and ϕ_{ppt}^V at asphaltene instability onsets for the model oil (square) and the stock-tank oil mixture (triangle) as a function of the square root of the precipitant molar volume ($v_p^{1/2}$) at 20°C.

The reservoir condition depressurization experiments (performed in this work) and the ambient condition titration experiments (performed by NMT) provide a set of data on asphaltene stability in a wide range of nonpolar precipitants from methane and separator gas (which is primarily methane, ethane, and propane) to n-pentadecane. Our hypothesis is that the mechanism responsible for asphaltene precipitation under reservoir depressurization is consistent with the mechanism in titration experiments. If this is true, we expect that thermodynamic models that account for van der Waals interactions, molecular size, and pressure effects should be able to predict the

depressurization results based on matching the results of the titration experiments.

3.2 Experimental

3.2.1 Stock-Tank Oil Properties

The stock-tank oil used in this study has a density of 0.857 g/cm³ at 293K and 0.848 g/cm³ at 328K (both at 14.5 psi). This corresponds to an API gravity of 33.6° at 293K. Using the ASTM D2007-80 method^[4], the stock-tank oil was fractionated into 72.3% (mass) saturates, 16.0% (mass) aromatics, 9.2% (mass) resins, and 2.5% (mass) n-heptane insoluble asphaltenes (Table 3.1). A breakdown of the oil composition is shown in Table 3.3. The composition was determined using gas-chromatography. A generalized single carbon number correlation due to Katz and Firoozabadi^[41] was used to estimate the molecular weight of C₁₀₊ petroleum sub-fractions. The correlation is based on normal boiling point distillation data of more than 26 condensates and liquid hydrocarbons.

Table 3.3 Stock-tank oil and separator gas compositions.

component	molecular weight	reservoir gas	stock-tank oil
		mass fraction	mass fraction
CO ₂	44.01	0.019	
N ₂	28.01	0.136	
C ₁	16.04	0.285	
C ₂	30.07	0.139	
C ₃	44.10	0.141	
C ₄	58.12	0.147	
C ₅	72.15	0.080	0.001
C ₆	86.20	0.027	0.004
m-cyclopentane	84.16		0.001
benzene	78.11		0.000
cyclohexane	84.16		0.001
C ₇	100.20	0.016	0.009
m-cyclohexane	98.19		0.004
toluene	92.14		0.001
C ₈	114.23	0.008	0.020
ethyl-benzene	106.17		0.001
xylene	106.17		0.005
C ₉	128.30	0.002	0.027
C ₁₀	134.00		0.041
C ₁₁	147.00		0.041
C ₁₂	161.00		0.040
C ₁₃	175.00		0.045
C ₁₄	190.00		0.042
C ₁₅	206.00		0.044
C ₁₆	222.00		0.038
C ₁₇	237.00		0.035
C ₁₈	251.00		0.035
C ₁₉	263.00		0.034
C ₂₀	275.00		0.031
C ₂₁	291.00		0.028
C ₂₂	305.00		0.025
C ₂₃	318.00		0.024
C ₂₄	331.00		0.021
C ₂₅	345.00		0.022
C ₂₆	359.00		0.017
C ₂₇	374.00		0.020
C ₂₈	388.00		0.017
C ₂₉	402.00		0.017
C ₃₀₊	580.00		0.307

3.2.2 Model Oil Preparation

Asphaltenes were extracted from a slightly different stock-tank oil from the same reservoir (Table 3.1) using a modified ASTM-D2007-80 procedure. [4] The extraction was performed by J.X. Wang at New Mexico Institute of Mining and Technology. A 40:1 excess volume of n-heptane was mixed with the oil for two days and the solution filtered through a range of filters from 8 down to 0.22 μm . The collected solids were redissolved in excess toluene (to a concentration of about 0.5%) and the solution filtered (with 0.22 μm filter) to remove any nonasphaltic solids. The filtrate was then concentrated using a rotary evaporator and the asphaltenes reprecipitated with 40:1 excess volume of n-heptane. After filtration with 0.22 μm filter, the solids were dried at ambient conditions for two days.

To prepare the model oil, the extracted asphaltenes were dissolved in degassed toluene (Fisher Scientific, Certified ACS Grade) at a ratio of 1 g asphaltenes per 100 mL toluene at 20°C and atmospheric pressure. The mixture was stirred constantly and aged for two days before being filtered through a 0.20 μm (Osmonics Inc. Silver Membrane) filter. The mass of undissolved solids removed equaled 7% to 8% of the mass of asphaltenes initially present in the model oil mixture.

3.2.3 Recombined Oil Preparation

Separator gas (0.378 g/cm^3 at 293K and 3,500 psi) with the composition given in Table 3.3 was prepared and mixed with the stock-tank oil to create a recombined oil with a targeted gas-oil-ratio (GOR) between 140 and 150 m^3/m^3 . The recombined oil was first aged for four days at 71.1°C and 6,000 psi outside the PVT cell and then kept at 71.1°C and 8,588 psi inside the PVT cell for 24 hours before use. The GOR of the prepared recombined oil was determined to be 152 m^3/m^3 using a DB Robinson Gasometer. Since the total mass of the one phase fluid in the PVT cell, the stock-tank oil density at ambient conditions, and the gas-oil-ratio were known, the mass of the dissolved gas could be calculated. The ideal gas equation of state was used to estimate gas density at ambient conditions using an average molecular weight of 28.5 obtained from composition data.

Asphaltene problems that occurred in the field from which this oil sample was taken were associated with injection of CO_2 . Because asphaltene related problems were not observed in the field prior to the introduction of CO_2 , it is unlikely that asphaltene precipitation would be observed if the oil were recombined to a GOR representative of down-hole samples. Therefore more separator gas was added in all experiments than the amount observed in down-hole samples.

3.2.4 High Pressure and Temperature Apparatus

A near infrared laser (2.0 milliwatts) transmittance device mounted on a visual PVT cell was used to detect phase instability onsets (Figure 3.2). The apparatus was designed and manufactured by DB Robinson. With this system, asphaltene instability and bubble point onsets could be observed as sudden decreases in light transmittance (due to increased light scattering caused by the formation of a second phase). The PVT cell had a maximum operating pressure of 15,000 psi and was mounted in an air temperature bath. The fluid of interest was placed inside a Pyrex glass cylinder (maximum sample volume of about 113 cc) and stirred using a magnetically coupled mixer. A volume displacement pump (DBR Series II Pump) controlled system pressure by adjusting the amount of overburden fluid based on readings from a digital Heise pressure gauge (accurate to $\pm 0.15\%$ of 15,000 psi). The pressure gauge was located on the overburden side of the apparatus. The cell temperature was measured using a platinum RTD (accurate to $\pm 0.05^\circ\text{C}$). During each experiment, the fluid volume was monitored using an external CCD camera (accurate to ± 0.002 cc). Additional fluid or gas could be added into the cell using a mercury displacement pump (accurate to ± 0.005 cc) via a port next to the magnetic stirrer.

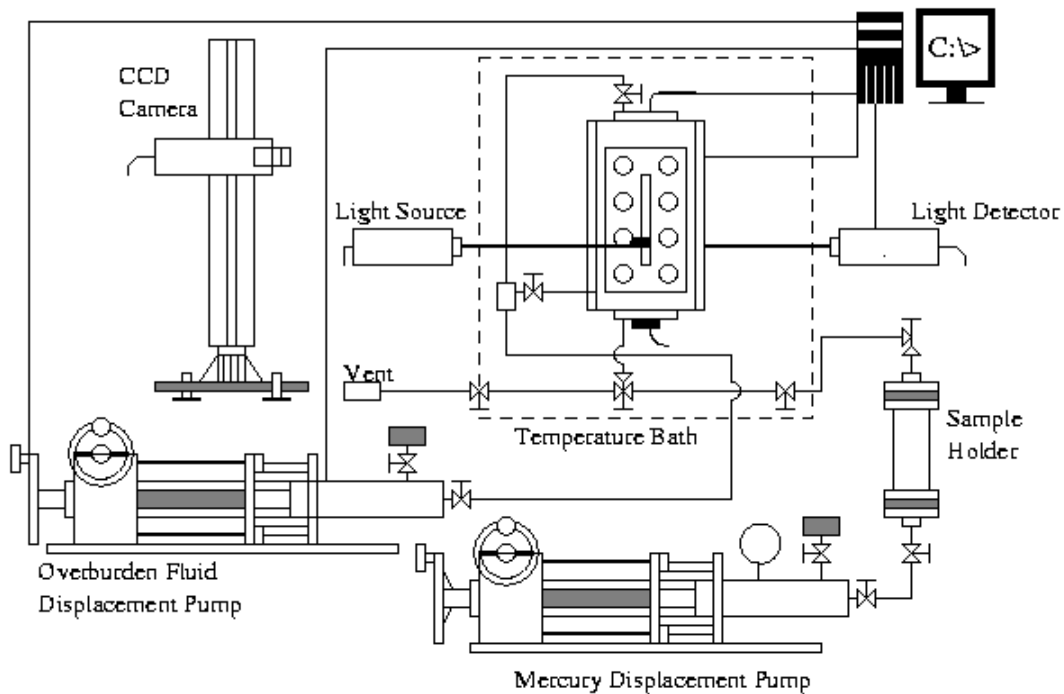


Figure 3.2 Diagram of the DB Robinson PVT apparatus used in the study.

3.2.5 Procedure

For the model oil investigations, a measured amount of the asphaltene-toluene mixture was fed into the PVT cell and pressurized to 5,500 psig. After temperature equilibration, a known amount of Air Product Ultra High Purity methane (at 6,000 psig, 20°C) was injected and the mixture pressurized to between 8,000 and 14,000 psig (depending on the amount of methane in the system) for up to 24 hours to redissolve any of the asphaltenes that might have precipitated during methane injection. While such pressurization led initially to dramatic increases in light transmittance, transmittance reached a plateau after about 12 hours and the change in transmittance became negligible after that point.

To trace out the asphaltene instability and bubble point boundaries, the model live oil was slowly depressurized at 45 minutes per pressure step until asphaltene instability onset. We defined the onset asphaltene instability pressure as the average between the first pressure (i.e. the highest pressure in a depressurization experiment) at which transmittance decreased continuously with time and the pressure step before that (see Figure 3.3). As a polydisperse mixture, some asphaltenes could have already phase separated at even higher pressures but were not observed due to instrument limitations.

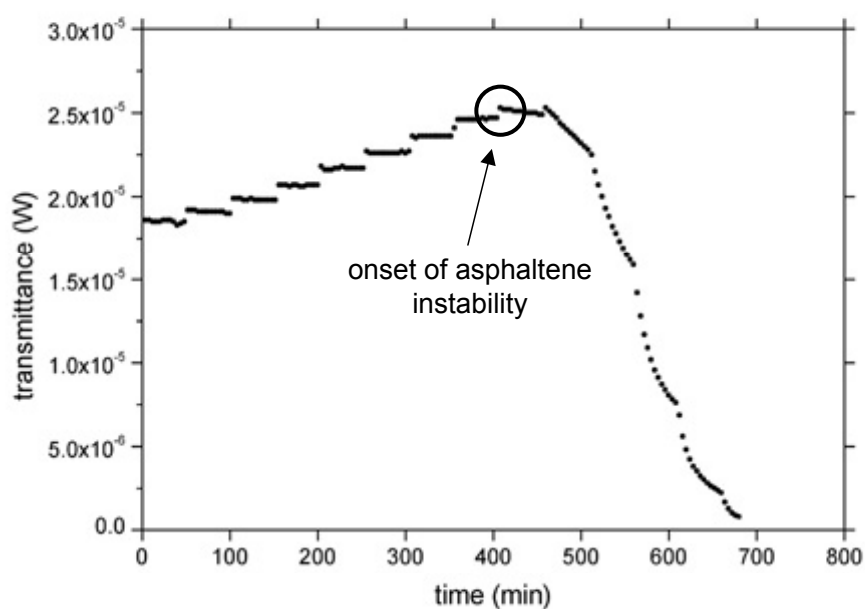


Figure 3.3 The onset of asphaltene instability for the model oil at 65.5°C.

Below the asphaltene instability onset pressure, the system was depressurized quickly until the mixture bubble point was reached (as determined by light transmittance and corroborated with sudden change in overall system

volume). The mixture was then quickly pressurized far above its asphaltene instability point and kept for between 8 to 12 hours to dissolve the asphaltenes that phase separated out of solution. At this point, either the experiment was repeated or a known amount of methane (at 6,000 psig, 20°C) was injected and then the procedure outlined above repeated. The procedure is shown as a cartoon in Figure 3.4.

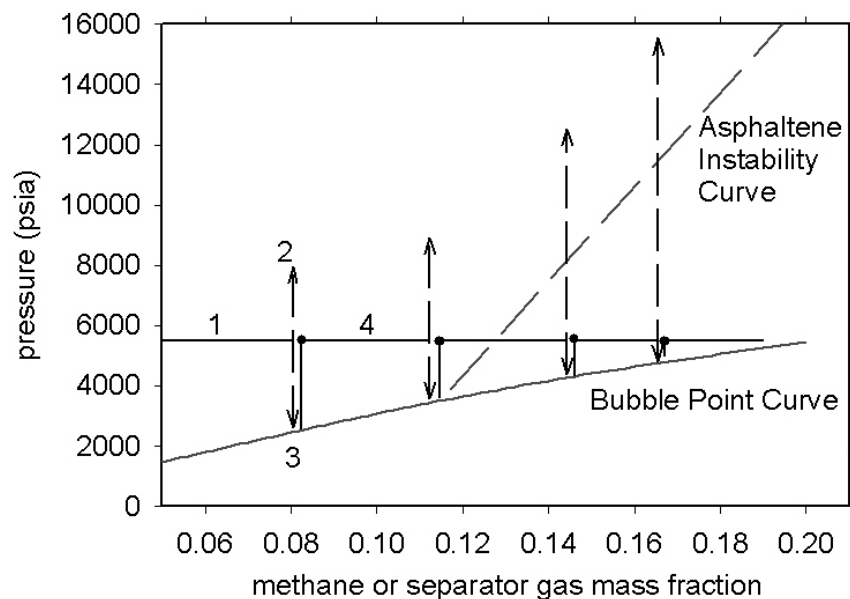


Figure 3.4 Experimental procedure. (1) Methane or separator gas was added, (2) pressure was raised to dissolve asphaltene precipitates, (3) the system was depressurized to find the asphaltene instability and mixture bubble points, the system was repressurized, and (4) gas was added and the experiment repeated.

The recombined oil investigations followed the same procedure as that described above for the model live oil system. In this case, separator gas was added to the recombined oil instead of methane.

3.3 Results

The measured asphaltene instability onset and bubble point pressures of the model live oil at 20.0°C and 65.5°C are listed in Table 3.4 and plotted in Figure 3.5(a). At lower methane concentrations, asphaltene instability was not observed during depressurization. However, as the amount of dissolved methane increased, asphaltene phase separated at increasingly higher pressures. The observed instability onset pressures were nearly linear functions of dissolved gas concentration at each temperature (solid and dashed lines fitted to the asphaltene instability points are shown in Figure 3.5(a)). Significant temperature effects on asphaltene stability were observed, with the fitted instability lines for the two temperatures having very similar slopes.

Table 3.4 Asphaltene instability onset and bubble point pressures of the model live oil.

methane mass frac.	mixture bubble point (psia)	asphaltene instability onset (psia)
T=20.0°C		
0.063 ± 0.001	1915 ± 30	Not Observed
0.103 ± 0.001	3153 ± 30	Not Observed
0.118 ± 0.002	3609 ± 40	4358 ± 130
0.132 ± 0.002	3960 ± 40	5747 ± 250
0.143 ± 0.002	4241 ± 40	7812 ± 100
0.153 ± 0.003		9786 ± 150
T=65.5°C		
0.061 ± 0.001	2038 ± 30	Not Observed
0.100 ± 0.001	3043 ± 30	Not Observed
0.116 ± 0.002	3468 ± 30	Not Observed
0.140 ± 0.002	3911 ± 23	4296 ± 100
0.159 ± 0.003		6514 ± 200
0.169 ± 0.003	4383 ± 23	7883 ± 150
0.180 ± 0.003	4556 ± 40	9899 ± 150

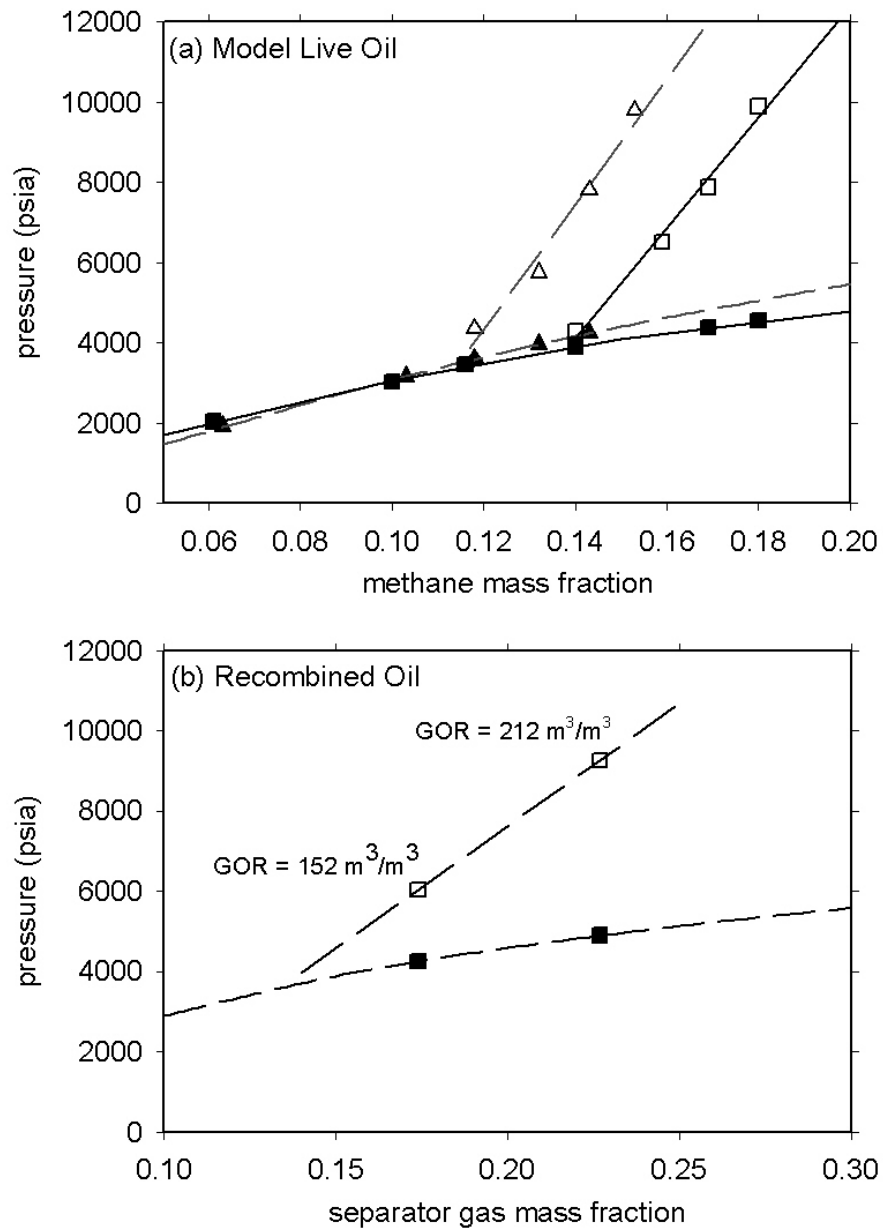


Figure 3.5 (a) Asphaltene instability onsets (open symbols) and bubble points (filled symbols) for the model live oil at 20.0°C (triangles) and 65.5°C (squares). (b) Asphaltene instability onsets (open squares) and bubble points (filled squares) for the recombinated oil at 71.1°C.

The asphaltene instability onset and bubble points for the recombinated oil at 71.1°C are listed in Table 3.5 and plotted in Figure 3.5(b). As seen in Figure 3.5(b), we would expect asphaltene precipitation problems to occur at higher

separator gas concentrations. Comparison of the model and recombined oil results shows that in the limited dissolved gas concentration range investigated, the behavior of asphaltenes to dissolved gas concentration and pressure changes are qualitatively similar. While the bubble point curve for the recombined oil was similar to that of the model oil at 65.5°C in the region investigated, the asphaltenes seemed to be more stable in the recombined oil. If we assumed that the asphaltene instability points for the recombined oil was a linear function of separator gas mass fraction, this line would have a smaller slope than those for the model oils (Figure 3.6). It is interesting to note that if the asphaltene instability points for the recombined oil were plotted as a function of methane plus nitrogen mass fraction (the components in separator gas most dissimilar to asphaltenes in their polarizabilities and densities), the resulting instability “line” has a slope similar to those of the model oil system.

Table 3.5 Asphaltene instability onset and bubble point pressures of the recombined oil.

separator gas mass frac.	bubble point (psia)	asphaltene instability onset (psia)	gas-oil-ratio (m ³ /m ³)
0.174	4250 ± 30	6034 ± 50	152
0.227	4900 ± 23	9266 ± 150	212

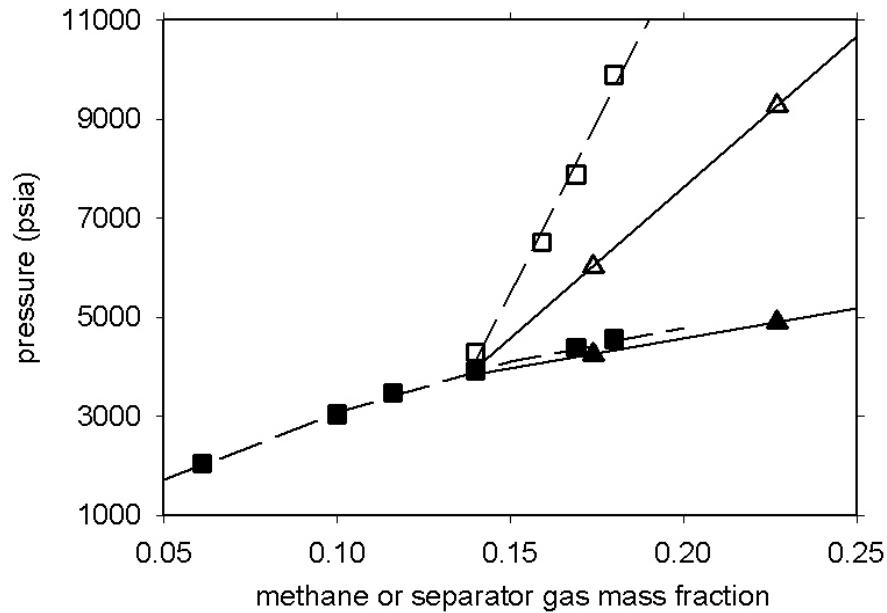


Figure 3.6 Comparison of asphaltene instability onsets (open symbols) and bubble points (filled symbols) for model oil (squares) at 65.5°C and recombinated oil (triangles) at 71.1°C.

The effect of pressure on mass density (from constant composition expansion measurements) for some compositions of model live oil and for the recombinated oil is shown in Figure 3.7. The density information was used in conjunction with composition data to calculate fluid properties discussed in the next section.

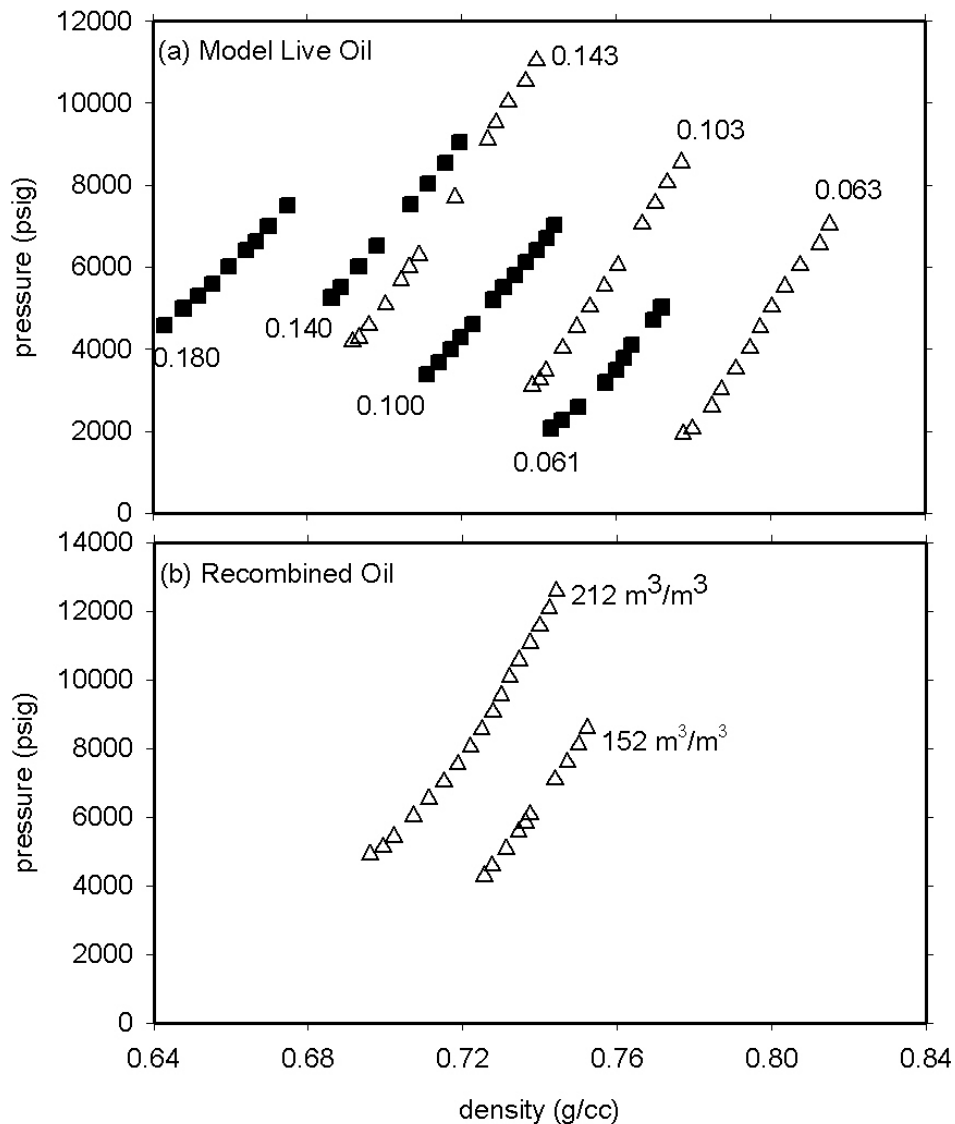


Figure 3.7 Effects of pressure on mass density for (a) model live oil at 20.0°C (triangles, methane mass fraction labeled above data) and 65.5°C (squares, methane mass fraction labeled below data) and (b) recombined oil (GOR labeled above data).

3.4 Discussions

The difference in magnitude between a solvent and a solute's solubility parameter is a measure of miscibility because this difference can be related to the enthalpies of mixing (for instance, see the expressions for Flory-Huggins-

regular-solution equation in Chapter 2.5.1). Demixing would occur if the mixture solubility parameter becomes much smaller than the solubility parameter of the most polarizable species in the mixture (of course, entropy effects would also play a role). A solubility threshold can then be established in terms of the mixture solubility parameter. For van der Waals fluids, a function of the refractive index, $\left(\frac{n^2 - 1}{n^2 + 2}\right)$, is approximately linearly proportional to solubility parameter.^[40] Hence the solubility threshold for nonpolar mixtures can be estimated by measuring the refractive index at the threshold of phase separation.

For the systems studied, we can determine approximately (using the Clausius-Mossotti-Lorenz-Lorentz equation^[42,43]) the refractive indices at the points of asphaltene instability onset from composition and density data:

$$\left(\frac{n_{mix}^2 - 1}{n_{mix}^2 + 2}\right) = \sum_i C_i R_i \quad (3.1)$$

$$R_i = \left(\frac{n_i^2 - 1}{n_i^2 + 2}\right) \left(\frac{MW_i}{d_i}\right) \quad (3.2)$$

In the above equations, n is the refractive index of the mixture or of the i th species and C_i , R_i , MW_i , d_i are the molar concentration, molar refraction, molecular weight, and pure component mass density of the i th species, respectively. In using Eqn. 3.1, we assume that the excess volume on mixing is zero for all components in the mixture. R_i is, to a first approximation, independent of temperature or physical states, and the molar refraction of pure species used in this work were obtained from group contribution methods tabulated in the Handbook of Chemistry and Physics.^[44] A comparison of the

molar refractions of some compounds of interest in this work calculated using the group contribution method and the molar refractions calculated with Eqn. 3.2 (using measured refractive indices) show good agreement (see Table 3.6). We used an asphaltene molar refraction of $1317 \text{ cm}^3/\text{mol}$ (assuming $MW = 3750$, $n = 1.75$ at 20°C , and density = 1.16 g/cm^3 at 20°C) but the contribution of asphaltenes was extremely small due to their low concentrations. In the recombined oil calculations, the stock-tank oil was treated as a single species and its molar refraction ($R = 83.6 \text{ cm}^3/\text{mol}$) was obtained from GC derived average molecular weight ($MW = 250$), measured mixture density ($\rho = 0.857 \text{ g/cm}^3$), and measured refractive index ($n = 1.485$) at ambient conditions. The components in the separator gas were treated explicitly (not as lumped pseudo-components) and the experimental densities in Fig. 3.7 were used to calculate the density contribution from each species.

Table 3.6 Comparison of molar refractions of some compounds of interest calculated using measured refractive indices and densities and using group contribution method.

compound	refractive index ^a (20°C)	molar refraction, Eqn. 3.2 (cm^3/mol)	molar refraction, group contribution ^b (cm^3/mol)	absolute deviation (percent)
n-C ₅	1.3575	25.27	25.29	0.08
n-C ₆	1.3751	29.88	29.94	0.18
n-C ₇	1.3878	34.57	34.59	0.05
n-C ₈	1.3974	39.19	39.23	0.10
n-C ₉	1.4054	43.85	43.88	0.08
n-C ₁₀	1.4102	48.31	48.53	0.45
n-C ₁₁	1.4165	53.05	53.17	0.23
n-C ₁₂	1.4216	57.77	57.82	0.09
n-C ₁₃	1.4251	62.34	62.47	0.21
n-C ₁₄	1.429	67.05	67.11	0.09

n-C ₁₅	1.4314	71.60	71.76	0.23
n-C ₁₆	1.4345	76.33	76.41	0.10
Toluene	1.4964	31.07	31.14	0.22
α -methyl naph.	1.6170	48.77	48.68	0.20
Methane	--	--	6.70	--

a from [45]
b from [44]

Figure 3.8 shows the calculated mixture refractive indices at the measured asphaltene instability onset points. We see that although the mixture compositions and onset pressures are quite different, the refractive indices at the onsets of asphaltene instability are similar at each temperature. Since refractive index is a measure of cohesive energy density, this means that the *CED* of the medium (in other words the solubility environment) is roughly the same along each asphaltene instability onset curve for the investigated mixtures. The near constant values of refractive index along the asphaltene instability boundary are the result of opposing contributions to the mixture *CED* due to composition and pressure changes.

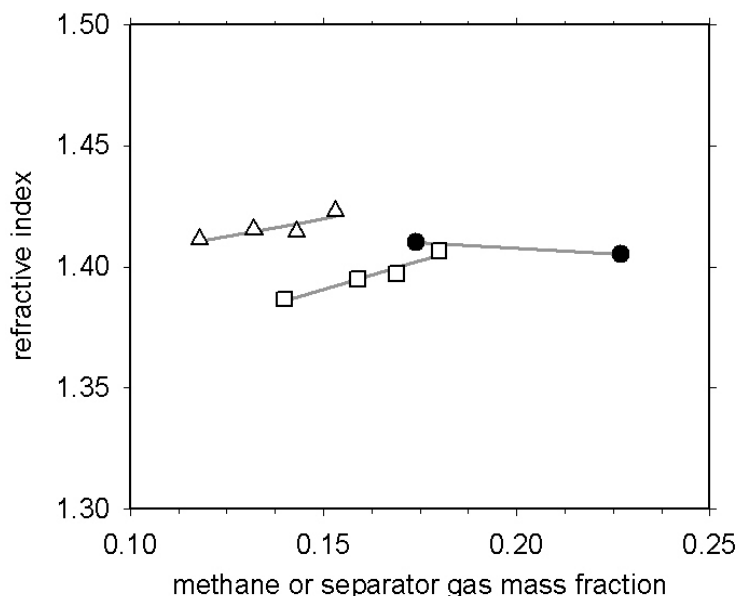


Figure 3.8 Mixture refractive indices on the asphaltene instability boundaries (P_{RI}) for model oil at 20.0°C (triangles), model oil at 65.5°C (squares), and recombined oil at 71.1°C (circles).

Titration studies at ambient conditions show that for many oils and asphaltene solutions, P_{RI} correlates linearly with the square root of the molar volume ($v_p^{1/2}$) of the n-alkane precipitants.^[46] Interpolation between the measured P_{RI} 's can then be used to estimate the onset conditions for other n-alkanes and for n-alkane mixtures. Since the mechanism responsible for asphaltene precipitation under reservoir depressurization is consistent with the mechanism in titration experiments, it should be possible to relate the stability behavior of asphaltenes in the two regimes. By plotting the calculated P_{RI} as a function of the square root of the effective molar volume of methane for the model live oil mixture at 20°C, we see that a near linear correlation can roughly describe the results of the methane induced precipitation and the results of the ambient pressure liquid n-alkane induced precipitation (Figure 3.9). For the

model live oil at 20°C, the value of $v_p^{1/2}$ of methane varies with pressure and mass fraction of methane and can be approximated by an effective methane volume

$$v_{mixture} = x_{toluene} v_{toluene}^{effective} + x_{methane} v_{methane}^{effective} \quad (3.3)$$

where $v_{mixture}$ is the mixture molar volume determined from experiment, $x_{toluene}$ and $x_{methane}$ are the toluene and methane mole fractions, and $v^{effective}$ are the effective molar volumes. The molar volume of pure toluene was used in place of $v_{toluene}^{effective}$. Note that $v_{methane}^{effective}$ is an “effective” methane volume and is not the partial molar volume of methane calculated by an equation of state such as SAFT. Hence by fitting to the asphaltene stability results from titration experiments at ambient conditions, we may be able to estimate the onset of asphaltene precipitation as a function of pressure, provided that we know the effective molar volume of the precipitants as a function of pressure.

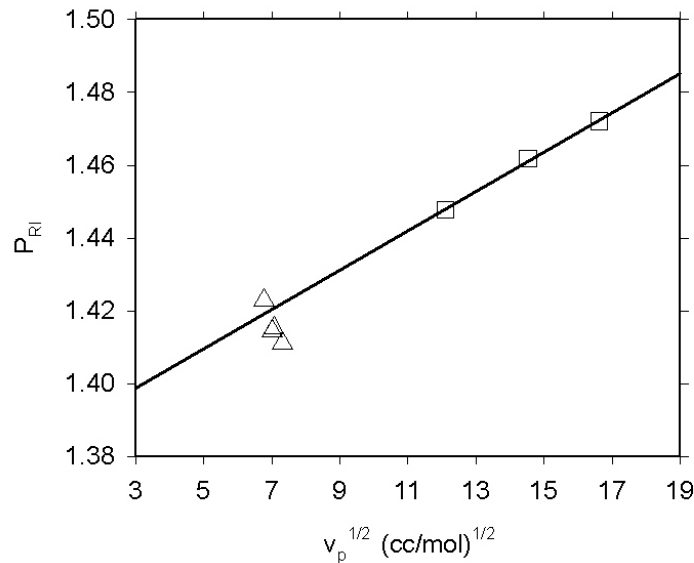


Figure 3.9 Measured P_{RI} vs. $v_p^{1/2}$ of n-alkane titrants (squares) for the model oil and calculated P_{RI} vs. $v_p^{1/2}$ of methane (triangles) for the model live oil at 20.0°C.

Because the observed instability onset pressures are nearly linear functions of mixture gas concentration at each temperature, it may be possible to trace out the asphaltene stability boundaries with only a small set of instability onset data. Furthermore, for this particular source asphaltenes, the effect of temperature on the asphaltene instability boundary seems to be systematic (i.e. increasing temperature improves asphaltene solvency in oil) and temperature extrapolation may be possible.

From an operational standpoint, results of this study suggest that the oil refractive index may be used to estimate whether or not asphaltenes would precipitate. Along the asphaltene instability boundaries, these properties should vary little regardless of pressure and composition. At a constant temperature, asphaltenes would be stable as long as the mixture was above a certain solubility threshold, as indicated by the mixture refractive index or solubility parameter. In an isothermal pressure depletion operation, asphaltenes would be initially stable at pressures high above the bubble point pressure due to high solvent density. As pressure decreases, the density of the oil will decrease (which can be seen by the lowering of the oil refractive index) as the solubility environment becomes increasingly unfavorable for asphaltene dissolution. Asphaltenes may precipitate out of solution below a certain refractive index threshold near the oil bubble point. Finally, as the pressure decreases further below the bubble point, the oil refractive index would increase (due to composition changes) and asphaltenes

may become stable again. This behavior is seen in Figure 3.10, where the calculated mixture refractive indices were plotted as a function of pressure for the model live oil at 20.0°C with 0.143 mass fraction methane above the bubble point.

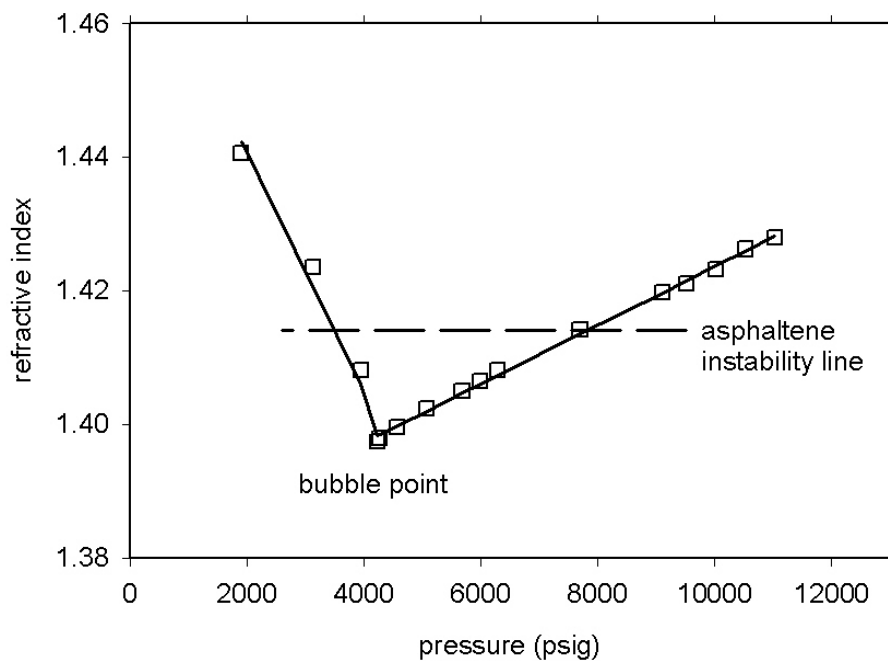


Figure 3.10 Mixture refractive indices during pressure depletion for the model live oil at 20.0°C with 0.143 mass fraction methane above the bubble point. Asphaltenes are unstable below the asphaltene instability line.

3.5 Summary

The asphaltene instability and bubble point curves of a recombined oil and a model live oil were measured as functions of pressure, temperature, and dissolved gas concentration. Significant temperature effects on asphaltene stability were observed, and increasing the temperature of the system seemed to

improve asphaltene stability. At each temperature, the asphaltene instability onset pressures were nearly linear functions of mixture gas concentration. This suggests that the asphaltene instability boundaries can be roughly estimated from a few data points.

An analysis of the data shows that at a constant temperature, the mixture refractive indices do not change much along the asphaltene instability curves. From an operational stand point, this means that it may be possible to estimate the degree of asphaltene stability from a crude oil's refractive index (or solubility parameter).

Finally, for the systems tested, there is a clear connection between asphaltene precipitation in the titration experiments at ambient conditions and in the reservoir depressurization experiments. This is indicated at 20°C by the near linear relationship between the mixture P_{RI} and the square root of the effective molar volume of the precipitants. Hence an equation of state that can match the results of the titration experiments at ambient conditions should be able to estimate the effects of pressure on asphaltene stability in crude oil.

CHAPTER 4. EQUATION OF STATE ALGORITHMS

4.1 Introduction

In this chapter, we will develop the theoretical tools to be used in the asphaltene phase behavior investigations. We will start with a description of the Statistical Associating Fluid Theory (SAFT) equation of state that includes a discussion on its limitations. SAFT-predicted thermodynamic properties of some pure fluids will be compared with experimental data or molecular simulation data to show the equation of state's ability to accurately model the thermodynamic properties of molecular species relevant in this work. A list of pure component SAFT parameters for compounds relevant in this work is also presented together with the methodology used to obtain them. An analysis of these parameters shows distinct trends in their behavior with molecular weight. The implications of these observed trends are discussed.

Since the SAFT equation of state is used to describe fluids and fluid mixtures in all phases, an algorithm is needed to determine equilibrium phase compositions from calculated free energies. Issues associated with mixture phase equilibrium calculations will be discussed and several algorithms investigated in terms of their speed and range of applicability. Finally, a hybrid phase stability-modified flash algorithm that is both robust and efficient is presented. This algorithm is used in all calculations presented in this thesis.

4.2 The SAFT Equation of State

A variety of approaches have been developed to describe the thermodynamic phase behavior of molecular fluids and fluid mixtures. These approaches include the use of perturbation theory, integral equation theory, scaled particle theory, molecular simulations, lattice theory, local composition theory, and correlative models such as the van Laar equations to describe fluid properties.^[24,47,48] Of these approaches, the use of thermodynamic perturbation theory is especially popular because of its theoretical basis, its fast computation time, its accuracy, and its wide range of applicability.

In perturbation theory, the properties of a fluid are obtained by expanding about the same properties of a reference fluid. It is assumed that the reference fluid roughly describes the fluid of interest; the perturbation is a series of small corrections to the reference. For instance, in one of the most well known (and together with virial expansion method the earliest) examples of this approach, van der Waals added a perturbation to the pressure of a hard-sphere fluid to account for intermolecular attraction:^[48]

$$\frac{P}{kT} = \frac{\rho}{1-b\rho} - \frac{a\rho^2}{kT} \quad (4.1)$$

In Eqn. 4.1, P is pressure, k is the Boltzmann constant, T is temperature, ρ is density, and a , b are constants that account for intermolecular attraction and hard-sphere fluid repulsion, respectively.

Since van der Waals published his monumental work in 1873^[49], much activity have been devoted to the application of perturbation theory methods to model dense fluids. These activities fall under one of two categories: (1) semi-empirical modifications to Eqn. 4.1 to better reproduce experimental data of real fluids and (2) application of statistical mechanics to the perturbation expansions of molecular pair potentials to obtain fluid properties. An example of the first approach is the Peng-Robinson (PR) equation^[50]. And an example of the second approach is the thermodynamic perturbation theory for square-well fluids and for Lennard-Jones fluids due to Barker and Henderson.^[51,52] While the first approach is popular in industry because of its wide applicability and mathematical simplicity, the second approach is favored by academics because it allows one to test the effects of different pair potential functions on bulk fluid properties. However, the second approach is complicated for molecules that have anisotropic potentials.

SAFT, an acronym for Statistical Associating Fluid Theory, is a statistical mechanical equation of state developed from Wertheim's first order perturbation theory (TPT1).^[53-59] By treating a mixture of associating spheres as a mixture of differently associated species (monomers, dimers, etc.), Wertheim used a perturbation expansion in terms of the monomer and overall fluid density (about the hard sphere reference) to calculate the free energy contribution due to bonding. The assumptions used in TPT1 are (see Figure 4.1): (1) the hard cores

of two molecules bonded at sites A (a site on one molecule) and B (a site on the second molecule) would prevent sites on a third molecule from bonding with these sites, (2) no double bonding can occur, (3) a site on a molecule cannot simultaneously bond to two sites on another molecule, and (4) each molecular segment does not know the location of other segments not directly bonded to it (and thus SAFT cannot explicitly model ring formation). The last assumption is the result of first order approximation. Derivation of Wertheim's theory can be found in Joslin, *et al*^[60] or in the works by Wertheim.^[56-59]

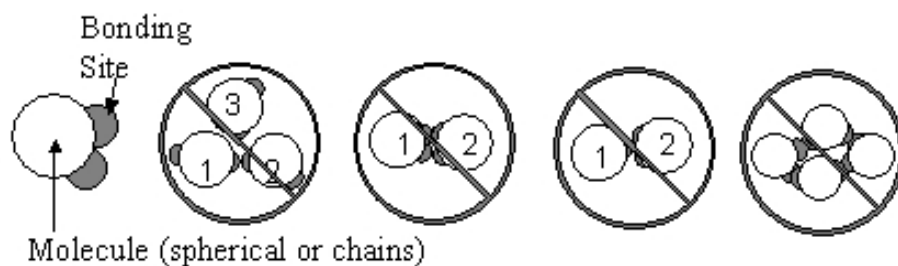


Figure 4.1 Assumptions and limitations of the SAFT EOS.

As a perturbation theory, SAFT considers the fluid of interest to be initially a mixture of independent segments. The theory predicts the change in free energy upon bonding these segments to form chains and on the further association of the chain-like molecules (Figure 4.2) using TPT1 theory. In this work, we use a hard-sphere contribution from the Mansoori-Carnahan-Starling-Leland (MCSL) hard-spheres equation of state^[61], chain formation and association contributions from Wertheim theory^[55], and mean field contribution from Gross and Sadowski^[62]. SAFT requires three parameters for each nonassociating component. These parameters are the temperature independent

diameter of each molecular segment (σ), the number of segments per molecule (m), and the segment-segment dispersion energy (ε/k).

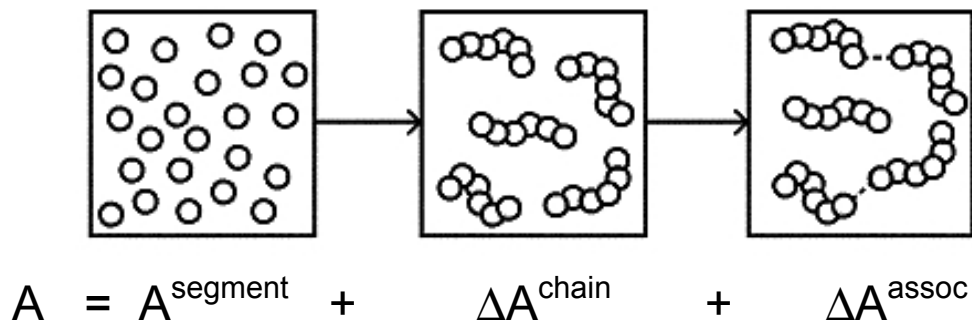


Figure 4.2 In SAFT, fluids are initially considered to be a mixture of independent segments that are then bonded to form chains.

The residual Helmholtz energy A^{res} of a fluid mixture is described by SAFT as

$$\frac{A^{res}}{RT} = \frac{A^{seg}}{RT} + \frac{A^{chain}}{RT} + \frac{A^{assoc}}{RT} = m \frac{A_o^{hs}}{RT} + m \frac{A_0^{disp}}{RT} + \frac{A^{chain}}{RT} + \frac{A^{assoc}}{RT} \quad (4.2)$$

where A^{seg} , A^{chain} , A^{assoc} , A_o^{hs} , A_0^{disp} are the segment, chain, association, segment hard sphere, and segment dispersion contributions to the residual Helmholtz energy. A^{res} is called a residual property because it is defined as the energy of the fluid minus that of an ideal gas at the same temperature and density. The average segment number of the mixture m is an average of the pure species segment numbers m_i weighted by their compositions:

$$m = \sum_i x_i m_i \quad (4.3)$$

The free energy contribution of the hard-sphere mixtures (from the MCSL EOS) is

$$\frac{A_o^{hs}}{RT} = \frac{6}{\pi\rho} \left[\frac{\zeta_2^3 + 3\zeta_1\zeta_2\zeta_3 - 3\zeta_1\zeta_2\zeta_3^2}{\zeta_3(1-\zeta_3)^2} - \left(\zeta_o - \frac{\zeta_2^3}{\zeta_3^2} \right) \ln(1-\zeta_3) \right] \quad (4.4)$$

$$\text{where } \zeta_k = \left(\frac{\pi}{6} \rho \right) \sum x_i m_i d_{ii}^k \quad (4.5)$$

$$\text{and } d_{ii} = \sigma_i [1 - 0.12 \exp(-3\varepsilon_i / kT)] \quad (4.6)$$

Here, ρ is the number density (molecules/A³), σ_i is the temperature-independent segment diameter of species i in units of Angstroms, and d_{ii} is the temperature-dependent segment diameter. The contribution to A due to chain formation is given by^[53]

$$\frac{A^{Chain}}{RT} = \sum x_i (1 - m_i) \ln g_{ii}^{hs}(d_{ii}) \quad (4.7)$$

$$\text{where } g_{ii}^{hs}(d_{ii}) = \left[\frac{1}{1-\zeta_3} + \frac{3d_{ii}}{2} \frac{\zeta_2}{(1-\zeta_3)^2} + 2 \left(\frac{d_{ii}}{2} \right)^2 \frac{\zeta_2^2}{(1-\zeta_3)^3} \right] \quad (4.8)$$

A comparison of SAFT-predicted compressibility factor (Z) with simulation results for flexible hard-sphere chains show good agreement^[53] (Figure 4.3), indicating that SAFT is a good model for hard-chain molecules.

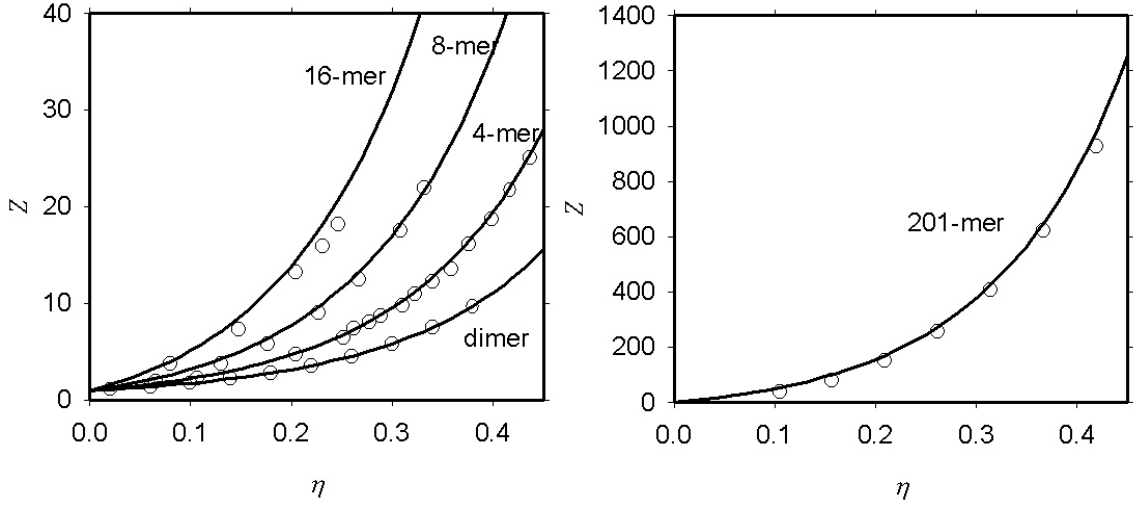


Figure 4.3 Comparison of SAFT-predicted compressibility factor Z as a function of packing fraction η with simulation results.^[53] The simulation data are from Dickman and Hall^[63] (dimer to 16-mer) and from Gao and Weiner^[64] (201-mer).

For fluid or fluid mixtures that are not comprised of hard-sphere chains, an energy contribution is added to account for dispersion interactions. As mentioned earlier, the dispersion contribution of Gross and Sadowski^[65] is used in this work. This particular dispersion term was initially developed for alkanes by incorporating the effects of chain length on the segment dispersion energy ε/k .

Thus

$$\frac{A_o^{disp}}{RT} = \frac{A_1}{RT} + \frac{A_2}{RT} \quad (4.9)$$

$$\frac{A_1}{RT} = -2\pi\rho I_1(\eta, m) \sum_i \sum_j x_i x_j m_i m_j \sigma_{ij}^3 \varepsilon_{ij} / kT \quad (4.10)$$

$$\frac{A_2}{RT} = -\rho\pi m I_2(\eta, m) W^{-1} \sum_i \sum_j x_i x_j m_i m_j \sigma_{ij}^3 (\varepsilon_{ij} / kT)^2 \quad (4.11)$$

$$W = 1 + m \frac{8\eta - 2\eta^2}{(1-\eta)^4} + (1-m) \frac{20\eta - 27\eta^2 + 12\eta^3 - 2\eta^4}{[(1-\eta)(2-\eta)]^2} \quad (4.12)$$

$$\varepsilon_{ij} = (1 - k_{ij}) \text{sqrt}(\varepsilon_{ii} \varepsilon_{jj}) \quad (4.13)$$

$$\sigma_{ij} = 0.5(\sigma_i + \sigma_j) \quad (4.14)$$

where l_1 and l_2 are functions of the system packing fraction and average segment number m and can be found in the work by Gross and Sadowski^[65]. k_{ij} corrects for deviations in the mixing of the pure component energies ε from that predicted by the geometric mixing rule. Equation 4.9 was derived in the spirit of Barker-Henderson perturbation theory and, as such, A_1 and A_2 correspond to the first and second order contributions to A_0^{disp} , respectively. Other dispersion contributions can be used instead of the one given in Eqns. 4.9 to 4.14. The form of SAFT described above is sometimes referred to in literature as PC-SAFT (perturbed-chain SAFT) because the dispersion contribution accounts for the effects of chain length on the segment dispersion energy.

Because of our assumption that nonpolar van der Waals interactions dominate asphaltene phase behavior in crude oil (Chapter 2), the association term in SAFT will not be used in our asphaltene modeling work. A detailed discussion of the SAFT association term will be deferred to Chapter 10, where we present some modifications to model hydrogen bonding interactions in water.

With the expressions for A^{res} given in Eqns. 4.2 to 4.14, all other residual thermodynamic properties can be calculated. For instance, $S/R = -(\partial A/RT/\partial T)_{v,n}$ where S is entropy, $U/RT = A/RT + S/R$ where U is internal energy, and $\delta \approx (U^{\text{rsm}} \rho RT)^{0.5}$ where δ is the solubility parameter.^[24]

SAFT and its various modifications and extensions have demonstrated the ability to accurately predict the phase behavior of simple, hydrogen bonding, polar, and polymeric mixtures.^[66,67] It is particularly useful for modeling systems with significant size, shape, and/or association effects. One reason for this success is due to SAFT's ability to reproduce and predict accurately the thermophysical properties of pure species and of mixtures. For example, a comparison of SAFT-predicted and experimental^[45] solubility parameters of some n-alkanes, polynuclear aromatics, cycloalkanes, benzene derivatives, and carbon disulfide at 25°C and 1 bar shows good agreement (Figure 4.4). A comparison of SAFT-predicted and experimental liquid volumes of hexadecane (n-C₁₆), tetracosane (n-C₂₄), and hexatriacontane (n-C₃₆) at 1 bar also shows good agreement^[68] (Figure 4.5). In contrast, a cubic equation of state such as Peng-Robinson equations does not predict the correct volumes for the longer n-alkanes because it does not correctly account for the effects of molecular size.

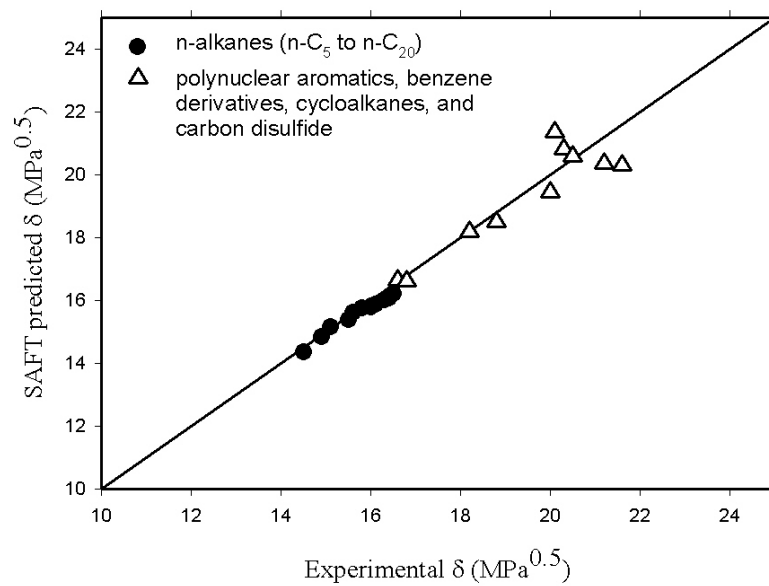


Figure 4.4 Comparison of SAFT-predicted and experimental^[45] solubility parameters at 25°C and 1 bar.

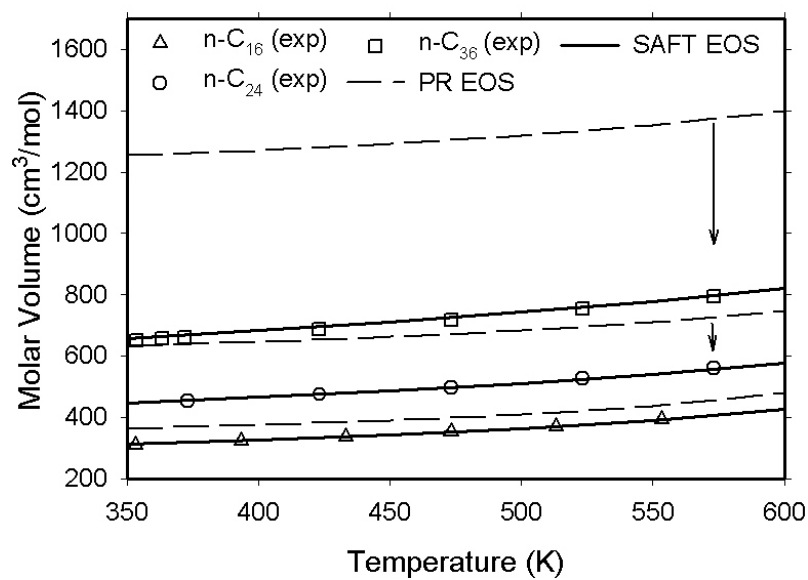


Figure 4.5 Comparison of SAFT-predicted, Peng-Robinson EOS-predicted, and experimental liquid molar volumes at 1 bar^[68].

4.3 Reference State Conversions

Because the terms in Eqn. 4.2 were obtained by perturbation expansions about the fluid's density at constant temperature, these two intensive variables are the natural reference variables for SAFT. However, it is the Gibbs energy (which has temperature and pressure as its reference variables) that has been used traditionally to examine phase stability. To change the reference state of the energies from one that is residual to an ideal gas at the same T and ρ to one that is residual to an ideal gas at the same T and P , we can write

$$A^{res}(P, T) = A^{res}(\rho, T) - nRT \ln Z \quad (4.15)$$

$$U^{res}(P, T) = U^{res}(\rho, T) \quad (4.16)$$

$$H^{res}(P, T) = H^{res}(\rho, T) \quad (4.17)$$

$$G^{res}(P, T) = G^{res}(\rho, T) - nRT \ln Z \quad (4.18)$$

$$S^{res}(P, T) = S^{res}(\rho, T) + nR \ln Z \quad (4.19)$$

$$\mu_i^{res}(P, T) = \mu_i^{res}(\rho, T) - RT \ln Z \quad (4.20)$$

$$\ln \phi_i = \mu_i^{res}(\rho, T) - \ln Z \quad (4.21)$$

where n is the number of moles, U is internal energy, H is enthalpy, G is Gibbs energy, S is entropy, Z is compressibility factor, and μ and ϕ are the chemical potential and fugacity coefficient of species i . Hence given a set of SAFT parameters (m , σ , and ϵ/k) for a pure fluid (or a fluid mixture), we can describe all thermodynamic properties of the fluid in the liquid and vapor phases.

4.4 SAFT Equation of State Parameters

The pure component SAFT parameters used in this work are listed in Table 4.1. These parameters were either tabulated by Gross and Sadowski^[65] or obtained in this work by regressing to the substance's experimental saturated vapor pressures (P_i^{sat}) and liquid densities (ρ_i^{liq}):

$$\min_{\sigma, m, \epsilon/k} \frac{1}{2} \sum_{i=1}^{ndp+ndp} f_i(\sigma, m, \epsilon/k, P_i^{sat} \text{ or } \rho_i^{liq})^2 \quad (4.22)$$

$$\text{where } f_i = \frac{P_i^{sat, calc} - P_i^{sat, exp}}{P_i^{sat, exp}} \quad \text{for } i = 1 \text{ to } ndp$$

$$f_i = \frac{\rho_i^{liq, calc} - \rho_i^{liq, exp}}{\rho_i^{liq, exp}} \quad \text{for } i = ndp+1 \text{ to } ndp+ ndp$$

The experimental data used in the regression were obtained from the DIPPR database^[69]. As is typical of analytic equations of state, SAFT tends to overpredict critical temperatures and pressures. Because of this, data in the critical region were not used in the fitting procedure.

Table 4.1 SAFT pure component parameters. For substances fitted in this work, the AAPDs^a and temperature range of the experimental data^[69] are given. All other SAFT parameters are from Gross and Sadowski.^[65]

Substance	MW (g/mol)	m	σ (Å)	ϵ/k (K)	T range (K)	AAPD ^a P^{sat} ρ^{liq}
n-alkanes						
methane	16.04	1.0000	3.7039	150.03		
ethane	30.07	1.6069	3.5206	191.42		
propane	44.09	2.0020	3.6184	208.11		
butane	58.12	2.3316	3.7086	222.88		
pentane	72.15	2.6896	3.7729	231.20		
hexane	86.18	3.0576	3.7983	236.77		
heptane	100.20	3.4831	3.8049	238.40		
octane	114.23	3.8176	3.8373	242.78		
nonane	128.25	4.2079	3.8448	244.51		

decane	142.29	4.6627	3.8384	243.87			
undecane	156.31	4.9082	3.8893	248.82			
dodecane	170.34	5.3060	3.8959	249.21			
tridecane	184.37	5.6877	3.9143	249.78			
tetradecane	198.39	5.9002	3.9396	254.21			
pentadecane	212.42	6.2855	3.9531	254.14			
hexadecane	226.45	6.6485	3.9552	254.70			
eicosane	282.55	7.9849	3.9869	257.75			
cycloalkanes							
cyclopentane	70.13	2.3655	3.7114	265.83			
methyl-cyclopentane	84.16	2.6130	3.8253	265.12			
ethyl-cyclopentane	98.18	2.9062	3.8873	270.50			
cyclohexane	84.15	2.5303	3.8499	278.11			
methyl-cyclohexane	98.18	2.6637	3.9993	282.33			
ethyl-cyclohexane	112.22	2.8256	4.1039	294.04			
cycloheptane	98.19	2.6870	3.9352	296.15	300-570	0.44	0.21
cyclooctane	112.22	2.9222	4.0028	304.67	300-620	0.71	1.06
polynuclear aromatics							
benzene	78.11	2.4653	3.6478	287.35			
naphthalene	128.17	3.0915	3.8333	348.40	373-633	1.45	0.77
anthracene	178.23	3.5291	4.0922	402.13	500-830	1.81	1.57
phenanthrene	178.23	3.4890	4.1053	403.06	330-780	1.51	1.39
naphthacene	228.29	4.6432	3.8942	407.60	660-940	0.88	4.23
chrysene	228.29	5.1201	3.8400	385.73	580-940	0.81	3.61
pyrene	202.26	3.6847	4.1151	427.35	450-850	1.37	3.76
aromatic & polynuclear aromatics derivatives							
toluene	92.14	2.8149	3.7169	285.69			
ethylbenzene	106.17	3.0799	3.7974	287.35			
propylbenzene	120.19	3.3438	3.8438	288.13			
butylbenzene	134.22	3.7662	3.8727	283.07			
tetralin	132.21	3.3131	3.8750	325.07			
biphenyl	154.21	3.8877	3.8151	327.42			
1-methylnaphthalene	142.20	3.4064	3.8961	345.71	393-673	0.29	0.50
1-phenylnaphthalene	204.27	4.7634	3.8582	336.53	330-780	1.51	1.39
m-terphenyl	228.29	5.6273	3.7967	329.18	420-840	1.52	0.26
gases							
nitrogen	28.01	1.2053	3.3130	90.96			
carbon dioxide	44.01	2.0729	2.7852	169.21			
carbon disulfide	76.14	1.6919	3.6172	334.82			

$$a \text{ Average absolute percent deviation} = \frac{1}{ndp} \sum_{ndp} \left| \frac{\text{Calculated} - \text{Experimental}}{\text{Experimental}} \right| 100\%$$

An important feature of SAFT is that the fitted pure component parameters behave in a systematic manner with molecular weight for each class of compounds^[62,70] (Figure 4.6, Table 4.2). Furthermore, species with both aromatic and aliphatic characteristics have EOS parameters that lie in between the aromatic and n-alkane correlations in a systematic manner depending on their degree of aromaticity. For instance, the variation of m with molecular weight for some benzene derivatives and cyclo-alkanes are shown in Figure 4.7; as the degree of aliphaticity increases, the pure component parameters more closely resembles those for the n-alkanes. These correlations between the pure component parameters and molecular weight have three implications. (1) The correlations can be used to estimate the SAFT parameters for substances whose vapor pressures and/or liquid densities are difficult to measure. For example, the SAFT-predicted liquid molar volumes of hexatriacontane (n-C₃₆) in Figure 4.5 were calculated using n-C₃₆ SAFT parameters extrapolated from the n-alkane correlations. In the case of asphaltenes, these correlations provide the upper and lower bounds of the asphaltene SAFT parameters. (2) Systems that are polydisperse in molecular size (with molecular weight) can be modeled in SAFT as a single pseudo-component. And (3) the pure component SAFT correlations imply that the EOS can be extended to explicitly model (rather than using a pseudo-component scheme) the effects of polydispersity. Each of these will be discussed in more detail in the following chapters.

Table 4.2 SAFT pure component parameter correlations.

	n-alkane saturates	polynuclear aromatics
m	$0.0253MW+0.9263$	$0.0139MW+1.2988$
$m\sigma$	$0.1037MW+2.7985$	$0.0597MW+4.2015$
ε/k	$32.81\ln(MW)+80.398$	$119.41\ln(MW)-230.21$

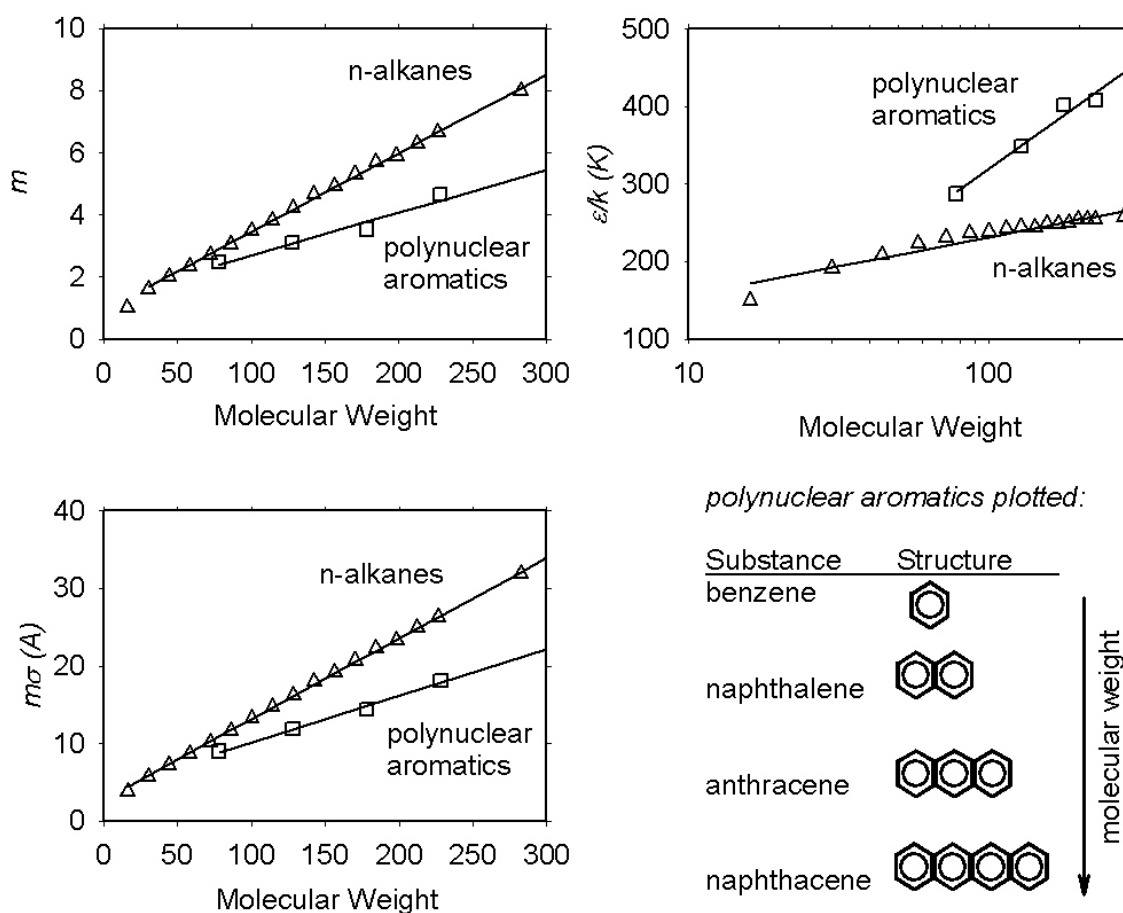


Figure 4.6 Plots of SAFT pure component parameters with molecular weight. The parameter correlations in Table 4.2 are shown as lines.

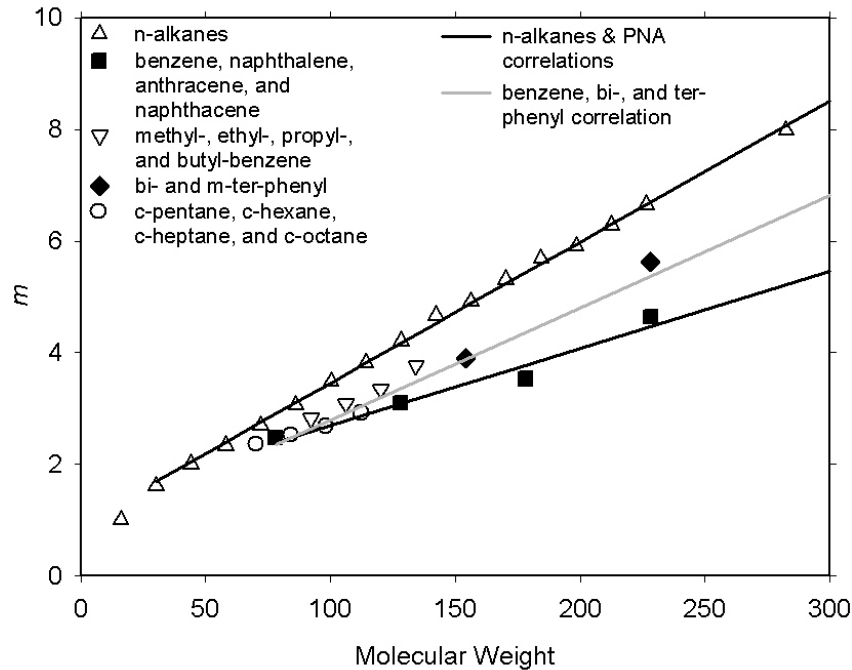


Figure 4.7 Variation of m with molecular weight for various compounds.

4.5 Phase Stability and Flash Algorithms

Equilibrium is a condition in which the system's macroscopic properties do not change with time because all the energy that may cause change are balanced.^[49] The necessary and sufficient condition for thermodynamic phase equilibrium (at a fixed T and P) is that the overall Gibbs energy of the mixture is at its global minimum^[49]:

$$\min_{n_{ij}} G = \sum_{i,j} n_{ij} \mu_{ij}(T, P, \underline{n}_j) \quad (4.23)$$

where the underscore denotes vector quantities and the summation is over all components i and all phases j . The necessary condition at equilibrium is

$$T^\alpha = T^\beta = \dots = T^\pi$$

$$P^\alpha = P^\beta = \dots = P^\pi$$

$$\mu_{i\alpha} = \mu_{i\beta} = \dots = \mu_{i\pi} \quad (i=1,2,\dots,n) \quad (4.24)$$

where $\alpha, \beta, \dots, \pi$ are the different phases and n is the total number of components. Eqn. 4.24 is the first order necessary condition of Eqn. 4.23 obtained by first differentiating Eqn. 4.23 and then applying the Gibbs-Duhem relation. Eqn. 4.24 can also be expressed as an equality of fugacities

$$f_{i\alpha} = f_{i\beta} = \dots = f_{i\pi} \quad (4.24')$$

because

$$\mu_i(\underline{n}, T, P) = \mu_i^0(T, P) + RT \ln f_i(\underline{n}, T, P) - RT \ln f_i^0(T, P) \quad (4.25)$$

and the fugacity and chemical potential of the pure components f_i^0, μ_i^0 depend only on temperature and pressure. The second order derivatives of the Gibbs energy with composition (which provides the sufficiency condition) depends on the EOS used to calculate the thermodynamic properties and are difficult to determine analytically for SAFT.

The direct minimization of the function G in (4.23) is difficult because the number of phases present is not known a priori and the equations of state used to calculate the chemical potentials of these nonideal mixtures are nonlinear. Optimization methods such as interval analysis^[71], simulated annealing^[38], the RAND method^[72], genetic algorithms^[73], and random search algorithms^[74] have all been used to solve (4.23) directly. The application of the interval analysis method seems especially promising, as the authors claim that their algorithm is guaranteed to find the global minimum.^[71] However, the robustness that these algorithms offer comes at the expense of efficiency. For instance, equilibrium

(binary) phase compositions of a mixture of ethane and eicosane (outside the mixture critical region) took about a minute of CPU time while a mixture of heptane and propanol (outside the mixture critical region) took more than 6 minutes on a Sun Ultra 10/440.^[71]

An alternative approach to determine equilibrium phase compositions is to use the constant temperature and pressure flash (also called the successive-substitution method). This approach is called a flash because it simulates the flashing of a one-phase mixture into a tank at T and P to see if the fluid would phase separate. The number of phases at equilibrium, the feed composition, an initial estimate of the compositions of all phases, T , and P must be given a priori. The algorithm for a vapor-liquid flash^[49,75] is shown in Figure 4.8. In the figure, $\{z\}$, $\{x\}$, and $\{y\}$ are the set of feed, liquid, and vapor phase compositions. K_i is the partition coefficient of the i th species, V is the ratio of the amount of vapor to the feed, and ϕ_i is the fugacity coefficient (recall Eqn. 4.24' and $(f_i = \phi_i x_i P)$). The equations shown in the figure to evaluate V , $\{x\}$, and $\{y\}$ are mass balance constraints. Since the function used to determine V is a monotonically decreasing function between $V=0$ and $V=1$, it can be evaluated easily. An extension of the algorithm to three phase calculations can be found in the work of Nelson^[76].

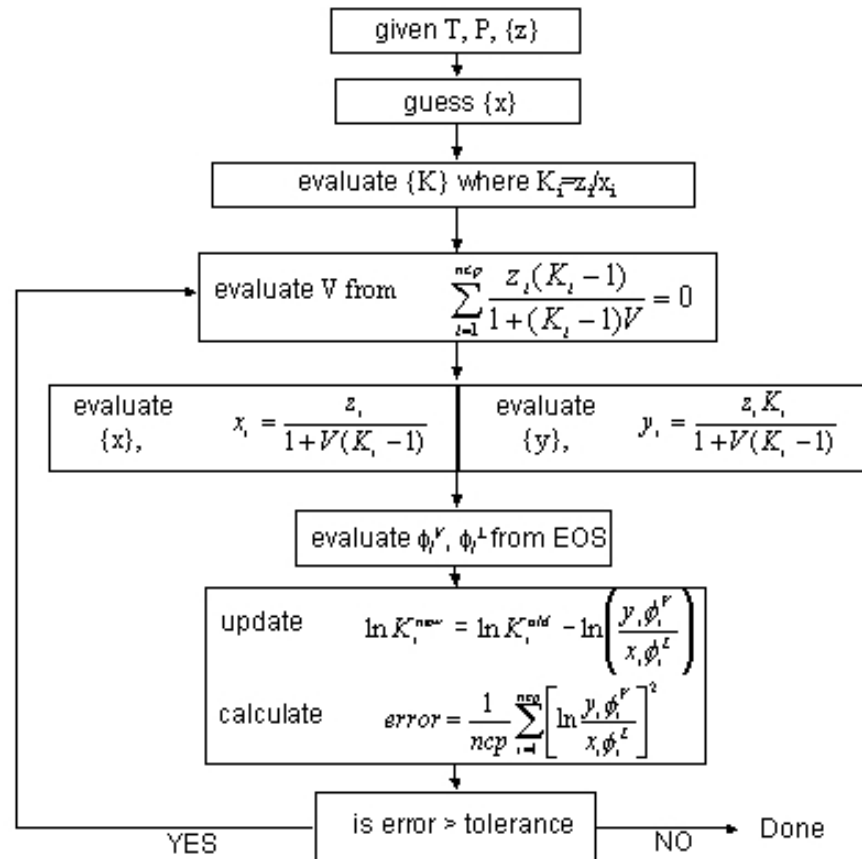


Figure 4.8 Calculation procedure in a typical TP flash algorithm^[49].

Unlike the direct Gibbs energy minimization approaches, the correct number of phases at equilibrium must be specified a priori for the solution of the flash to be meaningful. Furthermore, an initial guess for the equilibrium composition may return a trivial solution (which indicates a stable state) even if the state point is not stable, and multiple initial guesses for the equilibrium composition may be needed to determine stability. These and other problems are illustrated in Figure 4.9, where compositions at phase equilibrium are connected by tangents to the ΔG^{mix} curves (on the right hand side figures). Since the first derivative of ΔG^{mix} with respect to a component's mole number is its

chemical potential, the lines in Figure 4.9 satisfy the requirement of Equation 4.24. At pressure P_2 , a feed of composition z_2 would phase split into 3 phases. However, if one specified the number of phases to be 2, then the incorrect binary phase compositions of x_2^{Lb} and x_2^G would be obtained. At pressure P_1 , the system exists as either a single gas phase, a single liquid phase, or as a liquid and gas in equilibrium. The flash would converge to the solution x_2^{La} and x_2^G if a feed z_2 is used but would return the trivial solution if a feed of z_2^* is used. At pressure P_4 , the flash would converge to the trivial solution regardless of the feed composition. Finally, the tangent lines at P_3 illustrate the difficulties one may encounter in obtaining the correct phase equilibria compositions. While all three tangent lines at P_3 satisfy Eqn. 4.24, the compositions on the solid line are the only real solution.

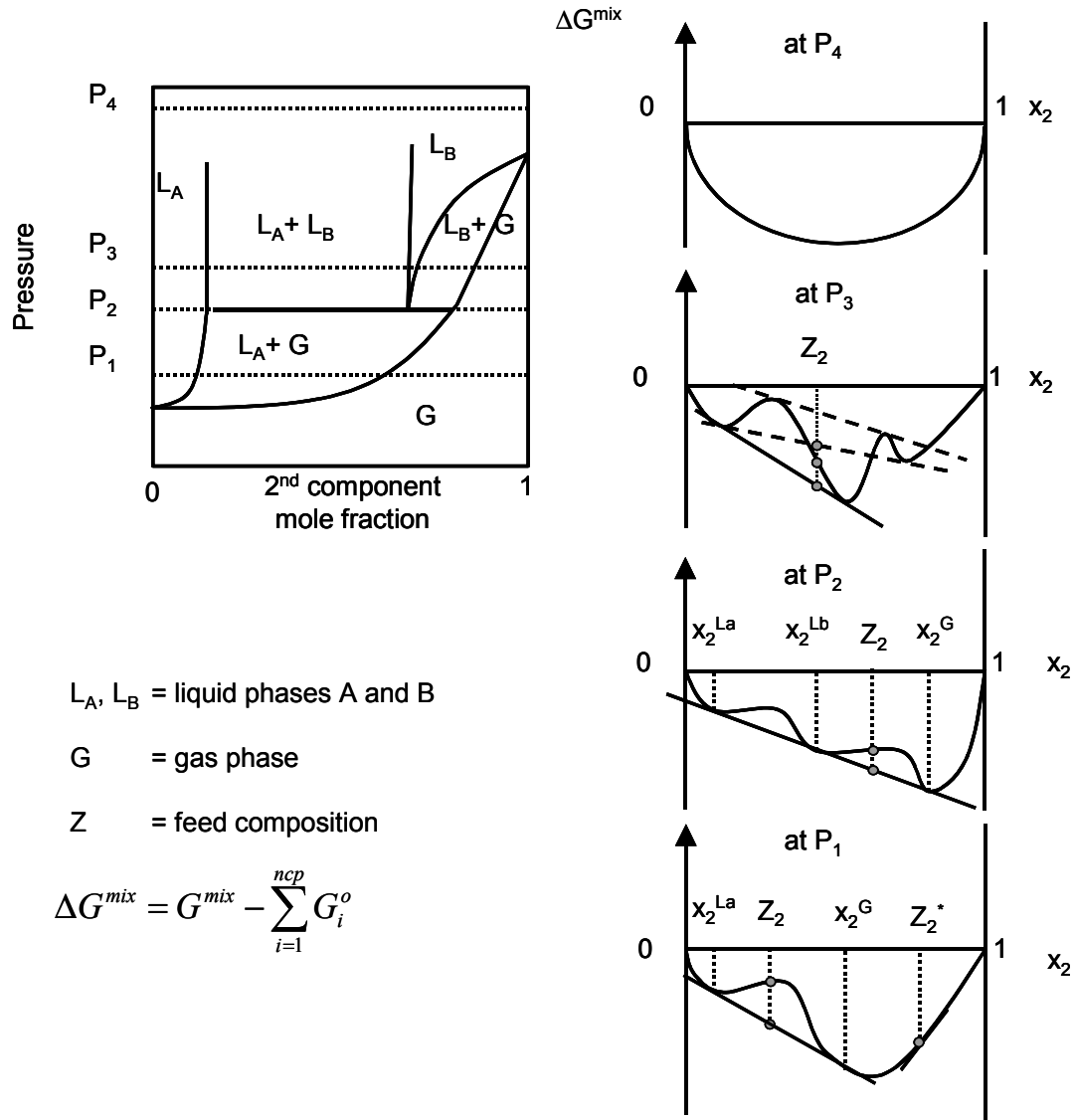


Figure 4.9 Change in the Gibbs energy of mixing for a binary mixture at various pressures and compositions. The pressure-composition diagram is given on the left and energy-composition diagrams for various pressure cuts on the right.

The flash algorithm of Figure 4.8 is equivalent to applying the steepest descent method to solve Eqn. 4.23 with a step length of one.^[77] The updating scheme for $\ln(K)$ for a binary mixture in Figure 4.8 can be written as

$$\ln K_j^{new} - \ln K_j^{old} = \Delta \ln K_j = \ln f_{j,liq}^{old} - \ln f_{j,vap}^{old}$$

(using Eqn. 4.23 and 4.25)

$$= -\frac{\partial G/RT}{\partial n_{j,\text{liq}}} = -g_j$$

so that

$$\underline{\Delta \ln K} = -\alpha_k \underline{\underline{B}}_k^{-1} \underline{g}_k \quad (4.26)$$

In Eqn. 4.26, k is the iteration number, the single underscore denotes vectors, and the double underscore denotes matrices. $\underline{\underline{B}}_k^{-1}$ in this case is the identity matrix I and α_k is one. Moreover, since the mole numbers \underline{n}_j for phase j is related to the equilibrium ratios \underline{K} (because the feed was specified a priori), we can rewrite Eqn. 4.26 for a two phase mixture as

$$\underline{\Delta n}_j = -\alpha \underline{\underline{U}}^{-1} \underline{\underline{B}}^{-1} \underline{g} \quad (4.26')$$

Since $\underline{\underline{U}}$ and its inverse are positive definite, the flash algorithm would always move in the direction of decreasing Gibbs energy.

While Gibbs energy minimization is superior to the flash formulation because the latter cannot guarantee convergence to the global solution, the computation costs associated with the global methods are often much higher. For instance, the interval method would give reliable solutions to (4.23) while a quasi-Newton method would be more efficient but does not guarantee convergence to the global solution. Ohanomah and Thompson^[78] compared more than ten algorithms and reported that direct Gibbs energy minimization schemes are not competitive in practice because of their added complexity and computation time.

In this work, we used a two-prong approach to improve the algorithm in Figure 4.8. A phase stability algorithm was added to a modified flash algorithm to improve efficiency and robustness. The proposed procedure is shown in Figure 4.10. Succinctly, a given feed is first checked for phase stability using the tangent plane method (to be discussed shortly). If the feed is unstable, the composition given by the stability algorithm (with which the feed are unstable to) is used with the feed composition to determine \underline{K} guesses for the two-phase flash. After the two-phase flash has converged, the calculated equilibrium phase compositions are tested for stability. If they are unstable, the process is first repeated with new feed compositions. If subsequent stability-flash calculations return the same false “equilibrium” compositions, the feed and the compositions calculated by the two-phase flash are then used to construct initial \underline{K} estimates for the three-phase flash. This cycle of flash calculation followed by stability check continues until a stable solution has been obtained. The notion of coupling a phase stability algorithm with a local optimization algorithm was first proposed by Michelsen^[79,80]. And the idea of modifying the flash with line search, trust region, or quasi-Newton methods was first investigated in the 1970s with the development of reservoir and plant simulators.

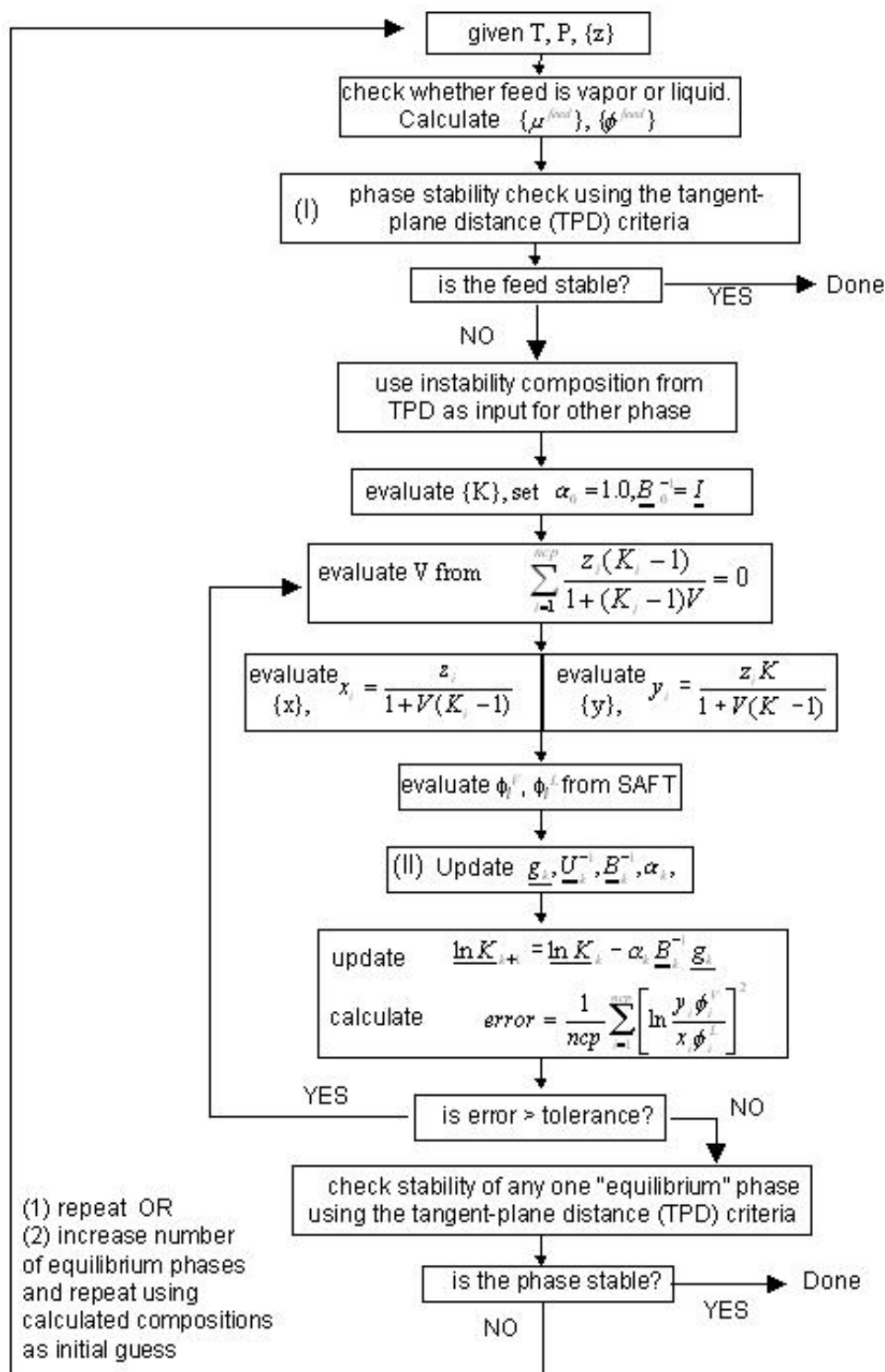


Figure 4.10 Proposed phase equilibria calculation procedure.

Three modifications to the flash algorithm were investigated. (1) We kept the steepest descent algorithm of Eqn. 4.26 with $\underline{\underline{B}}_k^{-1} = I$ but optimized α at each iteration k : $\min_{\alpha > 0} G(T, P, \underline{n}_k + \alpha_k \underline{g}_k)$ using the golden section algorithm with a tolerance of 10^{-5} and $0 < \alpha \leq 20$. (2) We set $\underline{\underline{B}}_k^{-1} = I$ and calculated the step length at each iteration after the first using^[77]

$$\alpha_k = \left(\frac{\underline{g}_{k-1}^T \underline{\underline{U}}^{-1} \underline{g}_{k-1}}{\underline{g}_{k-1}^T \underline{\underline{U}}^{-1} (\underline{g}_{k-1} - \underline{g}_k)} \right) \alpha_{k-1} \quad (4.27)$$

where the elements of $\underline{\underline{U}}^{-1}$ are

$$u_{ij}^{-1} = \left(\frac{V(1-V)}{1} \right) \left(\frac{x_i y_i}{z_i} \right) \left(\delta_{ij} + \left(\frac{x_j y_j}{z_j} \right) \left(\frac{1}{1 - \sum_k^n [x_k y_k / z_k]} \right) \right) \quad (4.28)$$

for the two phase system. Eqn. 4.27 was obtained by first Taylor expanding the Gibbs energy and then setting the derivative of the truncated expansion with α to 0. Eqn. 4.28 relates changes in composition to changes in K values assuming that the total amount of vapor and liquid is one mole. (3) We used the golden section algorithm to optimize α (as in the first approach) and updated $\underline{\underline{B}}_k^{-1}$ using the Broyden-Fletcher-Goldfarb-Shanno method^[81]

$$\underline{\underline{B}}_{k+1} = \underline{\underline{B}}_k - \frac{\underline{\underline{B}}_k \Delta \ln K_k \Delta \ln K_k^T \underline{\underline{B}}_k}{\Delta \ln K_k^T \underline{\underline{B}}_k \Delta \ln K_k} + \frac{\underline{g}_k \underline{g}_k^T}{\underline{g}_k^T \Delta \ln K_k} \quad (4.29)$$

with $\underline{\underline{B}}_0 = I$. $\underline{\underline{B}}$ was calculated once every 4 iterations to reduce computation time.

A comparison of the various flash algorithms on some representative, extremely nonideal binary mixtures is given in Table 4.3. The systems investigated include binary mixtures of hexane and hexatriacontane, hexane and 25,000 MW polystyrene, hexane and 33,000 MW polyethylene-octene, and methanol and pentane. The effectiveness of these algorithms in the mixture critical region is also tested. Keep in mind that all perturbation methods will fail at the critical point.

As seen in Table 4.3, the second modification was overall the most robust and the fastest. The algorithm of Modification 1 required few iterations but was CPU intensive because it needed to search for an optimum α at every iteration step. The original flash formulation, on the other hand, required many iterations but was not CPU intensive because few calculations were done at each step. For some systems, the original flash formulation would not converge because it would start to cycle between several compositions. Finally, the algorithm of Modification 3 was expensive because of the required line search plus the various matrix manipulations. It was also not reliable; the optimum α at some iteration k would sometimes push $\ln(K)$ of a specie to a very large number and hence force the specie out of a particular phase. It was decided that the algorithm of Modification 2 would be used in the stability-flash algorithm shown in Figure 4.10.

Table 4.3 Comparison^f of the flash algorithms on some nonideal systems.

temperature, pressure (feed composition) (TPD composition) ^a	traditional flash algorithm (Figure 4.7)	mod. 1	mod. 2	mod. 3	
(1) n-C6 and (2) n-C36 equil. comp. (0.7804, 0.2196) ^b (0.9915, 0.0085) ^b					
623K, 50 Bar (0.85, 0.15) ^b (0.9943, 0.0057) ^b	# iterations	10	6	7	11
	CPU time (s)	0.07	0.80	0.05	1.52
(1) n-C6 and (2) n-C36 → In Critical Region equil. comp. (0.9251, 0.0749) ^b and (0.9618, 0.0382) ^b					
623K, 73 Bar (0.93, 0.07) ^b (0.9675, 0.0325) ^b	# iterations	125	5	8	4
	CPU time (s)	0.87	0.63	0.06	0.51
(1) n-C6 and (2) Polystyrene (25,000 MW) equil. comp. (0.8011, 0.1989) ^c and (0.9841, 0.0159) ^c					
407K, 380 Bar (0.90, 0.10) ^c (0.99999995, 5e ⁻⁸) ^b	# iterations	86	13	50	27
	CPU time (s)	0.98	2.04	0.54	3.82
(1) n-C6 and (2) Polystyrene (25,000 MW) → In Critical Region equil. comp. (0.8952, 0.1048) ^c and (0.9407, 0.0593) ^c					
407K, 485 Bar (0.92, 0.08) ^c (0.99959, 4.1e ⁻⁴) ^b	# iterations	280	35	13	N/A ^d
	CPU time (s)	3.44	4.70	0.20	
(1) n-C6 and (2) Polyethylene-octene (33,000 MW) equil. comp. (0.8848, 0.1152) ^c and (0.9977, 0.0023) ^c					
450K, 42 Bar (0.96, 0.04) ^c (0.999993, 7e ⁻⁶) ^b	# iterations	N/A ^e	N/A ^d	283	N/A ^d
	CPU time (s)			3.50	
(1) methanol and (2) n-C5 equil. comp. (0.3831, 0.6169) ^b and (0.5479, 0.4521) ^b					
288K, 50 Bar (0.45, 0.55) ^b (0.5543, 0.4457) ^b	# iterations	3888	77	11	N/A ^d
	CPU time (s)	25.15	13.0	0.09	
(1) Methanol and (2) n-C5 equil. comp. (0.1025, 0.8975) ^b and (0.7681, 0.2319) ^b					
270K, 50 Bar (0.50, 0.50) ^b (0.0891, 0.9109) ^b	# iterations	311	15	11	N/A ^d
	CPU time (s)	1.95	1.77	0.08	

- a composition given by stability analysis to be unstable to the feed.
- b mole fraction
- c mass fraction
- d did not complete
- e did not converge after 20,000 iterations
- f comparisons were made on a 700 MHz Intel Pentium III computer

The phase stability algorithm used in the method of Figure 4.10 is based on the tangent plane distance (TPD) analysis of Baker, *et al.*^[82] and Michelsen^[79]. Essentially, a tangent to the Gibbs energy curve at the feed is constructed (see the cartoon in Figure 4.11). If the difference

$$TPD \equiv \sum_{i=1}^{ncp} x_i (\mu_i(T, P, \underline{x}) - \mu_i(T, P, \underline{z})) \quad (4.30)$$

is nonnegative for all composition \underline{x} , then the feed is stable (as in the case for \underline{z}_2 in Figure 4.11). The feed is unstable if any \underline{x} can be found that will make (4.30) negative (as in the case for \underline{z}_1 in Figure 4.11); a negative TPD is a necessary and sufficient condition for phase instability.

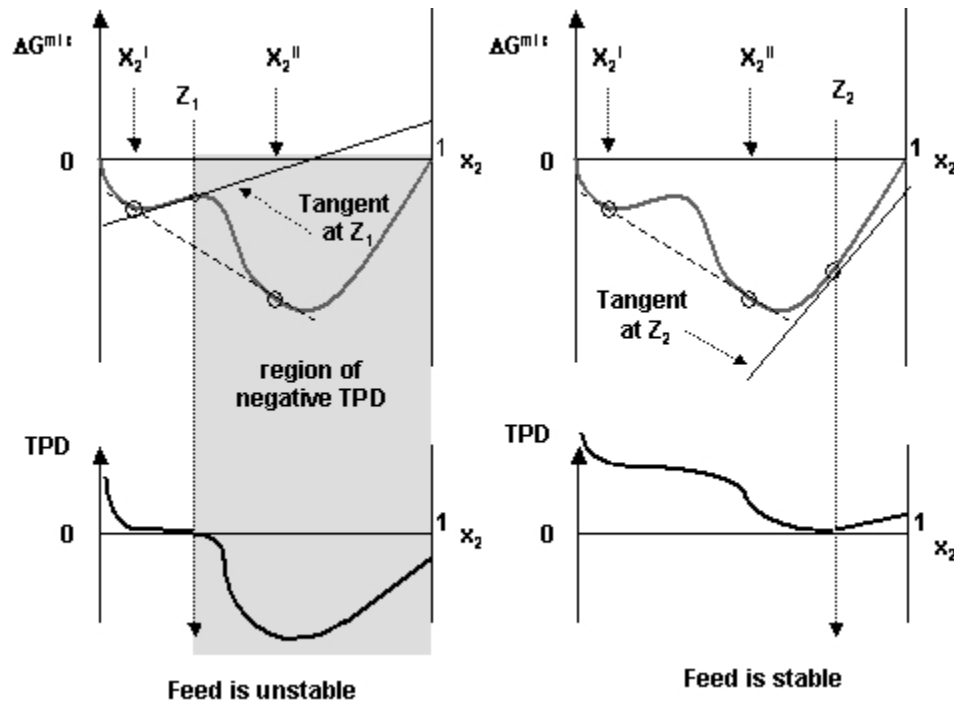


Figure 4.11 Illustration of the tangent plane distance approach to determine phase stability.

In this work, we used the golden section algorithm with the BFGS update to minimize the tangent plane distance. The set of \underline{x} that minimizes the TPD was then used (with the feed composition) to calculate initial estimates of \underline{K} . Note that in our approach, we do not perform an exhaustive search for all the stationary points to (4.30). Instead, we stop the TPD minimization program as soon as a negative TPD is found and rely on the stability check-flash calculation cycle to find the global solution. While our approach is less rigorous, it is faster because we are not interested in finding all the stationary points (the number of which is not known a priori) to the tangent plane distance, just a set of points in composition space that is a good enough initial guess for the flash.

The following mole fraction initial guesses are fed into (4.30):

$$x_i = 0.999999 \quad (4.31)$$

$$x_i = \exp(\ln z_i + \ln \phi_i(z)) \quad (4.32)$$

$$x_i = \frac{P}{P_i^{sat} - P_j^{sat}} \quad \text{for } P_j^{sat} \leq P \leq P_i^{sat} \quad (4.33)$$

Equation 4.31 is effective for systems containing polymers and Eqn. 4.32 was proposed by Michelsen^[79] that seems to work well for a variety of systems. In another check, if the stability algorithm cannot find an unstable point at T, P , the system pressure is reduced until an unstable point emerges and the equilibrium compositions at this lower pressure are used as initial guesses in (4.30). An exhaustive grid search on composition space is performed as a last resort. Because of the nature of the stability algorithm, it is much easier to map out the phase diagram of a mixture by operating inside the unstable regions than searching explicitly for the stable regions.

CHAPTER 5. APPLICATION OF SAFT TO MODEL SYSTEMS

5.1 Introduction

Using the tools developed in the previous chapter, we will apply the SAFT equation of state (EOS) to some model mixtures to test the EOS' range of applicability. We will investigate SAFT's ability to model the thermodynamic phase behavior of long-chain short-chain alkane mixtures in Section 5.2, of polystyrene-hexane and polystyrene-toluene-ethane mixtures in Section 5.3, and of phenanthrene-methane-decane mixtures in Section 5.4. The systems in Section 5.2 and 5.3 will test SAFT's ability to model the effects of size on solubility. The system in Section 5.4 will test SAFT's ability to describe the solubility behavior of polynuclear aromatics, which share structural similarities with asphaltenes. Since asphaltenes differ from other oil components in both size and shape, how well SAFT predicts the phase behavior of these systems provides insights to its ability to relate these molecular features to macroscopic thermodynamic properties. Furthermore, these model systems will provide us with insights regarding asphaltene phase behavior in oil. The system polystyrene-toluene-ethane is particularly interesting because it resembles the model live oil system (asphaltene-toluene-methane) described in Chapter 3. Finally, we are also interested in SAFT's ability to model long-chain short-chain alkane mixtures because the bulk of crude oil is made up of alkanes (see Table 3.1).

Aside from serving as model systems in our investigation of asphaltene phase behavior, these model systems are important in other areas of research. For example, the thermodynamic phase behavior of long-chain short-chain alkane mixtures is important in the recovery of wax products from the Fischer-Tropsch slurry reactor^[83], in determining wax precipitation in natural gas pipelines^[84], and in the design of the ROSE process which uses light, near critical solvents to recover oils from residual^[85]. The thermodynamic phase behavior of polymer-solvent systems is important in polymer synthesis and processing, and the phase behavior of mixtures containing polynuclear aromatics is important in refining, in environmental remediation, and in the recovery of tar oil.

5.2 Long-Chain Short-Chain Alkane Mixtures

5.2.1 Background Information

The goal of this investigation is to determine the extent to which SAFT is applicable to highly asymmetric mixtures of alkanes (and hence how well it accounts for the effects of size on mixture phase behavior). The Peng-Robinson (PR) equation^[50] was also evaluated for comparison. These EOS were tested for their predictive and their correlative abilities, with the experimental vapor-liquid equilibrium (VLE) data of Joyce and Thies^[86] and Joyce *et al.*^[87] for hexane-hexadecane (C₆-C₁₆), hexane-tetracosane (C₆-C₂₄), and hexane-hexatriacontane

(C₆-C₃₆) being used for analysis. The PR equation was chosen because of its widespread use in industry and simplicity.

The Peng-Robinson equation^[50] for pure fluids can be written as

$$P = \frac{RT}{v-b} - \frac{a(T)}{v^2 + 2bv - b^2} \quad (5.1)$$

where P denotes pressure, T temperature, v molar volume, and R the ideal gas constant. The temperature-independent repulsion parameter b is

$$b = \frac{0.07780RT_c}{P_c} \quad (5.2)$$

where T_c and P_c are the critical temperature and pressure, respectively. The temperature dependent attraction parameter $a(T)$ is given by

$$a = a(T_c) \left[1 + \kappa(1 - T_r^{0.5}) \right]^2 \quad (5.3)$$

where

$$a(T_c) = \frac{0.45724R^2T_c^2}{P_c} \quad (5.4)$$

In Eqn. 5.3, κ is correlated to vapor pressure data over a range of reduced temperature T_r . For aromatics, n-alkanes (but only up to n-decane), and other light nonpolar compounds, Peng and Robinson correlated κ to the acentric factor ω :

$$\kappa = 0.37464 + 1.54226\omega - 0.26992\omega^2 \quad (5.5)$$

For other species, κ can be regressed from vapor pressure data.

To extend this EOS to mixtures, van der Waals one-fluid mixing rules are typically applied:

$$a_{mix} = \sum_i \sum_j x_i x_j a_{ij} \quad (5.6)$$

$$b_{mix} = \sum_i x_i b_i \quad (5.7)$$

$$a_{ij} = (a_{ii} a_{jj})^{0.5} (1 - k_{ij}) \quad (5.8)$$

where x_i is the mole fraction of component i in either the vapor or liquid phase and k_{ij} is the binary interaction parameter between components i and j .

Several authors have examined the use of cubic EOS to predict the phase behavior of asymmetric mixtures of n-alkanes. For example, Peters *et al.*^[88] correlated the bubble point pressures for ethane-eicosane and ethane-tetracosane mixtures with the Soave-Redlich-Kwong equation, and for propane-tetracontane mixtures with PR EOS^[89]. More recently, Kontogeorgis *et al.*^[90] investigated the effect of different mixing rules on the ability of the PR equation to predict the bubble point pressures for asymmetric mixtures of alkanes. They found that the binary interaction parameter correlation to the b_{mix} term (commonly defined as l_{ij}) was more important than k_{ij} in providing good fits to the bubble point pressures. Floter *et al.*^[91] compared the effects of using different PR a parameter functions (Eqns. 5.3 to 5.5) for supercritical methane in methane-hexadecane and methane-tetracosane VLE. They found that an a obtained by replacing $[1 + \kappa(1 - T_r^{0.5})]^2$ in Eqn. 5.3 with a correlation optimized to the IUPAC-recommended fugacities for methane gave good VLE predictions.

A few authors have investigated the ability of SAFT to model alkane mixtures with significant degrees of size asymmetry. For example, Pan and Radosz^[92] used a version of SAFT (proposed by Huang and Radosz^[70,93]) with a single, temperature-independent $k_{ij} = 0.03$ to give reasonable predictions of liquid compositions for ethane-eicosane, ethane-docosane, and ethane-tetracosane systems (no experimental vapor-phase compositions were available for these systems). Benzaghou *et al.*^[94] investigated another approach: using the original version of SAFT proposed by Chapman *et al.*^[55], they regressed vapor pressures and liquid densities for n-C₂ to n-C₈ as a group to obtain constant, unique values for the segment diameter and the segment energy; only the segment number was allowed to vary with carbon number. Thus, no k_{ij} was used. Except in the vicinity of the mixture critical points, reasonable predictions of VLE for hexane-hexadecane and hexane-squalane were obtained. In another example, Gregorowicz and de Loos^[95] reported that the version of SAFT with the dispersion contribution proposed by Huang and Radosz^[70,93] gave poor predictions for ethane-eicosane liquid-liquid-vapor equilibria; similarly poor predictions were obtained for the critical end points for the ternary systems ethane-eicosane-methane and ethane-eicosane-propane.

For all EOS used in this study, the k_{ij} 's were obtained by minimizing the total absolute deviation between measured and calculated liquid and vapor compositions summed over all *ndp* data points:

$$\min_{k_{ij}} f = \sum_i^{ndp} \left| \frac{x_{i,calc} - x_{i,exp}}{\min(x_{i,exp}, 1 - x_{i,exp})} \right| + \sum_i^{ndp} \left| \frac{y_{i,calc} - y_{i,exp}}{\min(y_{i,exp}, 1 - y_{i,exp})} \right| \quad (5.9)$$

As indicated in Eqn. 5.9, the calculation was always carried out with the minor component in a given phase. Thus low vapor phase solubilities were weighted approximately the same as other data points. We also omitted the mixture critical points in the determination of the optimal binary interaction parameters.

5.2.2 Results and Discussions

The pure component parameters used in this study are given in Table 5.1. Critical properties and ω for hexane and hexadecane were obtained from Reid *et al.*[96], with κ obtained from Eqn. 5.5. Critical properties for tetracosane and hexatriacontane were obtained from Ambrose and Tsonopoulous[97] and from Nikitin, *et al.*[98], respectively. κ for tetracosane was obtained by regressing the vapor pressure data of Morgan and Kobayashi[99] and API-42[100]. And κ for hexatriacontane was obtained by regressing the vapor pressure correlation of Stephenson and Malanowski[101]. In the case of hexatriacontane, the correlation of Stephenson and Malanowski[101] gives vapor pressures that are in best agreement with the results of an enhancement factor[102] analysis (i.e., to better than $\pm 10\%$). The SAFT parameters for hexane and hexadecane were obtained from Table 4.1. As described in Chapter 4, these parameters were fit to pure component vapor pressures and saturated liquid densities. The SAFT parameters for tetracosane and hexatriacontane were calculated from correlations in Table 4.2.

Table 5.1 Experimentally obtained and regressed pure component parameters for the Peng-Robinson and SAFT equations.

component	PR			SAFT		
	T_c (K)	P_c (bar)	κ	σ (A)	ε/k (K)	m
hexane	507.5	30.1	0.812	3.798	236.77	3.058
hexadecane	722.0	14.1	1.371	3.955	254.70	6.648
tetracosane	800.0	8.7	1.781	3.937	253.18	9.822
hexatriacontane	872.0	4.7	2.224	4.014	256.37	13.860

Each of the tested EOS was fit to three asymmetric mixtures of n-alkanes (C_6 - C_{16} , C_6 - C_{24} , and C_6 - C_{36}) for which both VLE compositions and mixture critical points are available^[86,87]. The temperature of these systems range from 472K to 623K. For each measured pressure-composition isotherm, optimum binary interaction parameters were determined. These optimum binary interaction parameters and the average absolute percent deviation (AAPD) between experimental and calculated phase compositions are listed in Table 5.2. Representative pressure-composition isotherms generated by each EOS are compared with measurements at 622K or 623K in Figures 5.1 and 5.2.

Table 5.2 Optimum binary interaction parameters for the tested EOS and deviations (AAPD^a) between experimental^[86,87] and calculated phase compositions

mixture	T (K)	PR		SAFT			
		opt. k_{ij}	AAPDx	AAPDy	opt. k_{ij}	AAPDx	AAPDy
C ₆ -C ₁₆	473	-0.01	8.3	2.8	0.005	3.8	4.0
	524	0.00	7.7	2.0	0.031	14.5	6.1
	573	0.00	5.2	4.9	0.006	4.9	13.2
	623	0.02	5.0	8.4	0.007	3.7	8.8
C ₆ -C ₂₄	473	-0.01	11.1	14.4	0.021	16.4	8.17
	524	-0.04	11.0	7.5	0.015	16.2	14.3
	573	-0.11	22.1	5.1	-0.009	4.8	16.5
	623	-0.20	33.0	2.2	-0.011	3.8	10.3
C ₆ -C ₃₆	522	-0.14	39.6	20.4	0.008	9.1	45.0
	573	-0.24	42.7	25.6	0.006	6.4	19.7
	622	0.12	31.9	56.8	-0.002	6.2	14.5

$${}^a AAPD = \frac{\sum_{i=1}^{ndp} |x_i^{\text{exp}} - x_i^{\text{calc}}|}{ndp \cdot (\min(x_i^{\text{exp}}, 1 - x_i^{\text{exp}}))} \times 100, \text{ x is either the liquid or vapor composition}$$

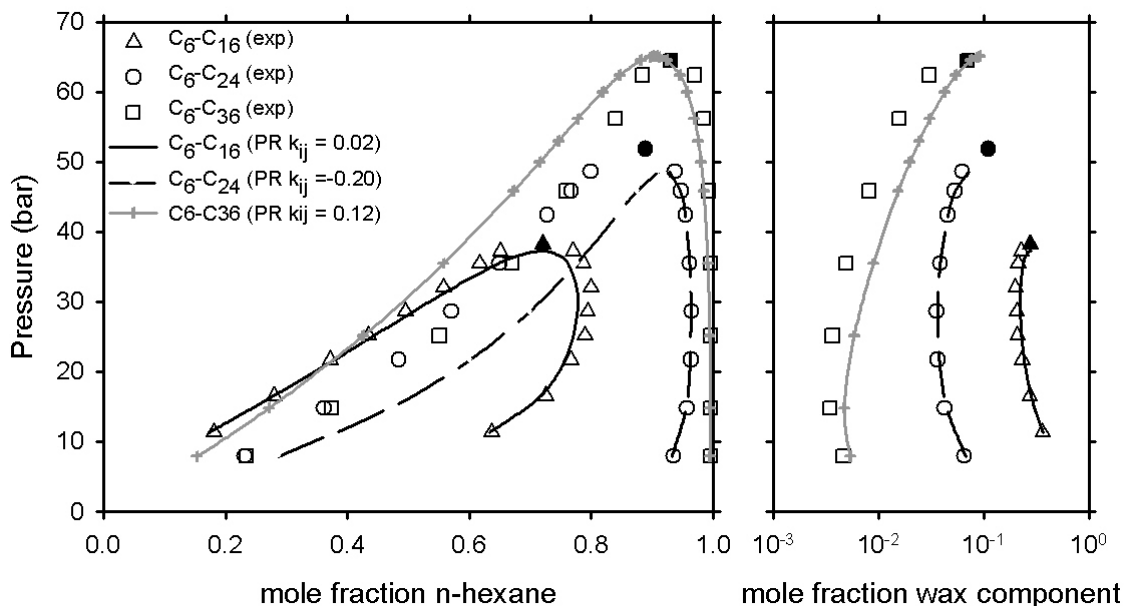


Figure 5.1 PR fits to mixture data at $T=622K$ or $623K$. The vapor compositions are expanded on the right and the mixture critical points are filled. Experimental data are from Joyce and Thies^[86] and Joyce, *et al.*^[87].

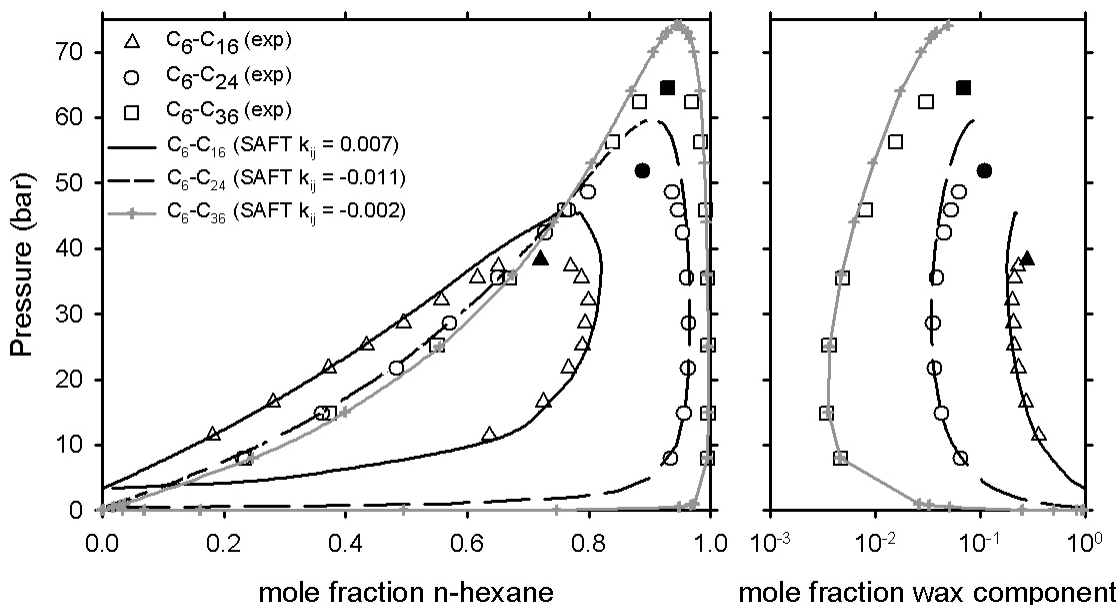


Figure 5.2 SAFT fits to mixture data at $T=622K$ or $623K$. The vapor compositions are expanded on the right and the mixture critical points are filled. Experimental data are from Joyce and Thies^[86] and Joyce, *et al.*^[87].

With the Peng-Robinson equations, a good fit to experimental data can be obtained for the C₆-C₁₆ system at all investigated temperatures (Table 5.2, Figure 5.1). Furthermore, for this system, the k_{ij} can be set to 0 with little loss in accuracy. However, as the chain length of the wax component increases, the goodness of fit deteriorates significantly. Moreover, for the C₆-C₂₄ and C₆-C₃₆ binaries the optimum k_{ij} 's exhibit large changes in magnitude as a function of temperature. Part of the reason for the poor fits to liquid phase compositions is that PR does not correctly predict the liquid density behavior of pure long-chain n-alkanes. As seen in Figure 4.5, PR EOS predicts molar volumes of long-chain n-alkanes that are significantly larger than the measured values. Techniques such as volume translation would correct this discrepancy in molar volumes but would not improve the phase equilibrium results.

Comparison of SAFT calculated phase equilibrium compositions and experimental results are given in Table 5.2 and Figure 5.2. At low to moderate pressures (i.e. far away from the critical region), SAFT provides a good fit to both the liquid and vapor phase compositions; the higher temperature fits are especially good. Furthermore, the optimized k_{ij} 's are very close to 0. One problem with SAFT is that the mixture critical pressures are significantly over-predicted; this deficiency is responsible for most of the reported deviations from the experimental data. For example, if the highest-pressure VLE compositions

shown in Figure 5.2 are not used in the AAPD calculations, the AAPDs for SAFT decreased by up to 37% on the liquid side and by up to 41% on the vapor side.

For an equation of state to be predictive, binary interaction parameters must be essentially constant or well-behaved as a function of temperature. As seen in Table 5.3, the liquid phase predictions of SAFT with $k_{ij} = 0$ are in good agreement with experimental data, and are in fact better than the calculated liquid phase composition shown in Table 5.2. The variation in k_{ij} 's listed in Table 5.2 is the result of SAFT's attempt to improve fits to the vapor compositions (often at a detriment to its liquid composition fits).

Table 5.3 AAPDs between experimental and predicted phase compositions for SAFT ($k_{ij} = 0$).

mixture	T (K)	SAFT ($k_{ij} = 0.00$)	
		AAPD _x	AAPD _y
C ₆ -C ₁₆	472	1.9	9.2
	524	4.6	26.2
	573	4.0	15.8
	623	3.5	10.7
C ₆ -C ₂₄	473	8.2	32.9
	524	6.0	25.3
	573	9.6	12.4
	623	8.9	7.8
C ₆ -C ₃₆	522	5.7	49.6
	573	5.2	21.6
	622	6.4	14.2

5.2.3 Section Summary

In spite of its deficiencies in vapor phase predictions and modeling of the critical region, SAFT is a better equation of state for predicting the phase behavior of highly asymmetric mixtures of alkanes compared to the conventional cubic equations. Because SAFT parameters correlate with molecular weight, we can avoid uncertainties in the critical points for long-chain alkanes that figure in the cubic equations of state calculations. Using a k_{ij} of 0, SAFT will provide good estimates of liquid phase compositions up to within 5 to 10 bars of the predicted mixture critical point. This means that we should be able to obtain good predictions of crude oil thermodynamic properties using SAFT if we set the k_{ij} 's between all alkanes in oil (with the exception of the light gases) to 0.

5.3 Polystyrene-Solvent/Precipitant Mixtures

5.3.1 Background Information

The goal of this section is to investigate the effects of asphaltene size on solubility via the behavior of various molecular weight polystyrenes in hexane and in mixtures of toluene and ethane. Polystyrene is chosen as an “asphaltene” model compound because it shares structural similarities (i.e., very large and possessing a certain degree of aromaticity) with asphaltenes and interacts mainly through dispersion forces.

Unlike mixtures of long-chain alkanes with solvents, mixtures containing polymers are less well defined (the polymers will exhibit at least some polydispersity) and the polymers do not have quantifiable vapor compositions.

The phase behavior of polymer solutions are often given in terms of the mixtures' cloud point pressures. This is the pressure at which a polymer in a mixture at fixed temperature, composition, and polymer molecular weight distribution first becomes unstable and is equivalent to the onset instability pressure for asphaltenes in oil described in Chapter 3.

The SAFT equation of state used to calculate polystyrene properties is slightly different than that used in the other calculations presented in this work. More specifically, the dispersion contribution developed by Chen and Kreglewski^[103] (as proposed by Huang and Radosz^[70,93]) is used in the polystyrene investigations. Recall that the SAFT EOS described in Chapter 4 (which is used in the rest of this work) has its dispersion contribution from Gross and Sadowski^[62]. While the pure component parameters and the mixture binary interaction parameters vary depending on the dispersion contribution used, the two different forms of SAFT will reproduce and show the same phase behaviors.

5.3.2 Results and Discussions

Using the pure component parameters listed in Table 5.4, we generated the cloud point pressures for a 4% mass polystyrene in n-hexane solution. The polystyrene used in the experiment is nearly monodisperse. As shown in Figure 5.3, SAFT predicts accurately the phase behavior of the polystyrene-hexane binary mixture over a wide range of pressures and temperatures from a low molecular weight of 8,000 to a high polystyrene molecular weight of 50,000.

These calculations were made using a single binary interaction parameter of 0.017. As the molecular weight of the polymer increases, so does the size of the two phase region. And at a given temperature, pressure increases will eventually move the system from a two-phase region into a one phase region due to the increase in the solvent's cohesive energy density with increasing pressure.

Table 5.4 SAFT parameters used to model polystyrene phase behavior. These parameters were obtained using the dispersion contribution developed by Chen and Kreglewski. [103]

Compound	σ (A)	ϵ/k (K)	m
ethane	3.2382	191.44	1.941
hexane	3.0827	202.72	4.724
polystyrene	3.0430	226.5	MW/21.9696
toluene	3.0251	245.27	4.373

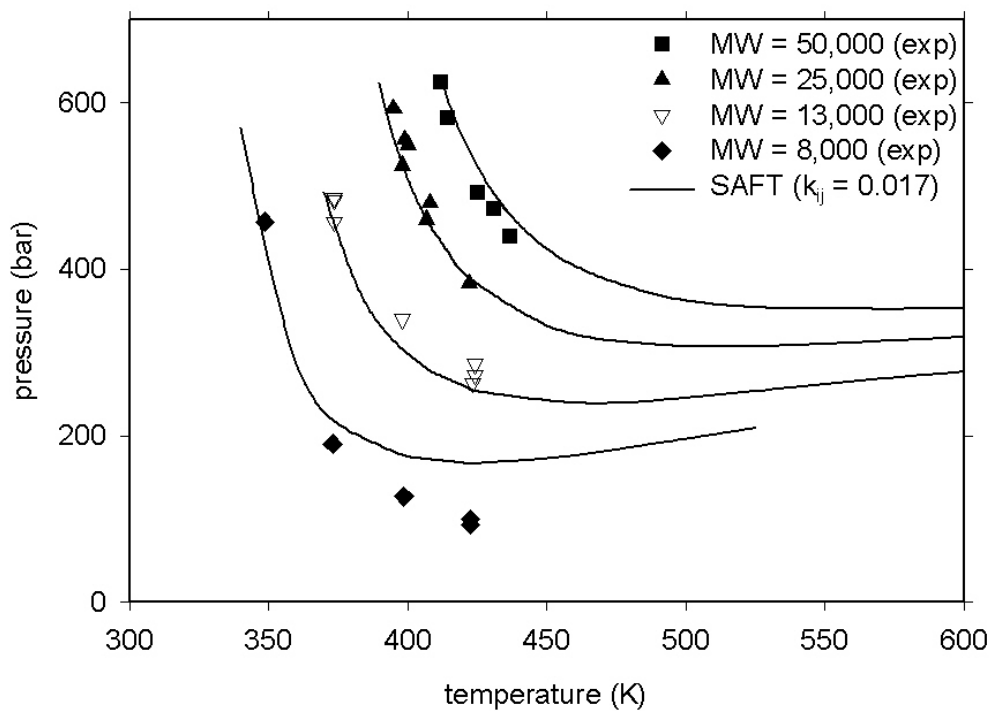


Figure 5.3 Cloud point pressures for 4% polystyrene solution in n-hexane. Experimental data are from Xiong and Kiran^[104].

We compared experimental cloud point pressures with SAFT predictions for 1%, 4%, and 8% mass polystyrene (8,000 MW) in hexane in Figure 5.4. As seen in the figure, SAFT qualitatively predicts the effects of different polymer concentrations on cloud point pressures. A large shift in the cloud point curves from 1% to 4% mass polystyrene is observed while a considerably smaller shift in the cloud point curve is observed between 4% and 8% mass polystyrene. A constant k_{ij} of 0.017 was used in all calculations.

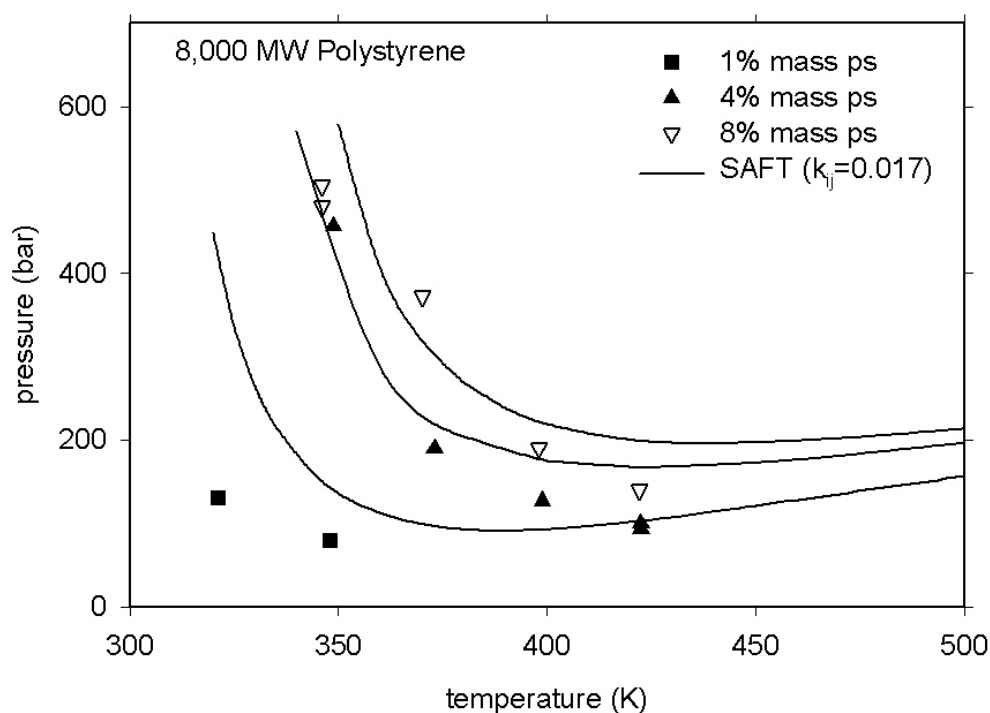


Figure 5.4 Cloud point pressures for 8,000 MW polystyrene solution in n-hexane. Experimental data are from Xiong and Kiran^[104].

An interesting observation from Figure 5.3 and 5.4 is that SAFT predicts the presence of a lower critical solution temperature (LCST) region at the higher

temperatures. In this region, an increase in temperature (at a fixed pressure) will result in the demixing of the polystyrene solution; the more typically observed behavior of increasing solubility with increasing temperature occurs in the upper critical solution temperature, or UCST region. While polystyrene-pentane and polystyrene-butane systems are known to exhibit LCST behaviors at higher temperatures, the presence of the LCST region has only been conjectured for the polystyrene-hexane system due to insufficient data.^[104]

The existence of the UCST and LCST regions can be explained in terms of contributions to the Gibbs energy. At lower temperatures, entropy effects dominate and polystyrene solubility increases with increasing temperature. At the higher temperatures (i.e., as the critical temperature of the solvent is approached), enthalpy effects dominate due to increasing differences in the rate of free volume expansion of the components, which effects large changes in the cohesive energy density of the solvent. In the case of the polystyrene-hexane system investigated here, the critical temperature of hexane is about 507.5K.^[96]

Although the polystyrene-hexane mixture is only a model system for asphaltenes, it elucidates characteristics typical of asphaltenes in crude oil. For instance, operations that decrease pressure (at fixed temperature and composition, as in the case when the mixture is above its bubble point) may lead to asphaltene phase separation due to increasing differences in the species' free volumes. And the opposing solubility behavior of asphaltenes with changes in

temperature, similar to the polystyrene mixing/demixing behaviors with temperature change in the UCST and LCST regions, has been reported in literature. From the free energy description given above, we can expect the onset of LCST behavior to shift to lower temperatures with increasing concentration of light gases in the asphaltene-containing solution (this behavior is observed in Figure 5.4 and in Figure 5.7 for the mixture polystyrene-toluene-ethane, which will be discussed in the next section). Indeed, it has been discussed in literature^[23] that with propane ($T_c \sim 100^\circ\text{C}$) addition, asphaltenes become increasingly unstable with temperature increase. On the other hand, for n-alkane (n-C₅₊) titrations, asphaltenes become more stable with increasing temperature.^[23] Of course, whether or not LCST behavior will be observed depends on the temperature range investigated.

A comparison of experimental and SAFT calculated phase equilibrium compositions (and tie lines) for a mixture of polystyrene, toluene, and ethane at 343K shows that SAFT can accurately account for the effects of pressure and composition changes (Figure 5.5). The polystyrene used in this experiment has a number average MW of 68,000 and $MW_w/MW_n = 2.21$. A single binary interaction parameter for ethane-polystyrene listed in Figure 5.5 was fit to equilibrium composition data at 62 bar. This system is similar to the model live oil described in Chapter 3 in that we have polystyrene (the model asphaltene) dissolved in a mixture of solvent (toluene) and precipitant (ethane). Like asphaltenes, varying the amounts of toluene (solvent) and ethane (precipitant)

changes the stability of polystyrene (at a fixed polymer concentration) in the system. Addition of toluene makes the system miscible, while ethane addition eventually results in phase separation (Fig. 5.5).

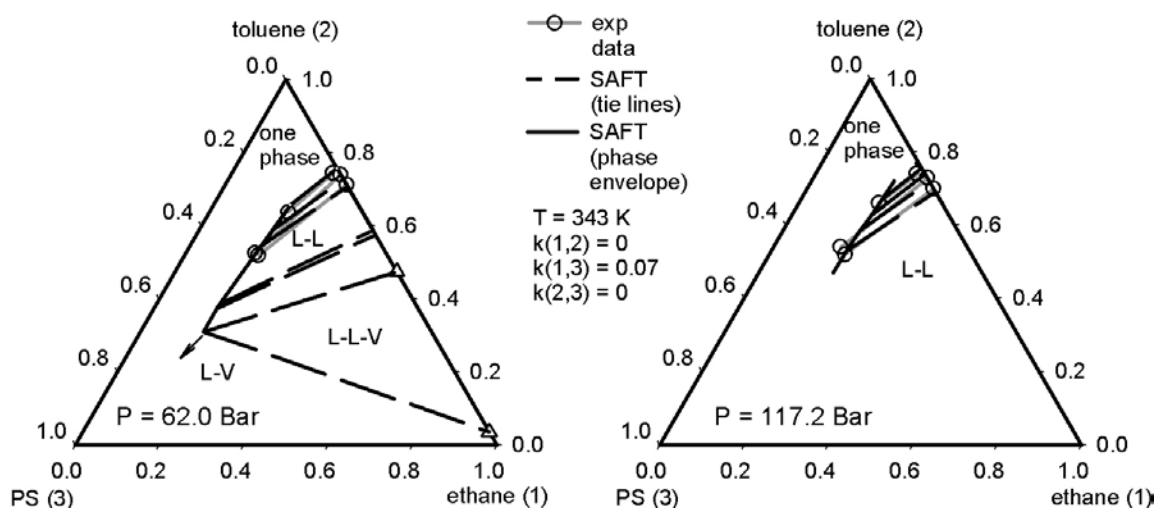


Figure 5.5 Ethane-toluene-polystyrene phase diagram at 343K and 62 or 117.2 bar. The compositions are in mass fractions and the regions of liquid-liquid (L-L), liquid-liquid-vapor (L-L-V), and liquid-vapor (L-V) equilibria are demarcated. Experimental data are from Seckner, *et al.*[105].

SAFT-predicted pressure effects on the phase stability of the ethane, toluene, and polystyrene system at 500K is plotted in Figure 5.6. When the pressure is increased from 300 to 500 bars, we see an increase of the single phase region. This is expected because increasing pressure increases the density and thus the cohesive energy density of the solvent. It is interesting to note in Figures 5.5 and 5.6 that at a given pressure, the stability boundary is approximately a function of ethane mass fraction and is nearly independent of the amount of polystyrene. This is analogous to saying that asphaltene stability is dominated by the solution gas-oil-ratio rather than the amount of asphaltenes

in the solution. It is also interesting to note that a plait point is observed at each of the pressures; when ethane is added to the system to induce precipitation, the precipitated phase can be either polymer lean or polymer rich depending on the polymer concentration with respect to the plait point. Both the formation of a light phase (asphaltene-lean) and the formation of a heavy phase (asphaltene-rich) have been observed at asphaltene instability onset in the field.^[106]

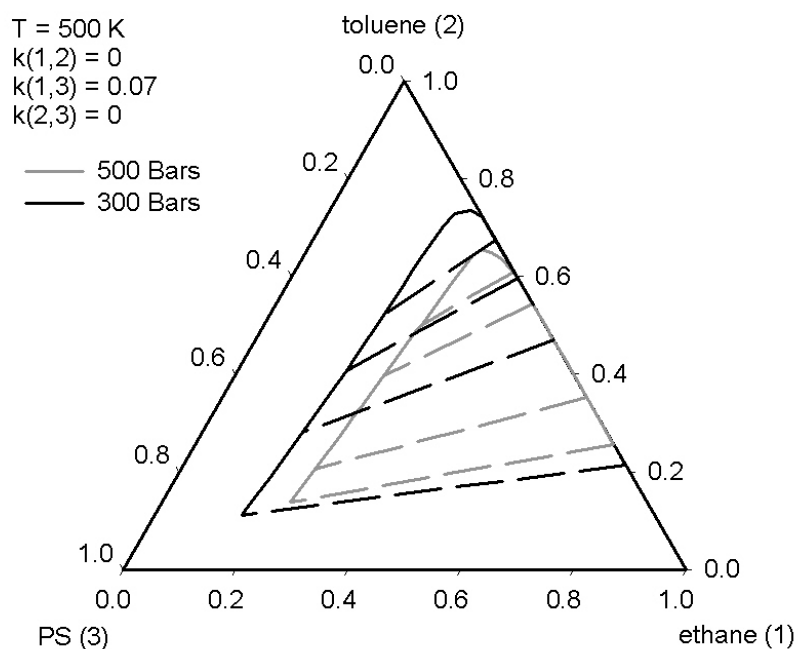


Figure 5.6 SAFT-predicted polystyrene-toluene-ethane phase diagram at 500K and 300 or 500 bars.

In Figure 5.7, we compared SAFT-predicted pressure-temperature diagrams for a system containing 17.8% mass ethane (in toluene and 68,000 number average MW polystyrene) and a system containing 22.5% mass ethane with experimental data of Seckner, *et al.*^[105]. The binary interaction parameters for the polystyrene-toluene-ethane system fitted to equilibrium composition data

at 343K and 62 bar were used in these calculations. To obtain these data, Seckner, *et al.* slowly added ethane to a mixture with initially 5% mass polystyrene dissolved in toluene until the onset of phase instability. This is similar to the methane titration of a 1g asphaltene/100mL toluene mixture until asphaltene instability onset in our experimental studies.

As seen in Figure 5.7, SAFT qualitatively describes the liquid-liquid and liquid-vapor equilibrium phase behavior of the polystyrene-toluene-ethane mixture with 17.8% mass ethane. The predicted phase envelopes are consistently lower than the experimental values. For the polystyrene-toluene-ethane mixture with 22.5% mass ethane, SAFT predictions for the liquid-liquid instability onset do not agree well with experimental data; SAFT shows the “breaking off” of the LCST/UCST curve from the LV curve at a much higher temperature than measured. According to Seckner, *et al.*^[105], the location of the LCST curve becomes very sensitive to ethane concentration at levels of 20% mass or greater. For example, the behavior predicted by SAFT is seen experimentally for the system with 24.9% mass ethane^[105]. The poor prediction given by SAFT is partly due to uncertainties in concentration measurements, to the effects of polymer polydispersity, and to the fact that the binary interaction parameters were not optimized.

We expect the “peculiar” temperature dependence of asphaltenes (i.e. the behavior in the LCST region) to be most apparent in systems with a large

concentration of light gas components and in reservoirs with higher temperatures.

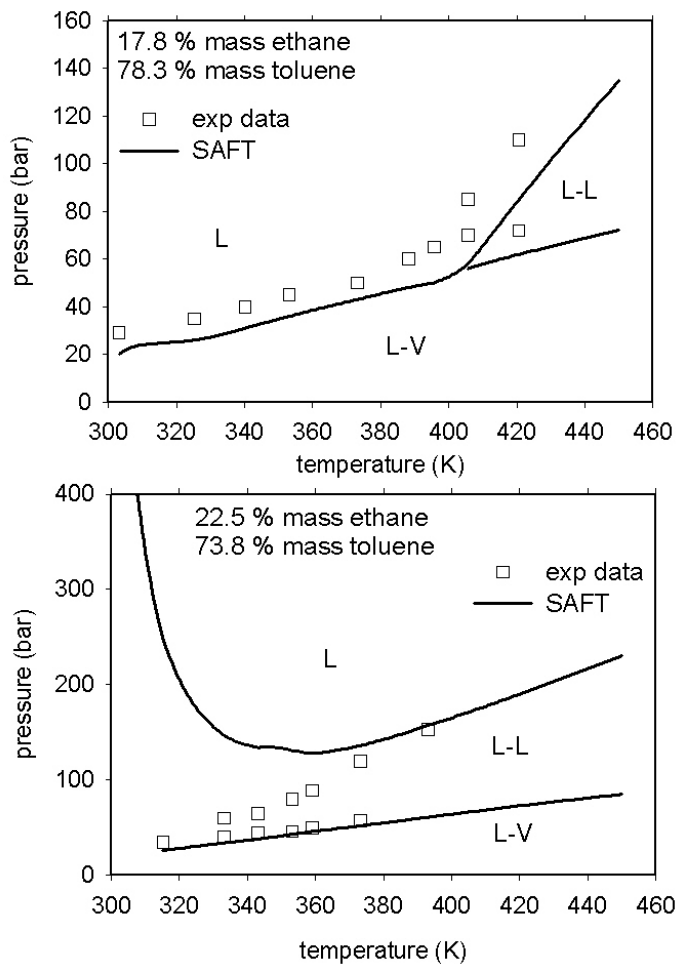


Figure 5.7 Experiment and SAFT-predicted pressure-temperature diagrams for the system polystyrene, toluene, and ethane. L=one liquid phase, L-L=two liquid phases in coexistence, L-V=liquid and vapor phases in coexistence. Experimental data are from Seckner, *et al.*^[105].

5.3.3 Section Summary

In this section, we showed that SAFT is capable of describing and predicting the phase behavior of binary and ternary systems consisting of species with very large size disparities. Various molecular weight polystyrenes

were used as model asphaltenes and their behaviors in solvents and precipitants investigated. The effects of pressure, temperature, and composition changes on phase stability can be accurately described using SAFT. Furthermore, because of similarities in phase behavior between asphaltenes and polystyrene, we were able to describe many asphaltene behaviors in crude oil in the framework of polymer thermodynamics.

5.4 Phenanthrene-Solvent/Precipitant Mixtures

5.4.1 Background Information

The phase behavior of the system phenanthrene-methane-decane at solid-liquid-vapor equilibrium (SLVE) was modeled to investigate whether SAFT can describe the solubility behavior of polynuclear aromatics. In this investigation, SAFT was used to describe fluid behavior in the liquid phase only; the solid phase was described using Eqn. 5.10. Phenanthrene, a three-ring polynuclear aromatic, was the model asphaltene in this work. Recall from Chapter 2 that the polynuclear aromatic cores of asphaltene molecules are structurally similar to a phenanthrene molecule. The conjugated benzene rings in the polynuclear aromatics (PNAs) make PNAs much more polarizable than linear or branched molecules of similar molecular weights (due to the delocalization of the π electrons).

When a (pure) solid phase is in equilibrium with a liquid phase, the fugacity of the solid ($f_{i,solid}$) is related to that specie's subcooled (pure) liquid fugacity ($f_{i,liq}$) by the ratio^[107,108]

$$\ln \frac{f_{i,liq}}{f_{i,solid}} = \frac{\Delta h^f}{RT_t} \left(\frac{T}{T_t} - 1 \right) - \frac{\Delta c_p}{R} \left(\frac{T}{T_t} - 1 \right) + \frac{\Delta c_p}{R} \ln \frac{T_t}{T} + \frac{\Delta v}{RT} (P - P^{sat}) + \lambda \quad (5.10)$$

In Eqn. 5.10, Δh^f is the enthalpy of fusion, Δc_p is the change in heat capacity from the liquid to the solid phase, Δv is the change in volume from the liquid to the solid phase, and λ is the change in Gibbs energy due to solid-solid phase transition divided by RT . The solid properties Δh^f , c_p^{solid} , v^{solid} , and λ are determined from experiments. The triple point temperature T_t can be approximated with the melting point temperature. Furthermore, the two terms containing the heat capacities are approximately equal in magnitude and opposite in sign in this investigation and can be dropped from Eqn. 5.10. For example, the magnitudes of the two terms containing the heat capacities differ by at most about 3% in the temperature range investigated. In this investigation, the fugacity of the subcooled liquid phenanthrene, the molar volume of the subcooled liquid phenanthrene, and the saturation pressure of the subcooled liquid phenanthrene were calculated using SAFT; the value for Δh^f and λ and the molar volume of solid phenanthrene were obtained from experiment. The condition of equi-fugacity between the solid and liquid phases was enforced at a given T and P to obtain the equilibrium compositions.

5.4.2 Results and Discussions

The solid and phase transition properties of phenanthrene are listed in Table 5.5 and the SAFT pure component parameters are listed in Table 4.1. Note that a solid-solid phase transition exists for phenanthrene at 347.5K. [109]

Table 5.5 Select solid, solid-solid and solid-liquid phase transition properties of pure phenanthrene.[109]

v_{solid}	151.7 cm ³ /mol
T_m	372.4 K
Δh_f	16,463 J/mol
λ transition energy	217 J/mol

The calculated and experimental SLVE compositions at pressures between 20.2 and 60.8 bar and temperatures between 350 K and 362K are plotted in Figure 5.8. The binary interaction parameters between phenanthrene-methane ($k_{ij} = 0.094$) and methane-decane ($k_{ij} = 0.015$) were fit to two-component vapor-liquid equilibrium data^[110-112] while the k_{ij} between phenanthrene and decane ($k_{ij} = 0.012$) was fit to the SLV equilibrium compositions at 350K. Comparison of the calculations with experimental data shows good agreement. As expected, the size of the SLVE region decreases as the temperature of the system approaches the melting temperature of phenanthrene. At a given temperature, increasing the system's pressure will decrease the size of the SLVE region but will increase the size of the SLE region.

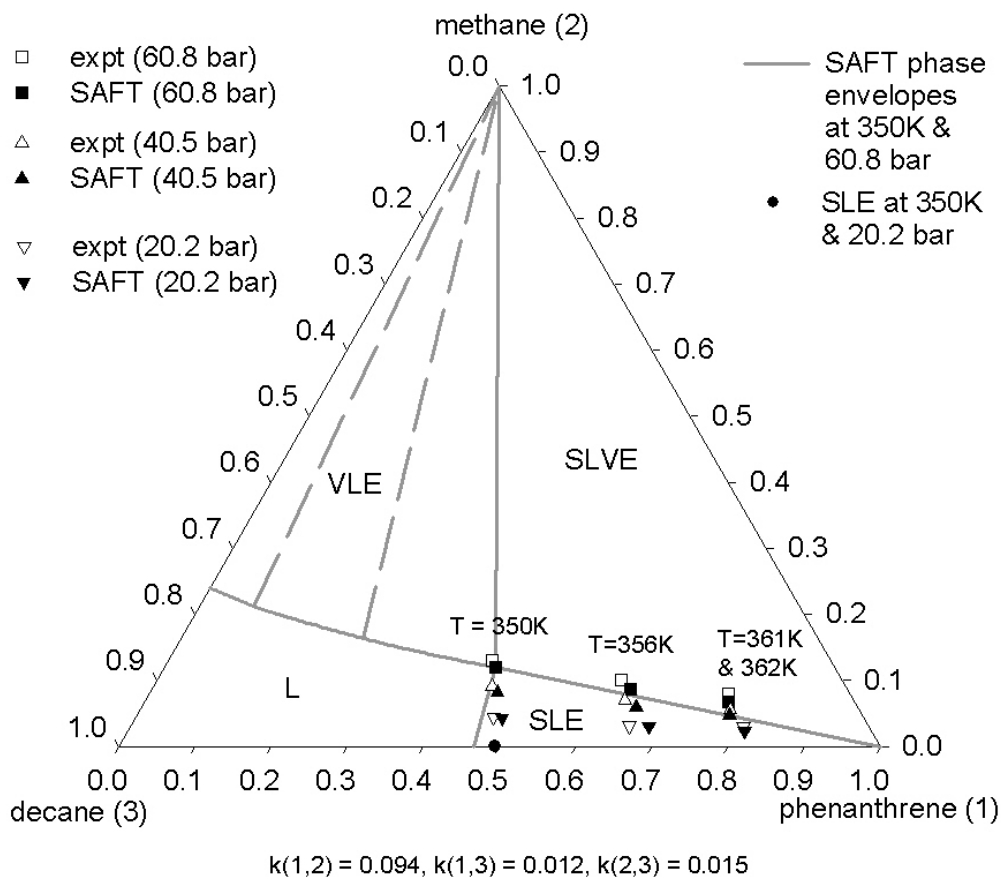


Figure 5.8 Experiment and SAFT+solid fugacity model calculated SLVE for the system phenanthrene-decane-methane at various pressures and temperatures. The calculated regions of VLE and SLE are demarcated. Experimental data are from Jacoby^[113].

An interesting observation from Figure 5.8 is that at a given temperature, an increase in pressure actually decreases the solubility of phenanthrene in the binary mixture with decane. For instance, at 60.8 bars, phenanthrene is soluble in decane up to about 47% (mole) and at 20.2 bars, phenanthrene is soluble in decane up to about 50% (mole). We observed similar pressure-solubility behavior with a system of phenanthrene and toluene at 293K using the experimental setup described in Chapter 3 (see Table 5.6). This behavior occurs because solid phenanthrene has a smaller molar volume than phenanthrene in

solution. When the system is pressurized, more liquid phenanthrene would go into the solid phase to minimize system volume. As seen in Table 5.6, although our model qualitatively describes the same pressure-solubility behavior, the predicted solubility is less sensitive to pressure than what was observed in experiments. We do not expect this type of pressure-solubility behavior to occur for asphaltenes because their polydispersity and the side groups surrounding their polynuclear aromatic cores prevent crystallization.

Table 5.6 Pressure-solubility behavior of phenanthrene in toluene at 293K.

solubility pressure (psi) ^a	exp. mole frac. Phenanthrene	SAFT mole frac. phenanthrene ($k_{ij}=0.008$)
~4200	0.147	0.152
~4500	0.145	0.151
~5100	0.143	0.151

a phenanthrene is soluble below the solubility pressure.

5.4.3 Section Summary

In this section, we showed that SAFT (together with a solid fugacity model) is able to describe the solubility behavior of polynuclear aromatics through an investigation of the SLVE phase behavior of phenanthrene in decane and methane. The size of the SLVE region decreases with increasing temperature and pressure, and the size of the one-phase (liquid) region increases with increasing pressure. Furthermore, the model is able to predict the pressure-solubility behavior of phenanthrene in which increasing pressure leads to lower solubility.

CHAPTER 6. MODELING OF ASPHALTENE PHASE BEHAVIOR

6.1 Introduction

The SAFT equation of state will be used to model asphaltene phase behavior in a model live oil and a recombined oil under reservoir conditions, with the asphaltenes modeled as a monodisperse species. Recall from Chapter 3 that the model live oil is a mixture of n-heptane insoluble asphaltenes in toluene and methane, and that the recombined oil is a mixture of stock-tank oil with its separator gas. We will compare the theory results with asphaltene precipitation data from n-alkane titrations at ambient conditions and from reservoir depressurization described in Chapter 3.

Two issues that will be addressed in this chapter are: (1) how to model asphaltenes in SAFT and (2) how to model the other oil components in SAFT. The equation of state parameters for asphaltenes are fit to ambient condition precipitation data from oil titrations with n-alkanes. If the mechanism responsible for asphaltene precipitation under reservoir depressurization is consistent with the mechanism in titration experiments, thermodynamic models that correctly account for the interaction forces should be able to predict the depressurization results based on matching the results of the titration experiments. To model reservoir fluids in SAFT, a lumping scheme that divides the recombined oil into six pseudo-components based on composition (from gas chromatography),

saturates-aromatics-resins-asphaltenes (SARA) fractionation, and gas-oil-ratio (GOR) is introduced.

As discussed in Chapter 2, the underlying hypothesis of our approach is that molecular size and nonpolar van der Waals interactions dominate asphaltene phase behavior in crude oil. This view is supported by: (1) the large effects on intermolecular interactions due to the polynuclear aromatic cores; (2) by the solubility parameter mapping arguments^[8]; (3) by the contrasting solvating and precipitating abilities of non-polar materials of similar sizes and structures (i.e. toluene vs. n-heptane and CS₂ vs. CO₂); and (4) by the success of using refractive index to estimate the stability of asphaltenes in oil-precipitant mixtures (see Chapter 3). Within this molecular thermodynamic framework, SAFT is a good candidate for asphaltene phase behavior modeling because it accurately describes and predicts the phase behavior of nonpolar fluids where molecular size and shape interactions dominate (see Chapter 5).

6.2 Model Oil Investigations

6.2.1 Determination of Asphaltene SAFT Parameters

Since the model oil is a mixture of well defined species with n-C₇ insoluble asphaltenes, all SAFT parameters except those for the asphaltenes can be found in Table 4.1. We will fit the SAFT parameters for asphaltenes to the measured composition and mixture refractive index data at the onset of asphaltene instability with n-alkane titration (Table 3.2). The procedure is outlined in Figure

6.1. Essentially, a set of SAFT asphaltene parameters is chosen such that (1) the calculated solubility parameter (δ) is in the range reported for asphaltenes, (2) the SAFT asphaltene parameters are within the correlation space bound by the n-alkanes and PNA correlations (see Fig. 4.6), and (3) the asphaltenes are soluble in toluene. The parameters that meet the above criteria are then used to calculate the mixture composition and refractive index (P_{RI}) at the onset of asphaltene instability for a range of n-alkane precipitants at ambient conditions. If the calculated compositions and P_{RI} 's do not agree with experimental measurements, another set of asphaltene SAFT parameters that satisfies the aforementioned constraints (refer to Chapter 7 for the selection guidelines) is used and the procedure repeated until satisfactory agreement (determined, for instance, with average absolute percent deviations between measured and calculated compositions or P_{RI} s) is obtained.

The refractive index of the asphaltene-toluene-precipitant mixture at the onset of asphaltene instability can be calculated from instability onset compositions using Eqn. 3.1. As described in Chapter 3.4, we use an asphaltene molar refraction of $1317 \text{ cm}^3/\text{mol}$ in our calculations but the contribution of asphaltenes is extremely small due to their low concentrations. The molar refraction of other species (toluene and n-alkanes) are calculated from group contribution methods given in the CRC Handbook of Chemistry and Physics.^[44] For these compounds, the molar refractions calculated using the group

contribution method are in good agreement with those calculated from measured pure species' refractive indices and densities (see Table 3.6).

To satisfy the mass density requirement of pure asphaltenes (i.e. asphaltenes having densities between 1.13 g/cm^3 and 1.20 g/cm^3), the molecular weight of the asphaltene needs to be recalculated every time the set of SAFT asphaltene parameters is changed. This is important because SAFT requires molar compositions as inputs. Since the asphaltene/toluene ratio in the model oil is 1g asphaltenes per 100mL toluene at 293 K and 1 bar, failure to update the asphaltene molecular weight whenever the SAFT asphaltene parameters are changed effectively will change the ratio of asphaltenes to toluene between the iterations.

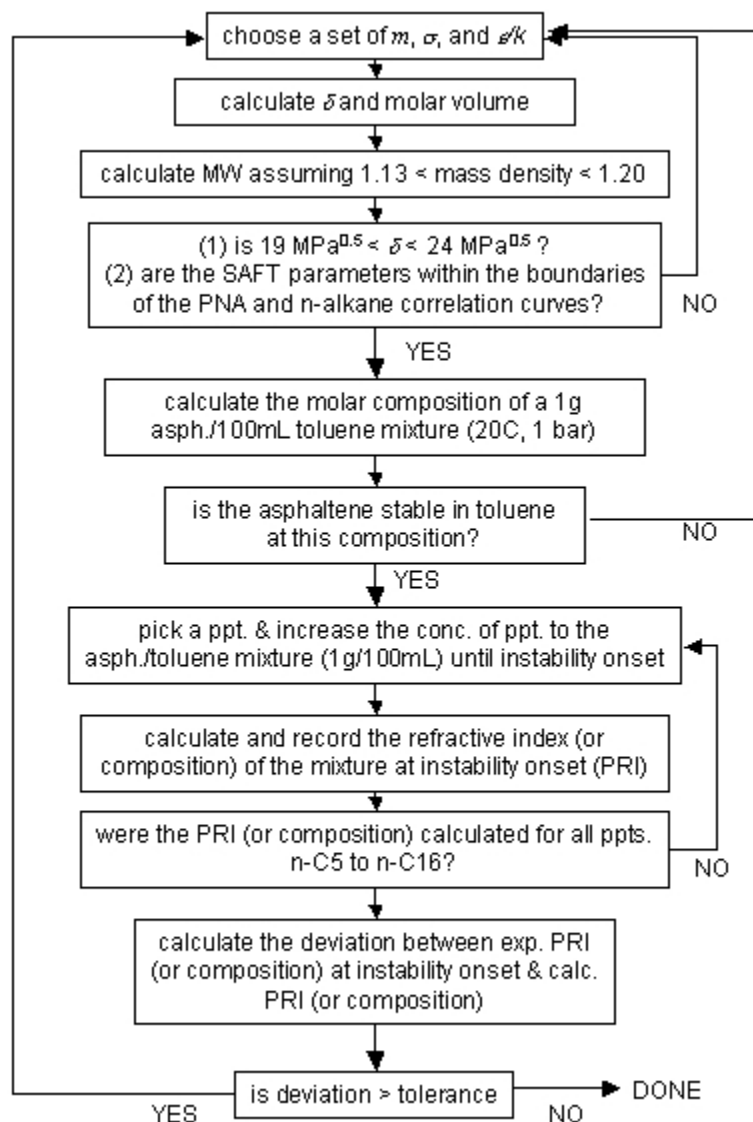


Figure 6.1 Asphaltene SAFT parameters fitting procedure.

To reduce the number of fitted parameters, all binary interaction parameters between asphaltenes and other species are set to zero. The k_{ij} 's between toluene and n-alkanes (from pentane to hexadecane) are also set to 0 because SAFT adequately describes the VLE behavior of these systems with zero k_{ij} .

Using the procedure outlined above, the resulting fits for the n-C₇ insoluble asphaltenes to composition (in terms of precipitant volume fraction, or ϕ_v^{ppt}) and to the refractive index of the mixture at the onset of asphaltene precipitation (P_{RI}) are shown in Figure 6.2. The fitted asphaltene has the following SAFT parameters: $\sigma = 4.05$ Angstrom, $m = 80.0$, and $\varepsilon/k = 350.8$ K (also listed in Table 6.6). This asphaltene has a SAFT calculated solubility parameter of 21.85 MPa^{0.5} and a molar volume of 3,334 cm³/mole. Given that the density of asphaltenes is estimated to be between 1.13 g/cm³ and 1.20 g/cm³ at room conditions, the SAFT calculated model oil asphaltene would then have an implied molecular weight between 3767 and 4000. It can be seen from Figure 6.2 that SAFT fits the experimental data well. Furthermore, the equation of state predicts a precipitant volume fraction maximum around nonane and decane. This maximum in ϕ_v^{ppt} has been known to exist from experimental studies.[5,114,115]

A sensitivity analysis on the effects of changing each of the asphaltene parameters (m , σ , and ε/k) on the calculated mixture composition at asphaltene instability onset is presented in Chapter 7. The analysis will provide some insights into the behavior of the equation of state parameters. It will also give some guidelines on how to select the “appropriate” set of SAFT asphaltene parameters to reproduce experimental data.

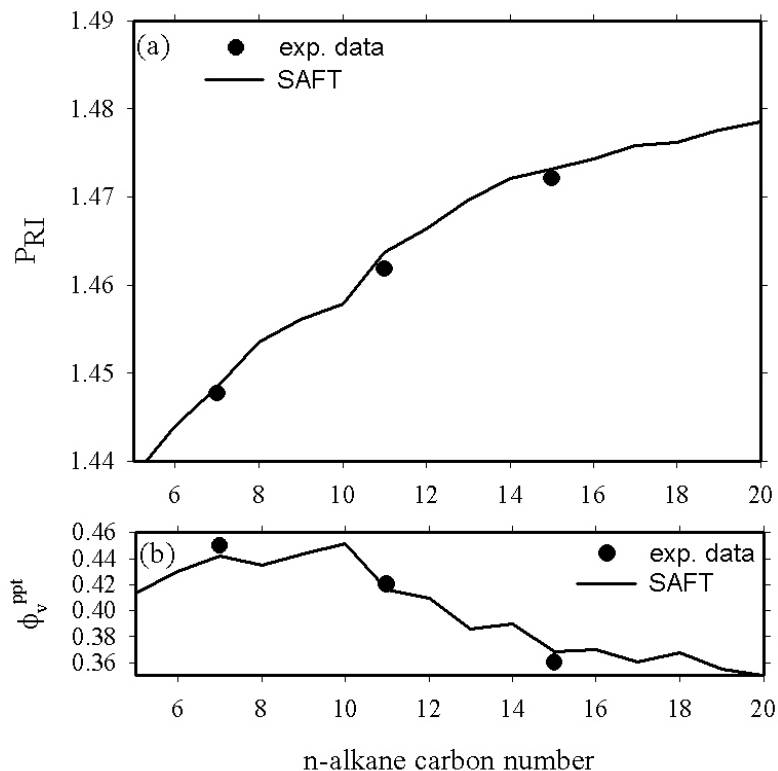


Figure 6.2 SAFT fits to model oil asphaltene aggregates P_{RI} and volume fraction precipitants data.

The ternary phase diagram at 20°C and 1 bar for a mixture of asphaltene, toluene, and n-pentane is shown in Figure 6.3. This plot is representative of asphaltene-toluene-alkane systems under these conditions. The compositions in the figure are in mass fractions. The line connecting the toluene-asphaltene axis to the n-pentane axis gives the mixture composition along the path of titration of a 1 g asphaltene per 100 mL toluene solution. The calculated compositions in Figure 6.2 are essentially the compositions given by the intersection of the titration line with the phase envelope for mixtures of toluene and asphaltene with different n-alkane precipitants. Figure 6.3 shows that a plait point exists for this ternary mixture. This implies that it is possible to phase-split either an asphaltene-rich or an asphaltene-poor phase at initial asphaltene instability onset

depending on the amount of asphaltenes initially present in the system. In the field, both “light” (asphaltene-lean) and “heavy” (asphaltene-rich) precipitated phases have been observed at the onset of asphaltene instability.^[106] Furthermore, information on the compositions along the tie lines may provide insights into the morphology of the various phases. It is interesting to note that the mass fraction of pentane in the asphaltene-rich (“heavy”) phase is relatively constant.

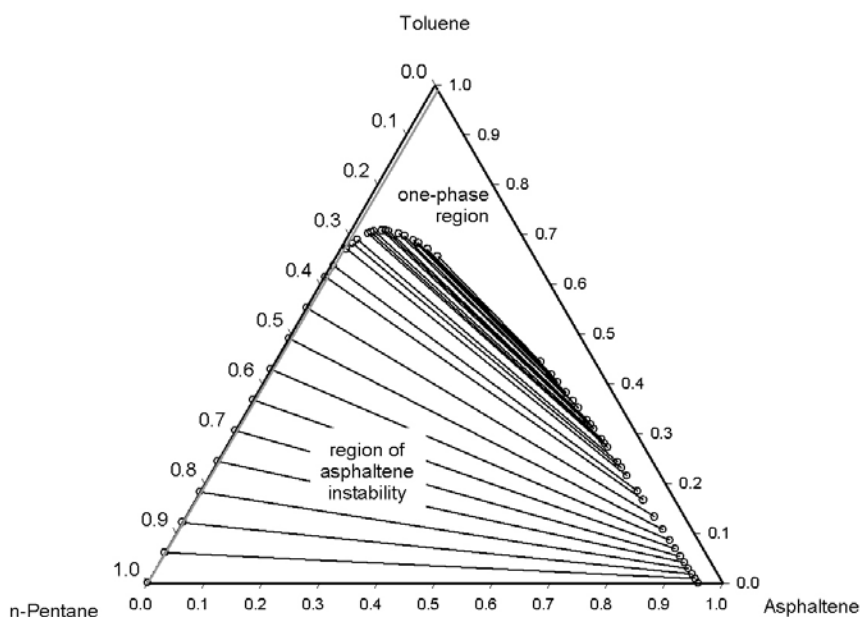


Figure 6.3 Ternary phase diagram at 20°C and 1 bar for a mixture of asphaltene, toluene, and n-pentane. The compositions are in mass fractions.

6.2.2 Comparison of Predicted and Measured Asphaltene Instability Onsets

With the asphaltene parameters determined above, SAFT can be used to predict the phase behavior of the model live oil system (mixture of toluene, methane, and asphaltenes). Comparison between SAFT predictions and

experimental data shows qualitative agreement (Figure 6.4). In these calculations, a temperature independent methane-toluene binary interaction parameter of 0.029 (determined from methane-toluene vapor-liquid equilibria determined in this work and by Elbishlawi and Spencer^[116]) was used and all other binary interaction parameters were set to zero. While SAFT predicts the correct temperature dependence of the asphaltene instability curves, its predictions become worse at higher methane concentrations. In the most part, SAFT calculated asphaltenes are less stable than experimental observations. We believe that the inclusion of asphaltene polydispersity will improve the quality of these predictions.

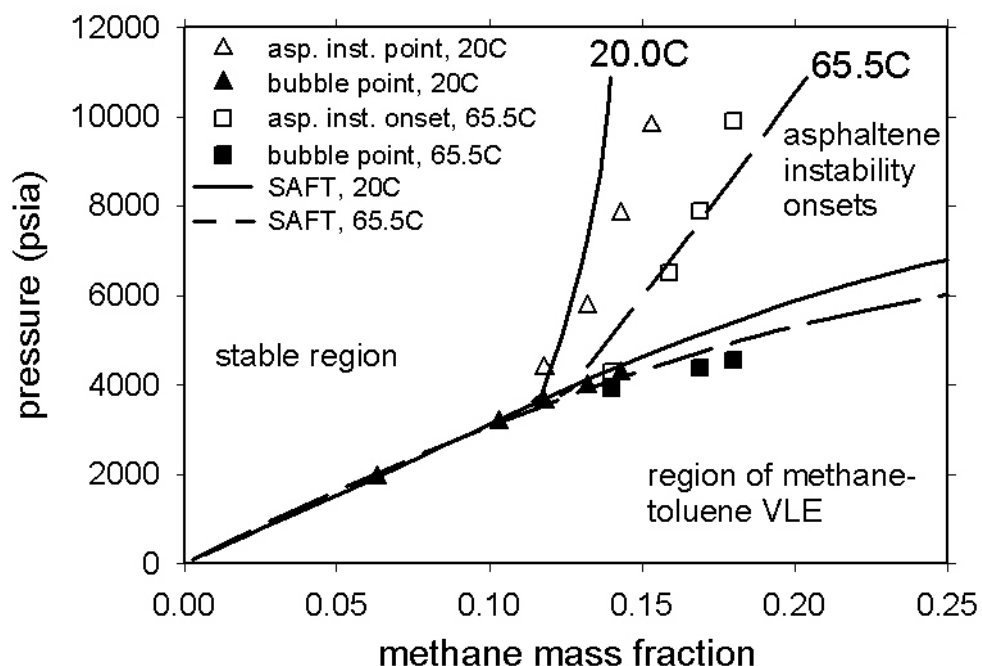


Figure 6.4 Experimental and SAFT-predicted asphaltene instability onsets and bubble points for the model oil at 20.0°C and 65.5°C.

Since the SAFT equation of state provides accurate solubility parameters, we can plot the change in the mixture solubility parameter during pressure depletion. As seen in Figure 6.5 (for the model live oil at 20.0°C with 0.143 mass fraction methane above the bubble point), asphaltenes in the model oil are stable above a certain solubility threshold. Asphaltenes are unstable below the asphaltene instability line shown in Figure 6.5 and are stable above that line. Above the bubble point, asphaltenes are stable at high pressures because of high solvent density. Below the bubble point, asphaltenes are stable at lower pressures because of changing composition (i.e. the light ends start to leave the liquid mixture). As expected, the plot of mixture solubility parameter and the plot of refractive index (the same RI plot in Figure 3.10) show the same behavior because refractive index is a measure of solubility parameter for fluids dominated by nonpolar interactions. The presence of the solubility threshold means that at each temperature, we can estimate whether a reservoir will encounter asphaltene related problems by examining how far the solubility parameter (or refractive index) of the reservoir fluid is from its solubility threshold.

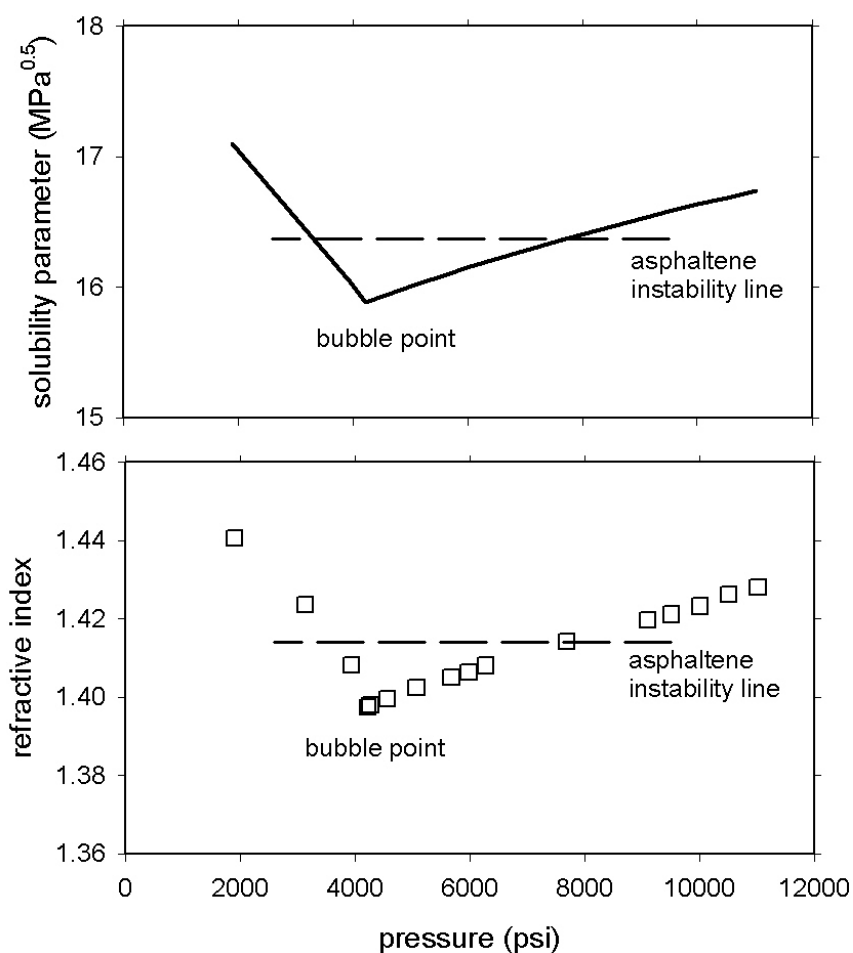


Figure 6.5 Calculated refractive index and SAFT calculated mixture solubility parameter during pressure depletion for the model live oil at 20.0°C with 0.143 mass fraction methane above the bubble point. Asphaltenes are unstable below the asphaltene instability line.

6.3 Recombined Oil Investigations

To model the phase behavior of the recombined oil (stock-tank oil plus its separator gas with compositions given in Table 3.3), the oil is treated as a six pseudo-components mixture. Three sub-fractions (methane, N₂+CO₂, and light n-alkanes) are used to describe the separator gas and three sub-fractions (saturates, aromatics+polynuclear aromatics, and asphaltenes) are used to

describe the stock-tank oil. The relative amount of each sub-fraction can be calculated based on composition data from gas chromatography (GC), SARA fractionation data, and GOR data listed in Chapter 3.

6.3.1 Separator Gas Characterization

The molar composition of the separator gas is listed in Table 6.1 together with each sub-fraction's pseudo-component SAFT parameters. As seen in the table, the average molecular weight of the light n-alkane sub-fraction is similar to that of propane, and a correlation described in the footnote to Table 6.1 is used to calculate the light n-alkane sub-fraction SAFT parameters. Note also that N₂ and CO₂ are modeled as a separate pseudo-component. The SAFT calculated density of 0.3708 g/cm³ obtained from the three pseudo-component treatment of the separator gas compares well with the experimentally determined density of 0.3773 g/cm³ at 241.3 bar and 293K. The binary interaction parameters used between the separator gas sub-fractions are listed in Table 6.2.

Table 6.1 Composition of the separator gas and the pseudo-component SAFT parameters.

component	MW	mole frac.	pseudo-comp. mole frac.	SAFT parameters			
				MW _n	σ (Å)	m	ε/k (K)
CO ₂	44.01	0.0126	0.1510	29.34	3.3130 ^a	1.2053 ^a	90.96 ^a
N ₂	28.01	0.1385					
methane	16.04	0.5063	0.5063	16.04	3.7039	1.0000	150.03
ethane	30.07	0.1320	0.3427	46.61	3.6917 ^b	1.9854 ^b	206.12 ^b
propane	44.09	0.0913					
butane	58.12	0.0719					
pentane	72.15	0.0315					
hexane	86.17	0.0090					
heptane	100.21	0.0045					
octane	114.23	0.0021					
nonane	128.26	0.0005					
Total		1.0000	1.00000				
MW _n	28.524						

a SAFT parameters for N₂ is used because of low CO₂ composition.

b Obtained from molecular weight correlations similar to the n-alkane correlations in Table 4.2, with the exception that the correlation used here was only based on parameters from ethane to decane.

Table 6.2 Binary interaction parameters for the separator gas sub-fractions.

	methane	N ₂ +CO ₂	light n-alkanes
methane	0.000	0.000 ^a	0.011 ^b
N ₂ +CO ₂	0.000 ^a	0.000	0.071 ^c
light n-alkanes	0.011 ^b	0.071 ^c	0.000

a based on methane-N₂ binary data of Kidnay, *et al.*[117]

b based on methane-propane binary data of Reamer, *et al.*[118]

c based on N₂-propane binary data of Grauso, *et al.*[119]

6.3.2 Stock-Tank Oil Characterization

The stock-tank oil is treated as a mixture of 3 pseudo-components (saturates, aromatics+resins, and asphaltenes). The following assumptions are

applied to the oil composition data of Table 3.3 to determine the composition of each sub-fraction:

(1) The entries C_1 to C_9 in Table 3.3 give mass fractions of methane, ethane, propane, butane,..., and nonane. In other words, we assume that the saturates can be distinguished from the aromatics below the C_{10} carbon cut.

(2) 72.3% mass (from SARA analysis) of the materials from the higher carbon cuts (the C_{10} cut and higher) are saturate components. The remaining 27.8% (mass) of the materials are either aromatics+resins (up to, and including the C_{29} cut) or aromatics+resins and asphaltenes (in the C_{30+} cut).

(3) 2.5% mass (from SARA analysis) of the stock-tank oil are asphaltenes, and all asphaltenes are found in the C_{30+} sub-fraction.

(4) The molecular weight distribution (and thus the average molecular weight) of the C_{30+} saturates can be described with the exponential distribution

$$\text{mole amount} = \frac{1}{130} \exp\left[\frac{-(MW - 285)}{130}\right] \quad (6.1)$$

The constants in Eqn. 6.1 were fit to the amount of saturates in the C_{10} to C_{29} sub-fractions (Figure 6.6).

(5) The components in the saturates sub-fraction are all normal alkanes.

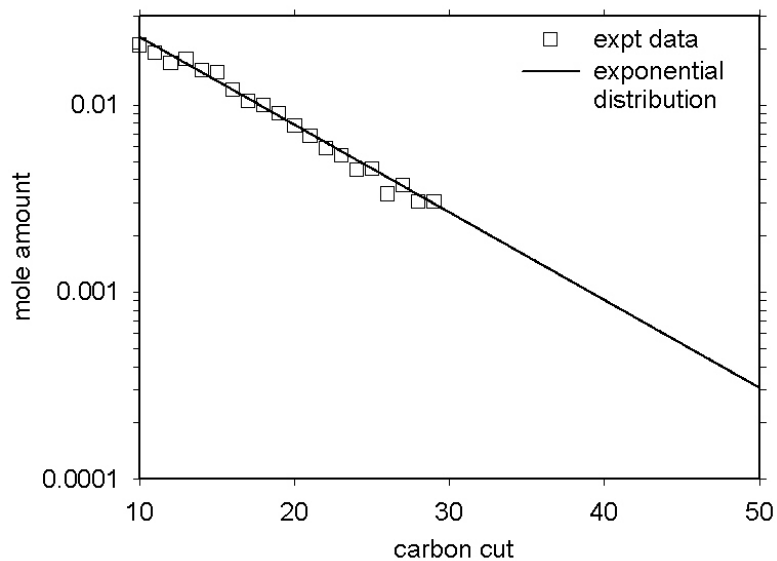


Figure 6.6 Molecular weight distribution of the C₁₀₊ saturates.

Using Eqn. 6.1, the average molecular weight of the C₃₀₊ saturates was found to be about 546 g/mol. The estimated make-up of each oil sub-fraction is listed in Table 6.3. As seen in the table, the proposed fractionation does not noticeably change the pseudo-component mass compositions from those obtained experimentally by SARA fractionation. An average asphaltene molecular weight of 3750 (the MW of the n-C₇ insoluble asphaltenes in the model oil system) is used in these calculations, although the calculated properties are insensitive to the asphaltene molecular weight used because of asphaltene's low concentration.

Table 6.3 Estimated compositions of each stock-tank oil sub-fraction.

Component	SCN properties		saturates sub-fraction			aromatics+resins sub-fraction		
	MW _n	mass frac.	MW _{sat}	mass frac.	norm. mole frac.	MW _{aro+res}	mass frac.	norm. mole frac.
C5	72.15	0.001	72.15	0.001	0.004			
C6	86.2	0.004	86.18	0.004	0.016			
Cyclopentane	84.16	0.001				84.16	0.001	0.007
Benzene	78.11	0.000				78.11	2.3E ⁻⁴	0.003
Cyclohexane	84.16	0.001				84.16	0.001	0.013
Heptane	100.20	0.009	100.20	0.009	0.031			
Cyclohexane	98.19	0.004				98.19	0.004	0.035
Toluene	92.14	0.001				92.14	0.001	0.010
Octane	114.23	0.020	114.23	0.020	0.062			
Ethylbenzene	106.17	0.001				106.17	0.001	0.012
Xylene	106.17	0.005				106.17	0.005	0.038
C9	128.3	0.027	128.25	0.020	0.054	128.43	0.008	0.052
C10	134	0.041	142.29	0.030	0.074	116.31	0.011	0.087
C11	147	0.041	156.31	0.030	0.067	127.21	0.011	0.079
C12	161	0.040	170.34	0.029	0.060	140.84	0.011	0.069
C13	175	0.045	184.37	0.033	0.063	154.51	0.013	0.071
C14	190	0.042	198.39	0.031	0.055	171.10	0.012	0.060
C15	206	0.044	212.42	0.032	0.053	190.93	0.012	0.056
C16	222	0.038	226.45	0.027	0.043	211.17	0.010	0.044
C17	237	0.035	240.47	0.025	0.037	228.39	0.010	0.037
C18	251	0.035	254.50	0.025	0.035	242.30	0.010	0.035
C19	263	0.034	268.53	0.024	0.032	249.58	0.009	0.033
C20	275	0.031	282.55	0.022	0.028	257.06	0.008	0.029
C21	291	0.028	296.56	0.020	0.024	277.41	0.008	0.025
C22	305	0.025	310.59	0.018	0.021	291.31	0.007	0.021
C23	318	0.024	324.61	0.017	0.019	301.93	0.007	0.020
C24	331	0.021	338.64	0.015	0.016	312.58	0.006	0.017
C25	345	0.022	352.67	0.016	0.016	326.47	0.006	0.017
C26	359	0.017	366.69	0.012	0.012	340.36	0.005	0.012
C27	374	0.020	380.72	0.014	0.013	357.53	0.005	0.013
C28	388	0.017	394.74	0.012	0.011	371.43	0.005	0.011
C29	402	0.017	408.77	0.013	0.011	385.33	0.005	0.011
C30+	580	0.307	546.00	0.222	0.145	640.75	0.060	0.083
Total mass/mole frac.		1.000		0.723	1.000		0.252	1.000
Average MW			255.00			222.00		

The SAFT parameters for the saturates sub-fraction can be calculated from the sub-fraction's average molecular weight using the n-alkane correlations first given in Table 4.2 and reproduced in Table 6.5. The correlated SAFT

parameters of the saturates sub-fraction are listed in Table 6.4. In using these correlations, we assume (assumption 5) that all saturates are normal alkanes. Comparison of SAFT calculated densities of the saturates-only mixture at representative pressures and temperatures using the one-fluid (pseudo-component) and the full 26-components treatment is shown in Figure 6.7. As expected, the results of the one-fluid and the full 26-components treatment are similar because SAFT uses the conformal solution mixing rule to describe mixture properties.

Table 6.4 SAFT parameters for the non-asphaltene stock-tank oil pseudo-components.

	saturates	aromatics + resins
MW_n	255	222
m	7.377	5.335
$\sigma (A)$	3.964	3.764
$\epsilon/k(K)$	257.1	323.7

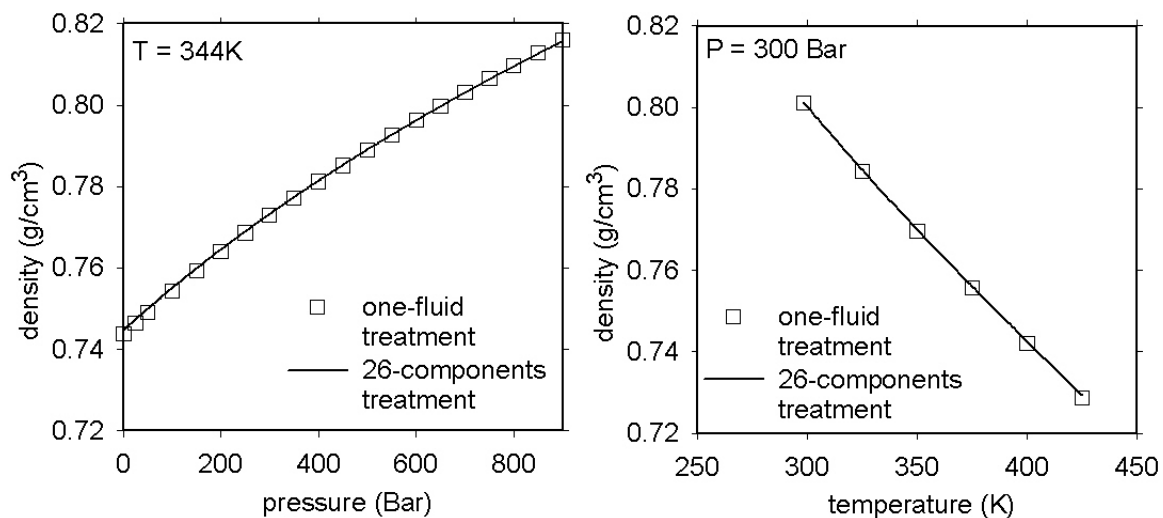


Figure 6.7 Comparison of SAFT calculated densities for the mixture of saturates using the one-fluid treatment and the 26-components treatment.

The SAFT parameters for the aromatics+resins sub-fraction (listed in Table 6.4) depend not only on the average molecular weight but also on the average aromaticity of the sub-fraction. This is because the aromatics+resins sub-fraction is a mixture of aromatics, polynuclear aromatics (PNA), PNA derivatives, and resins that span a range in terms of the aromaticity of each molecular constituents. For instance, if a mixture contains a lot of alkyl-benzenes and very little polynuclear aromatics, it is, on average, less “aromatic” than a mixture consisting mostly of polynuclear aromatics. Since the SAFT parameters for compounds in each of these classes follow different parameter correlation curves (see Figure 4.7), it is important to quantify this “degree of aromaticity”. We have defined a fitting parameter γ , which we call the aromaticity parameter, that would relate the degree of aromaticity of the aromatics+resins sub-fraction to the SAFT parameter correlations used to calculate the sub-fraction’s SAFT

parameters (see Table 6.5). With $\gamma = 0$, the correlation for the aromatics+resins sub-fraction reduces to the correlation for PNAs'. With $\gamma = 1$, the correlation reduces to the correlation for benzene, biphenyl, and ter-phenyl.

Table 6.5 SAFT parameter correlations for the saturates and aromatics+resins oil sub-fractions. γ is a ratio parameter related to the degree of aromaticity.^a

	saturates	aromatics + resins ^a
correlation for m	$0.0253MW+0.9263$	$\gamma(0.0201MW+0.7860)+$ $(1-\gamma)(0.0139MW + 1.2988)$
Correlation for $m\sigma$	$0.1037MW+2.7985$	$\gamma(0.0782MW+2.466) +$ $(1-\gamma)(0.0597MW + 4.2015)$
Correlation for ε/k	$32.81\ln(MW)+80.398$	$\gamma(40.65\ln(MW)+112.4) +$ $(1-\gamma)(119.41\ln(MW)-230.21)$

a The ratio $\gamma = 1.1$ was chosen so that (1) the recombined oil would reproduce the correct bubble point and (2) asphaltenes would be soluble in the aromatics+resins pseudo-component fluid. The two sets of bracketed correlations are those for the polynuclear aromatics and those for benzene, biphenyl, and terphenyl.

We grouped aromatics and resins into one single pseudo-component because they form a part of the same distribution (that actually extends out to the asphaltenes).

To pin down a set of parameters for the aromatics+resins sub-fraction, the following procedure can be used. Starting with the set of SAFT parameters for n-alkanes at $MW_n=222$, we slowly increase γ , the aromaticity parameter, until (1) the predicted stock-tank oil density at ambient conditions matches the

experimental density and (2) the n-C₇ insoluble asphaltene in the model oil investigations becomes completely soluble in a fluid composed of only the aromatics+resins sub-fraction. Since the SAFT parameters for the stock-tank oil asphaltenes have not yet been determined, the n-C₇ insoluble asphaltene used in the model oil investigations can be used in the density calculations. Recall that the parameters for the model oil asphaltenes were determined from ambient condition titration in n-alkane precipitants + toluene. The binary interaction parameter between the saturates and the aromatics+resins pseudo-components are set to -0.01 based on the optimal k_{ij} for toluene-dodecane and toluene-hexadecane VLE data^[120] at 353K and 333K.

The SAFT equation of state parameters for the aromatics+resins pseudo-component are listed in Table 6.4 and were obtained using the listed correlations; the γ parameter adjusts for the degree of aromaticity and has a value of 1.1 for this oil. With $\gamma = 0$, the correlation reduces to the correlation for PNAs'. With $\gamma = 1$, the correlation reduces to the correlation for benzene, biphenyl, and terphenyl. A comparison of the calculated and experimental stock-tank oil densities show good agreement; the deviation at 293K and 1 bar between experimental (0.857 g/cm³) and calculated (0.864 g/cm³) densities is about 0.8% and the deviation at 328K and 1 bar between experimental (0.848 g/cm³) and calculated (0.839 g/cm³) densities is about -1%. The good agreement is not surprising because the density data at 293K and 1 bar was used to fit the pseudo-component SAFT parameters for the aromatics+resins sub-fraction. Comparison

of SAFT calculated densities using the aromatics+resins one-fluid treatment and the full 29-components treatment (similar to what was done in Figure 6.7) also shows good agreement, with deviations of less than 0.13% in the temperature and pressure ranges in Figure 6.7.

The asphaltene SAFT parameter fitting procedure used in the model oil investigations (Figure 6.1) is used to fit asphaltene SAFT parameters for the stock-tank oil. Because of the complexity in composition of the stock-tank oil, the correlation

$$\frac{n^2 - 1}{n^2 + 2} = \frac{\delta - 4.7943}{44.377} \quad (6.2)$$

is used instead of Eqn. 3.1 to relate calculated solubility parameters (in $\text{Mpa}^{0.5}$) to refractive indices. A plot of Eqn. 6.2 with experimental solubility parameter and refractive index function of some selected compounds is shown in Figure 6.8. Note that the refractive index in Figure 6.8 was measured at 20°C while the solubility parameter was measured at 25°C.

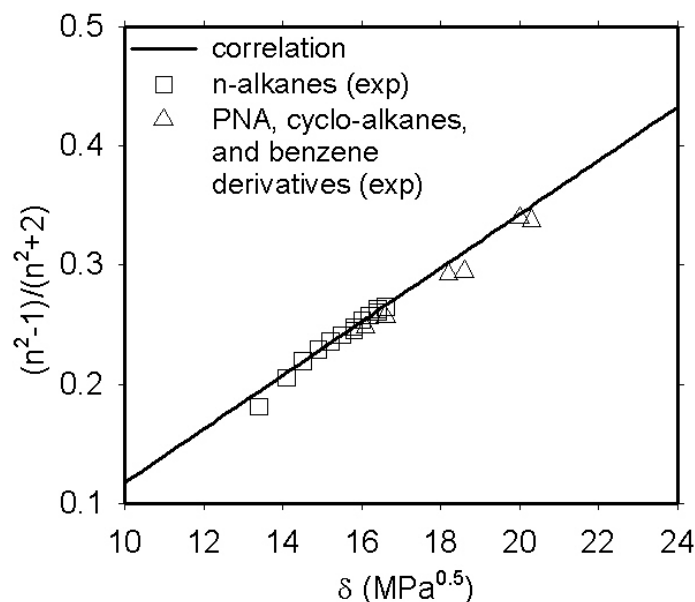


Figure 6.8 Relationship between solubility parameter^[121] (δ , at 25°C) and refractive index^[44] (at 20°C) for some select compounds.

As described in Chapter 3 (see Table 3.2), the stock-tank oil was initially mixed with equi-volume of α -methyl naphthalene. For a given oil/precipitant pair, the addition of asphaltene solvents to the oil shifts the amount of precipitant needed to induce asphaltene precipitation but does not significantly alter the refractive index at precipitation onset.^[40] As in the model oil asphaltene fits, the binary interaction parameters between asphaltenes and the other stock-tank oil components (and α -methyl-naphthalene) are set to zero. The set of k_{ij} 's used between the various components are listed in Table 6.6. These interaction parameters were based on k_{ij} 's between representative species of the oil sub-fractions described in the footnotes of Table 6.6.

Table 6.6 Binary interaction parameters used to fit the stock-tank oil asphaltenes in SAFT.

	saturates	aromatics+ resins	α -methyl naph. ^b	n-alkane ppt. ^c	asphaltenes
Saturates	0.00	-0.01 ^a	-0.01	0.00	0.00
aromatics+ resins	-0.01 ^a	0.00	0.00	-0.01	0.00
α -methyl naph. ^b	-0.01	0.00	0.00	-0.01	0.00
n-alkane ppt. ^c	0.00	-0.01	-0.01	0.00	0.00
Asphaltenes	0.00	0.00	0.00	0.00	0.00

a based on toluene-dodecane and toluene-hexadecane binary data of Messow and Engel^[120]

b the k_{ij} 's between α -methyl naphthalene and other species are the same as those between aromatics+resins and other species.

c the k_{ij} 's between n-alkane precipitants and other species are the same as those between saturates and other species.

The fitted stock-tank oil asphaltenes has the following parameters: $\sigma = 4.30$ Angstrom, $m = 29.5$, $\epsilon/k = 395$ K. This asphaltene has a SAFT calculated solubility parameter of $21.85 \text{ MPa}^{0.5}$ and a molar volume of $1,437 \text{ cm}^3/\text{mol}$. Given that the density of asphaltenes is estimated to be between 1.13 g/cm^3 and 1.20 g/cm^3 , the SAFT calculated stock-tank oil asphaltene has an implied MW between 1624 and 1724. Results of the fits are given in Figure 6.9. A comparison of the stock-tank oil SAFT asphaltene parameters and the n-C₇ insoluble model oil SAFT asphaltene parameters is given in Table 6.7.

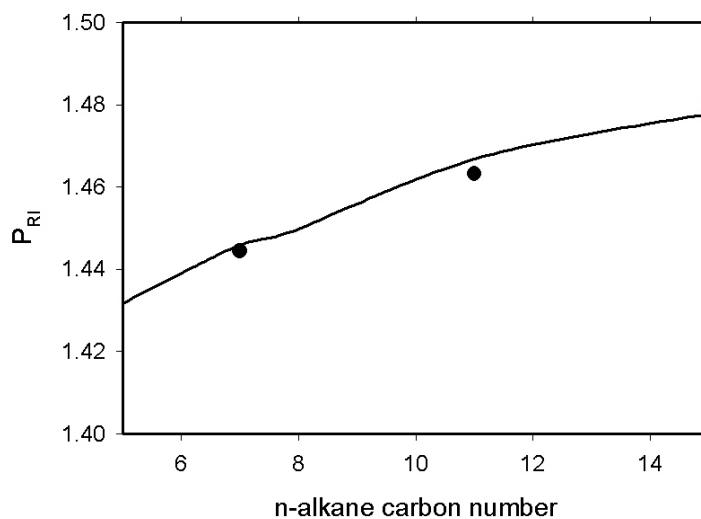


Figure 6.9 SAFT fits to stock-tank oil asphaltene aggregates P_{RI} data.

Table 6.7 Comparison of stock-tank oil SAFT asphaltene parameters and the n-C₇ insoluble model oil asphaltene parameters.

	stock-tank oil asphaltene	n-C ₇ insoluble model oil asphaltene
m	29.5	80.0
σ (Angstrom)	4.30	4.05
ε/k (K)	395	350.8
δ (MPa ^{0.5})	21.85	21.85
molar volume (cm ³ /mol)	1,437	3,334
MW (range)	1,624-1,724	3,767-4,000

A comparison of the SAFT parameters for the stock-tank oil asphaltenes and the n-C₇ extracted asphaltenes used in the model live oil (Table 6.7) shows that the stock-tank oil asphaltenes are, on average, smaller and more polarizable. This is expected. We recognize that the stock-tank oil asphaltenes are polydisperse in size, shape, and molecular composition. We modeled the

asphaltenes as a monodisperse species with the SAFT parameters giving average properties. The n-C₇ insoluble product of the extraction process is a high molecular weight sub-fraction of the stock-tank oil asphaltenes. The difference in the two sets of SAFT parameters reflects the difference in physical properties between the average n-C₇ insoluble and stock-tank oil asphaltenes. This information can be used together with data on the precipitation behavior of other n-alkane extracted asphaltenes to estimate the stock-tank oil asphaltene's degree of polydispersity.

6.3.3 Recombined Oil Properties

Before the pure component SAFT parameters listed above can be used to model the recombined oil system, the binary interaction parameters between the pseudo-components in oil need to be determined. These binary interaction parameters are given in Table 6.8 and were obtained from k_{ij} 's between the sub-fractions' representative species (see table footnotes). For instance, the interaction parameter between propane (MW = 44.1) and hexadecane (MW = 226.4) can be used in place of the interaction parameter between saturates (MW_n = 255) and light alkanes (MW_n = 46.6) sub-fractions. Although the MW_n of the saturates sub-fraction is closer to the molecular weight of octadecane than hexadecane, hexadecane is used as the representative species for saturates because of constraints in the availability of published data. Whenever strongly temperature-dependent k_{ij} 's were observed, the values listed in Table 6.8 were interpolated/extrapolated to the k_{ij} values between 300K and 350K.

Table 6.8 Binary interaction parameters between pseudo-component species in SAFT.

	methane	N ₂ +CO ₂	light n-alkanes	saturates	aromatics +resins	asphaltenes ^k
methane	0.00	0.00 ^a	0.01 ^b	0.03 ^d	0.03 ^e	0.03
N ₂ +CO ₂	0.00 ^a	0.00	0.07 ^c	0.01 ^f	0.13 ^h	0.13
light n-alkanes	0.01 ^b	0.07 ^c	0.00	0.006 ^g	0.02 ⁱ	0.00
saturates	0.03 ^d	0.01 ^f	0.006 ^g	0.00	-0.01 ^j	0.00
aromatics +resins	0.03 ^e	0.13 ^h	0.02 ⁱ	-0.01 ^j	0.00	0.00
asphaltenes ^k	0.03	0.13	0.00	0.00	0.00	0.00

a based on methane-N₂ binary data of Kidnay, *et al.*[117]

b based on methane-propane binary data of Reamer, *et al.*[118]

c based on N₂-propane binary data of Grauso, *et al.*[119]

d based on methane-decane data of Reamer, *et al.*[111]

e based on methane-toluene binary data reported in this work and from Elbishlawi and Spencer[116]

f based on N₂-decane binary data of Azarnoosh and McKetta[122]

g based on propane-hexadecane binary data of Joyce[102]

h based on N₂-benzene binary data of Miller and Dodge[123]

i based on propane-benzene binary data of Glanville, *et al.*[124]

j based on toluene-dodecane and toluene-hexadecane binary data of Messow and Engel[120]

k the k_{ij} 's between asphaltenes and separator gas sub-fractions are assumed to be the same as the k_{ij} 's between aromatics+resins and separator gas sub-fractions.

To calculate the amount of separator gas in the recombined oil, the gas-oil ratio can be converted to molar quantities (of gas) per mass stock-tank oil:

$$\frac{\text{moles gas}}{\text{mass STO}} = \text{GOR}^{20\text{C}, 1\text{bar}} \left(\frac{100\text{cm}}{\text{m}} \right)^3 \rho_{\text{gas}}^{20\text{C}, 1\text{bar}} \text{MW}_{\text{gas}} \quad (6.3)$$

where GOR is in m³/m³, the average molecular weight of the separator gas is 28.52, and the density of the separator gas at 293 K and 1 bar is approximately 0.0012 g/cm³ using the ideal gas equation of state.

A comparison of SAFT-predicted and experimental densities (along the depressurization experiments) for the one-phase recombined oil with a gas-oil ratio of $152 \text{ m}^3/\text{m}^3$ and a GOR of $212 \text{ m}^3/\text{m}^3$ is shown in Figure 6.10. Although SAFT slightly under-predicts the recombined oil densities, the predicted densities are in good agreement with experimental values. As described in Chapter 3 (see Figure 3.7b), the experimental densities were obtained from constant-composition volume-expansion data.

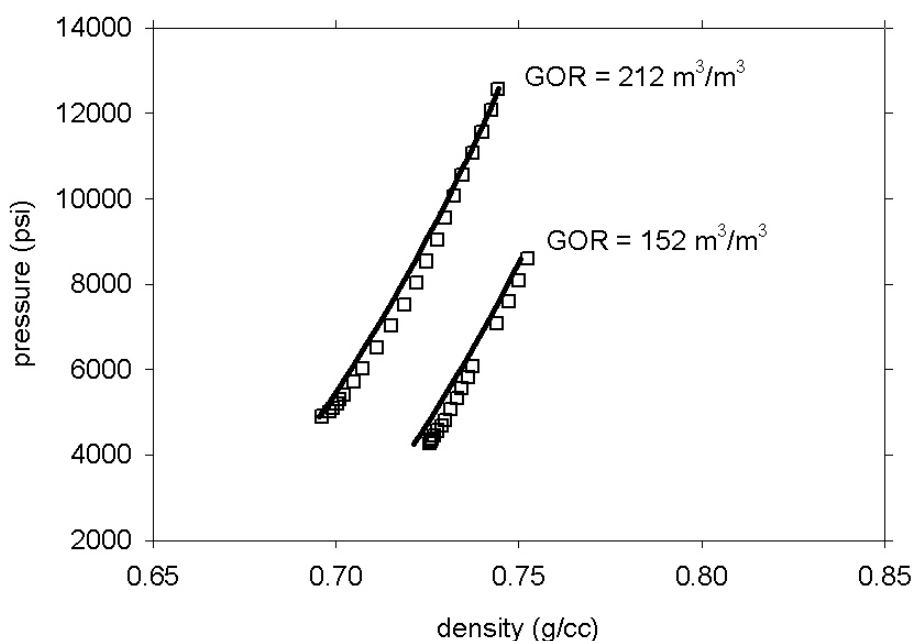


Figure 6.10 Experimental and SAFT-predicted (lines) one-phase recombined oil densities with two different gas-oil ratios.

Comparison of SAFT-predicted and measured bubble points for the recombined oil with the two different gas-oil ratios is shown in Figure 6.11. As seen in the figure, SAFT accurately describes the effect of gas concentration on bubble point pressures. The predicted mixture bubble points for two limiting scenarios of separator gas compositions are also plotted in the figure. In the first

scenario (limiting case 1 in Figure 6.11), all separator gas is assumed to be methane. In the second scenario (limiting case 2 in the figure), we assume that N_2 and CO_2 are light alkanes in the separator gas (i.e. the concentration of light alkanes is increased by the amount of N_2 and CO_2 in the system, and the contribution due to N_2 and CO_2 are ignored). As seen in the figure, SAFT correctly overpredicts the bubble points in the first limiting scenario and underpredicts the bubble points in the second limiting scenario.

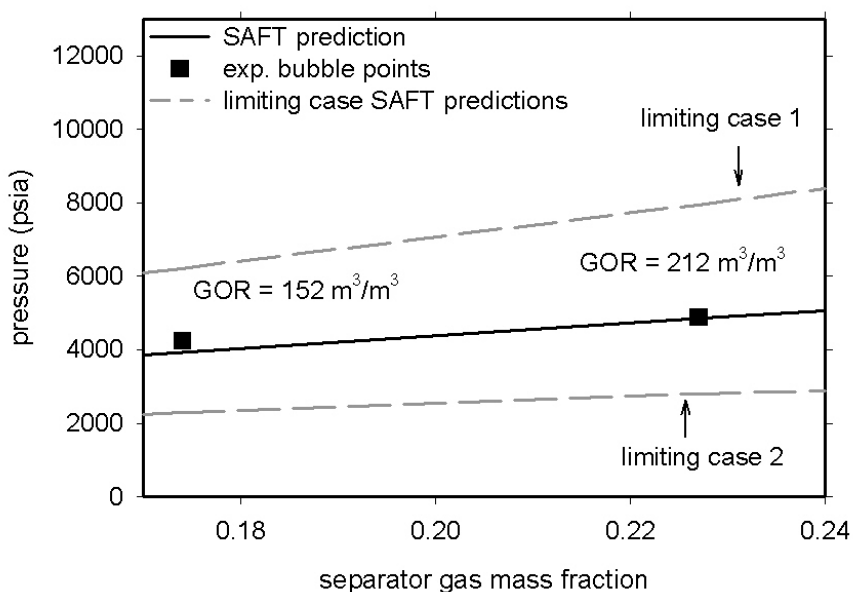


Figure 6.11 Comparison of SAFT-predicted and measured bubble points for the recombined oils.

6.3.4 Comparison of Predicted and Measured Asphaltene Instability Onsets

The SAFT-predicted asphaltene instability onset and bubble point pressures for the recombined oil at $71.1^{\circ}C$ are plotted in Figure 6.12 together with experimental data. SAFT predicts accurately both the bubble points and the asphaltene instability onset points for this oil in the composition range

investigated. According to the equation of state calculations, we would expect asphaltene precipitation problems to occur at higher separator gas concentrations.

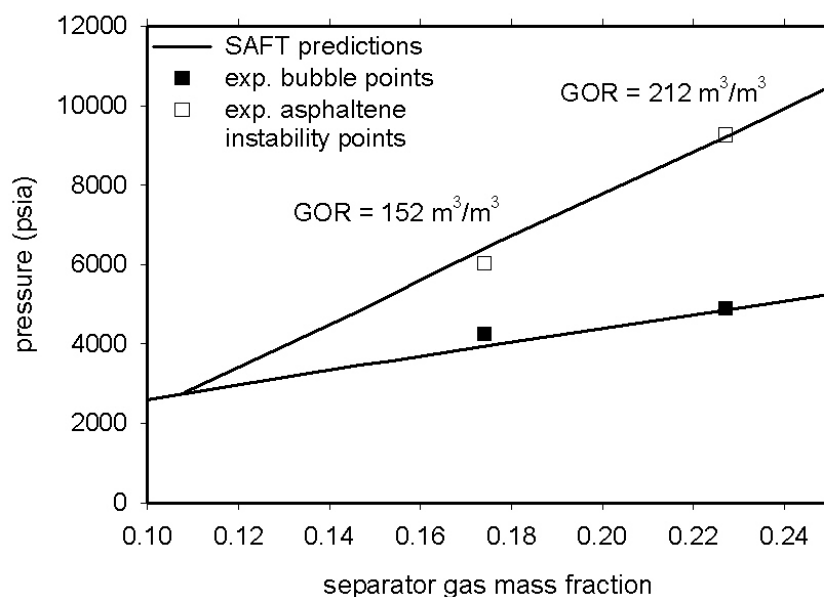


Figure 6.12 SAFT-predicted and measured asphaltene instability onset and mixture bubble points for the recombined oil at 71.1°C.

6.4 Summary

A method has been presented to characterize the recombined oil and the asphaltenes for use in the SAFT equation of state. The recombined oil was modeled as a six-component mixture, with three pseudo-components for the stock-tank oil and three pseudo-components for the separator gas. The average molecular weight and the amount of each sub-fraction was determined from gas-chromatography, saturates-aromatics-resins-asphaltenes fractionation, and gas-oil-ratio information. SAFT parameters for each sub-fraction (except for the

asphaltenes) were obtained from correlations with molecular weight for each class of compounds. The SAFT-predicted densities for the stock-tank oil and the recombined oils agree very well with experimental measurements.

P_{RI} data was used to fit the asphaltene's SAFT parameters. Essentially, the SAFT asphaltene parameters were optimized so that SAFT would reproduce the composition of the mixture (or the refractive index of the mixture) at the onset of asphaltene precipitation. For both the model oil and the stock-tank oil, good agreements were obtained between experimental and fitted P_{RI} even with a binary interaction parameter of zero between asphaltenes and the other species. While the stock-tank oil and the model oil asphaltenes thus obtained have almost the same solubility parameter, according to SAFT, the stock-tank oil asphaltenes are much smaller and more aromatic.

For both the model and the recombined oil systems, SAFT-predicted asphaltene instability and bubble points agree well with experimental measurements.

CHAPTER 7. ASPHALTENE SAFT PARAMETERS SELECTION RULES

7.1 Introduction

As described in Chapter 6, the SAFT equation of state parameters for asphaltenes (m , σ , and ϵ/k) are fit to ambient condition precipitation data from oil titrations with n-alkanes. In this section, we will investigate the effects of varying one or more of these parameters on the calculated asphaltene instability onset compositions. We will also look at the effects of changing these parameters on a pure species' solubility parameter (δ) and molar volume (v). These investigations will provide some general guidelines on selecting the appropriate set of asphaltene SAFT parameters to fit the ambient condition titration data.

7.2 Effects of Variations in SAFT Parameters on Solubility Parameter

The effects of varying a pure specie's chain length (m), segment diameter (σ), and segment energy (ϵ/k) on the calculated solubility parameter (20°C, 1 bar) are shown in Figures 7.1(a) to 7.1(c). The range of SAFT parameters investigated ($14 \leq m \leq 90$; $3.9\text{\AA} \leq \sigma \leq 4.1\text{\AA}$; $280\text{K} \leq \epsilon/k \leq 400\text{K}$) roughly span the parameter space where we expect asphaltenes to lie. Compared to the range of m and ϵ/k investigated, the range of σ investigated is small because σ does not vary much between species (see Table 4.1). The gray horizontal lines in Figures 7.1(a)-(c) demarcate the measured upper and lower values of solubility

parameter for asphaltenes; these lines mark the boundaries within which potential asphaltene SAFT parameters would be found.

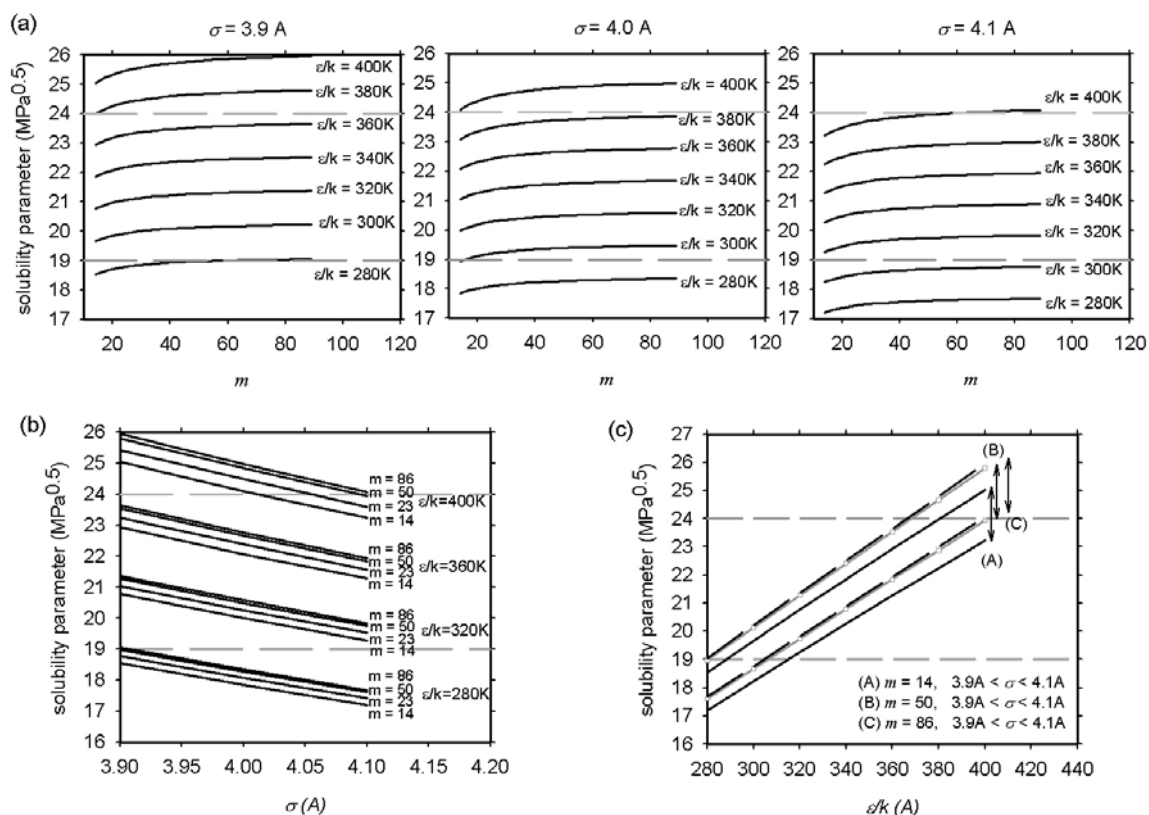


Figure 7.1 Effects of variations in m , σ , and ϵ/k on the calculated solubility parameters at 20°C and 1 bar. The three plots contain the same data.

As seen in Figure 7.1, with all other parameters held constant, the solubility parameters are not very sensitive to changes in molecular chain length. For instance, at $\sigma = 4.0\text{\AA}$ and $\epsilon/k = 340\text{K}$, a 50% increase in m from 44 to 66 results in a 0.4% increase in δ . This implies that for a given set of segment properties (ϵ/k and σ) in the region of SAFT parameter space investigated, the ratio of the residual internal energy to the molecular volume (i.e. the solubility parameter) is relatively independent of chain length. Since the residual internal

energy is approximately proportional to chain length at fixed mass density and temperature, the molar volume is also proportional to chain length.

Unlike the case with m , the solubility parameters are sensitive to small changes in the segment properties ϵ/k and σ . A decrease in the segment energy will decrease the solubility parameter (see Figure 7.1(c)), and a decrease in the segment diameter will increase the solubility parameter (see Figure 7.1(b)). For instance, at $m = 50$ and $\sigma = 4.0\text{\AA}$, a 2.5% decrease in ϵ/k from 400K to 390K results in a 2.2% decrease in δ . And at $m = 50$ and $\epsilon/k = 400\text{K}$, a 2.5% decrease in σ from 4.0\AA to 3.9\AA results in a 3.7% increase in δ . In both instances, the molecule's energy density has been altered.

7.3 Effects of Variations in SAFT Parameters on Molar Volume

The effects of varying a pure specie's chain length, segment diameter, and segment energy on its molar volume (at 20°C, 1 bar) can be seen in Figure 7.2. The range of SAFT parameters investigated is the same as those in the previous section. As seen in the figure, molar volume is a linear function of m . As expected, increasing the segment diameter σ increases the molar volume while increasing the segment energy ϵ/k has the opposite effect. It is interesting that the effects of changes in the segment properties (σ and ϵ/k) are more pronounced in molecules with longer chains (larger values of m). Because of the

large differences in the reported asphaltene molecular weights, an asphaltene molecule would fall within the range of molar volumes in Figure 7.2.

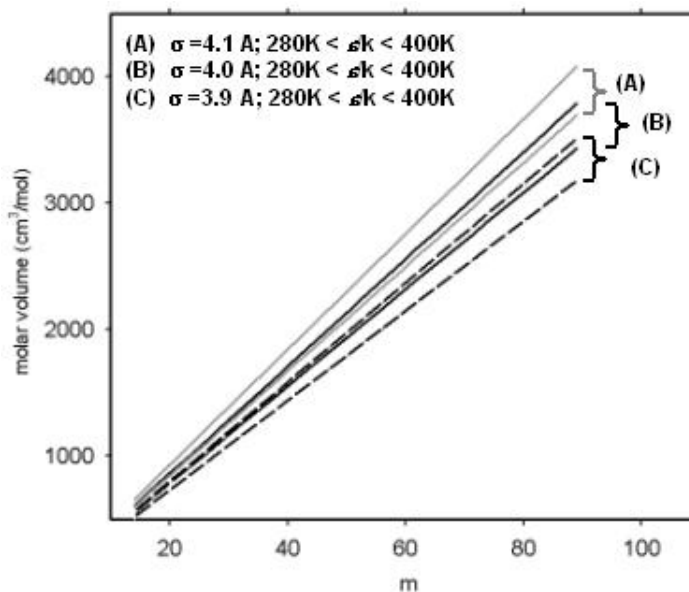


Figure 7.2 Effects of variations in m , σ , and ϵ/k on calculated molar volumes at 20°C, 1 bar. All else being equal, molecules with lower ϵ/k have larger molar volumes.

7.4 Effects of Variations in Asphaltene SAFT Parameters on Mixture Composition at Asphaltene Instability Onset

The effects of varying each of the asphaltene SAFT parameters on the calculated asphaltene-toluene-n-alkane mixture composition at asphaltene instability onset are shown in Figure 7.3. As described earlier, ϕ_{ppt}^V is the volume fraction of the precipitant in a mixture of asphaltene-toluene-n-alkane at the onset of asphaltene instability. The concentration of asphaltenes in these calculations is fixed at 1g asphaltenes per 100mL toluene (at 20°C, 1 bar). Since the asphaltene molar volume calculated using each set of SAFT parameters is

different, the molecular weight of the asphaltenes are allowed to vary to maintain an asphaltene mass density of 1.126 g/cc. As detailed in Chapter 6, the binary interaction parameters between all species are set to zero. To check for phase stability of the asphaltene-toluene-n-alkane mixtures, we use, as initial guesses, a composition grid of 0.04 in each direction. An unstable phase is defined (numerically) as one in which the tangent plane distance (see Chapter 4) has a value more negative than -1.0×10^{-14} .

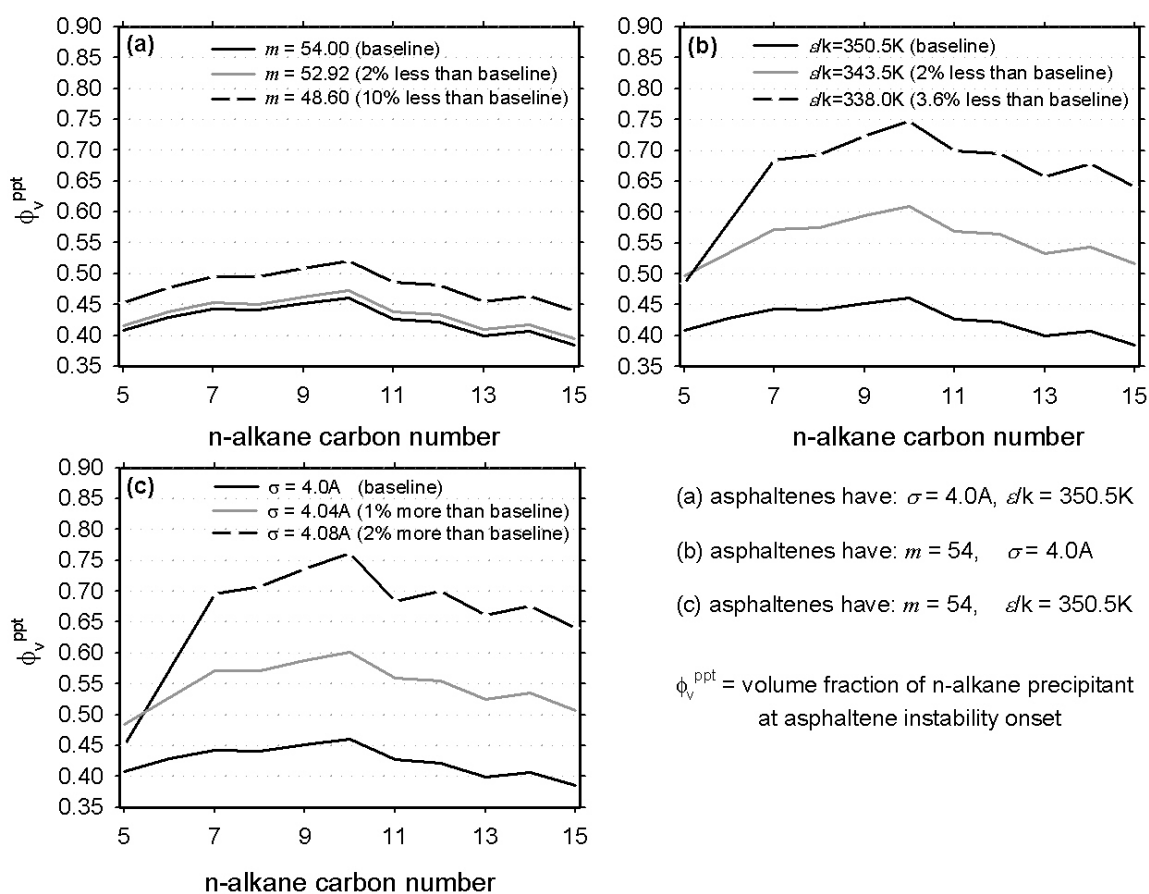


Figure 7.3 Effects of changing (a) m , (b) ϵ/k , and (c) σ for asphaltenes on the amount of n-alkane precipitants needed to induce asphaltene instability in the asphaltene-toluene-n-alkane mixtures.

As seen in Figure 7.3(a), decreasing m (while holding the other parameters constant) will increase the volume fraction (ϕ_v^{ppt}) of n-alkane precipitants needed to induce asphaltene instability. Since the magnitude of change in ϕ_v^{ppt} is almost constant for all n-alkane precipitants investigated, the overall effect of changing m for asphaltenes is a translation of the instability onset curve (on a plot of ϕ_v^{ppt} vs. n-alkane carbon number).

The effect of changing ϵ/k for asphaltenes on the calculated ϕ_v^{ppt} is shown in Figure 7.3(b). Decreasing the segment energy lowers the energy density of the asphaltene molecules and increases the amount of n-alkane precipitants needed to induce asphaltene instability. A comparison of the plots in Fig. 7.3(a) and (b) shows that ϕ_v^{ppt} is much more sensitive to changes in ϵ/k than to changes in m . For instance, a 2% decrease in m would, on average, increase the amount of n-alkane precipitants needed to induce asphaltene instability by about 2.5%; a 2% decrease in ϵ/k would, on the other hand, increase ϕ_v^{ppt} by about 30%. Furthermore, unlike changing m , changing ϵ/k alters the curvature of the ϕ_v^{ppt} vs. n-alkane carbon number curve.

Figure 7.3(c) shows the effect of changing σ for asphaltenes on the calculated precipitant volume fraction in the asphaltene-toluene-n-alkane mixture at asphaltene instability onset. As seen in the figure, the overall effects of changing σ (on ϕ_v^{ppt}) are similar to that of changing ϵ/k and the calculated asphaltene instability onset compositions are even more sensitive to changes in

σ than to ϵ/k . This is not surprising because unlike changes in ϵ/k (which directly changes the molecular energy density but only indirectly changes the molar volume), changing σ directly changes the molar volume and the molecular energy density. Since changing ϵ/k and σ for asphaltenes have qualitatively similar effects on ϕ_v^{ppt} , the issue of parameter uniqueness becomes important. This issue will be addressed in the following section.

An example of the combined effects of changing ϵ/k and m on the calculated ϕ_v^{ppt} is given in Figure 7.4. In these calculations, the segment diameter of the asphaltenes is fixed at 4.0 Å. As seen in the figure, one way to increase the curvature of the ϕ_v^{ppt} vs. n-alkane carbon number plot is to first decrease the segment energy of the asphaltene and then increase its segment number to reduce the volume fraction of precipitants needed to induce asphaltene instability.

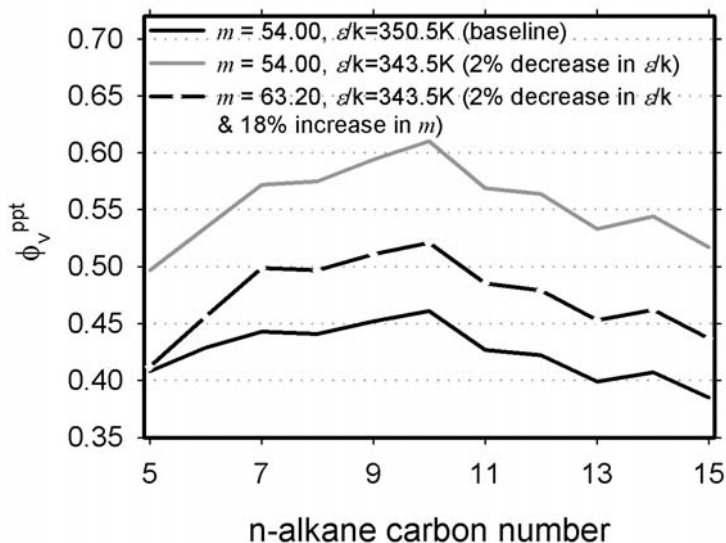


Figure 7.4 Effects of m and ϵ/k for asphaltenes on calculated volume fraction of precipitants at the onset of asphaltene instability at 20°C and 1 bar.

7.5 Uniqueness of the Asphaltene SAFT Parameters

Since changing ϵ/k and σ for asphaltenes have qualitatively similar influences on the calculated amount of precipitants needed to induce asphaltene instability, the issue of parameter uniqueness becomes important. In other words, can we fit an experimental ϕ_v^{ppt} (and hence P_{RI}) curve using different sets of asphaltene SAFT parameters?

In Figure 7.5, the ϕ_v^{ppt} vs. n-alkane carbon number curve is plotted for six sets of asphaltene SAFT parameters, all with $m = 54$. As seen in the figure, in three cases, two independent sets of parameters produce nearly identical results. This suggests that, in modeling the ambient condition ϕ_v^{ppt} and P_{RI} curves, it is possible to fit the experimental data using multiple sets of asphaltene SAFT

parameters. Further investigation (Figure 7.6) shows that, given a set of asphaltene SAFT parameters, another set of parameters can be chosen to give similar instability onset compositions if it lies on a line $\varepsilon/k \approx 175\sigma - b$ where the intercept, b , is calculated from the given set of SAFT parameters. Interestingly, the calculated solubility parameters and molar volumes of asphaltenes with parameters along these lines have different values. In the past, the problem of parameter uniqueness has not been an issue when a pure specie's SAFT parameters are fit to its vapor pressures and liquid densities.

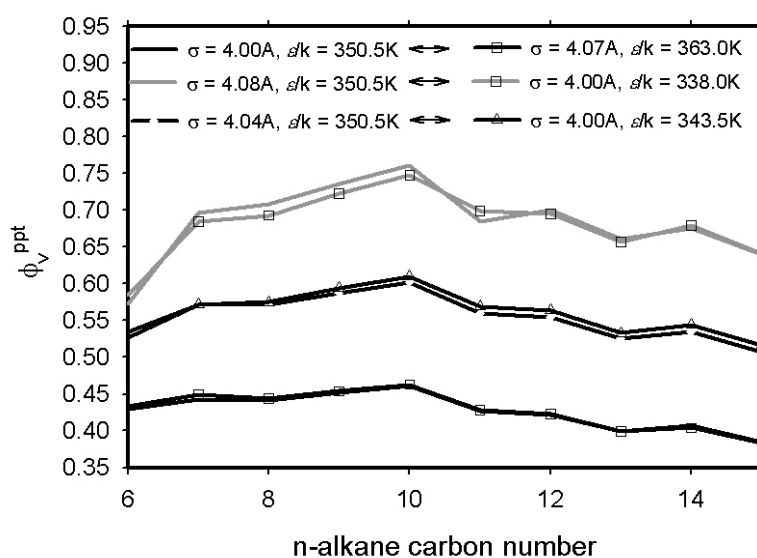


Figure 7.5 Calculated precipitant volume fractions at asphaltene instability onset (ϕ_v^{ppt}) using different sets of asphaltene SAFT parameters. $m = 54$ in all cases.

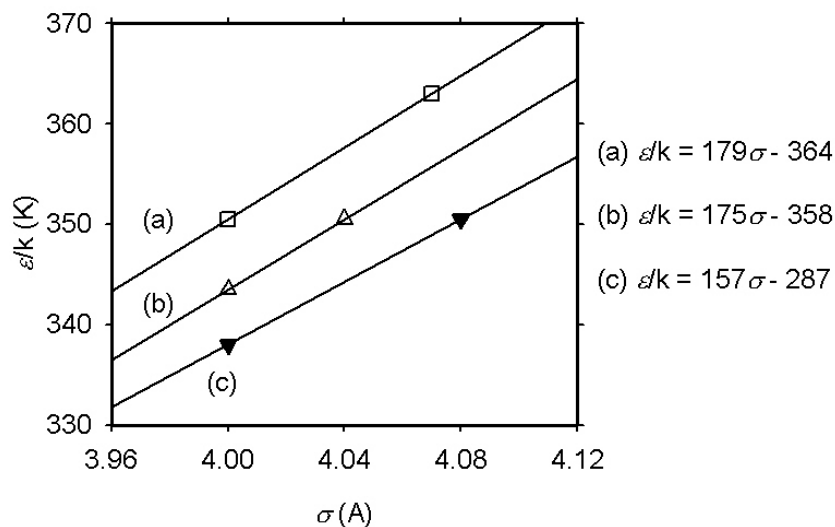


Figure 7.6 ϵ/k vs. σ for six sets of asphaltene SAFT parameters ($m = 54$ in all cases). Different sets of SAFT parameters that give similar ϕ_v^{ppt} vs. n-alkane carbon number curves are connected by lines.

To investigate whether the region in parameter space of an asphaltene's SAFT parameters can be further restricted, the asphaltene-toluene-n-heptane ternary phase diagrams (at 20°C, 1 bar) for two different asphaltenes that give similar ϕ_v^{ppt} vs. n-alkane carbon number curves are plotted in Figure 7.7. As seen in the figure, the mixture compositions at the onset of asphaltene instabilities for a 1g asphaltene per 100mL toluene mixture (the intersection of the titration line with the phase boundaries) are similar for both asphaltenes. Furthermore, the slope of the tie lines are similar for the two systems and the phase envelopes are similar away from the mixtures' plait points. Because of the similarities in the phase envelopes away from the plait points, the effects of the non-uniqueness of ϵ/k and σ for asphaltenes on asphaltene phase behavior should be small for similar mixtures away from the plait points. We should be able to further restrict the region in parameter space of an asphaltene's SAFT

parameters if asphaltene instability onset data are available for systems that originally (i.e. before any precipitant titration) had much more asphaltene dissolved in toluene. In situations where this additional information is not available, one should arbitrarily set σ to a constant value in the fitting procedure and then vary ϵ/k because a species' thermodynamic phase behavior is much more sensitive to changes in σ .

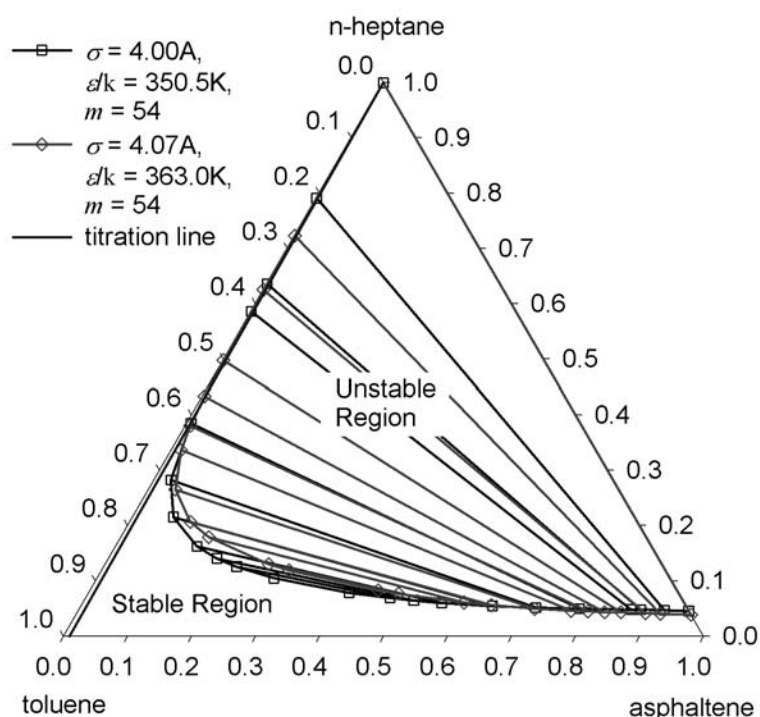


Figure 7.7 Asphaltene-toluene-n-heptane ternary phase diagram for two different asphaltenes that give similar ϕ_v^{ppt} vs. n-alkane carbon number curves at 20°C and 1 bar.

7.6 Summary

We investigated the effects of changes in SAFT parameters on the pure species' solubility parameter and molar volume. In the region of parameter

space where we expect asphaltenes to lie, the calculated solubility parameter is not sensitive to changes in m but is very sensitive to changes in the segment properties ϵ/k and σ . On the other hand, the calculated molar volume is a linear function of m and is less sensitive to changes in ϵ/k and σ .

The effect of changing the asphaltene SAFT parameters on the ϕ_v^{ppt} vs. n-alkane carbon number curve is also explored. The overall effect of changing m for asphaltenes is a translation of the asphaltene instability onset curve (on a plot of ϕ_v^{ppt} vs. n-alkane carbon number). The volume fraction of precipitants needed to induce asphaltene instability decreases with increasing m for asphaltenes. Unlike changes in m , changes in ϵ/k and σ also alter the curvature of the ϕ_v^{ppt} vs. n-alkane carbon number curve. Using different combinations of m , σ , and ϵ/k for asphaltenes, we can fit a wide range of ϕ_v^{ppt} vs. n-alkane carbon number data.

In the last section, we investigated the issue of uniqueness of the asphaltene SAFT parameters. It is shown that SAFT can fit the ambient condition ϕ_v^{ppt} (and hence the P_{RI}) data using multiple sets of ϵ/k and σ . Furthermore, different sets of ϵ/k and σ for asphaltenes that would fit the same ambient condition ϕ_v^{ppt} data are linearly related. Away from the mixture plait point, the phase envelope calculated using these different (but related) sets of asphaltene parameters are similar and we believe the effects of the non-uniqueness of ϵ/k and σ for asphaltenes on asphaltene phase behavior in oil should be small. Asphaltene instability onset data for systems containing much

more asphaltenes (where the mixture is closer to its plait point) can be used to further pin down a set of unique asphaltene parameters. In situations where this additional information is not available, one should arbitrarily set σ to a constant value in the fitting procedure.

CHAPTER 8. EFFECTS OF ASPHALTENE POLYDISPERSITY (INCLUDING RESIN ADDITION)

8.1 Introduction

The results on asphaltene stability presented thus far were calculated in SAFT by treating asphaltenes as a single, monodisperse component. As discussed in Chapter 2, asphaltenes are, in actuality, a polydisperse class of compounds with resins as their lower molecular weight sub-fraction; what is commonly termed asphaltenes in literature is a solubility cut (toluene soluble, n-pentane or n-heptane insoluble) of this distribution. As an example, Yarranton and Masliyah^[125] are able to describe the molar mass distribution (determined using plasma desorption mass spectrometry^[126]) for Athabasca bitumen using an exponential distribution. Since asphaltenes are a polydisperse class of compounds, the effects of asphaltene polydispersity need to be incorporated.

The goal of this chapter is to examine the effects of asphaltene polydispersity on its thermodynamic phase behavior in oil. One of the questions we will try to answer is whether the lowest molecular weight asphaltenes (including the resins) can stabilize, via nonpolar interactions, the higher molecular weight asphaltenes. Another question we will try to address is whether SAFT can describe the correct partitioning of the asphaltene pseudo-components between the oil and the precipitated phases at equilibrium. Since deposition

tendencies onto pipeline surfaces have often been associated with variations in the morphology and the composition of the precipitated asphaltene phase, an understanding of the molecular weight distribution of polydisperse asphaltenes in equilibrium phases will help us estimate asphaltene's deposition tendencies.

At this stage of the research, polydisperse asphaltene will be represented as four pseudo-components in SAFT: the n-C₃₋₅, the n-C₅₋₇, the n-C₇₋₁₅, and the n-C₁₅₊ n-alkane insoluble sub-fraction. The reader should keep in mind that, traditionally, the n-C₃₋₅ fraction is called resins and that conventional asphaltene extraction techniques generally identify asphaltenes as the n-C₅₊ or n-C₇₊ insoluble (and toluene/benzene soluble) fractions of heavy organics.

8.2 Selection of SAFT Parameters for Polydisperse Asphaltenes & Resins

In experiments performed by Wang^[5], the asphaltenes for Lagrave oil (the oil modeled in this chapter) were first separated into various solubility fractions using excess n-pentane, n-heptane, and n-pentadecane precipitants; these sub-fractions are called n-C₅ insoluble asphaltenes (7.5g/100mL stock-tank oil), the n-C₇ insoluble asphaltenes (6.7g/100mL oil), and the n-C₁₅ insoluble asphaltenes (5.1g/100mL oil), respectively. The asphaltene instability onsets for mixtures of asphaltenes, toluene, and n-alkanes (at ambient condition and initially with an asphaltene/toluene ratio of 1 gram per 100mL toluene) were then measured for each asphaltene fraction. The experimental asphaltene fractionation and

instability onset data that we use in this chapter to fit the SAFT model are those for Lagrave oil and are taken from Wang^[5].

The method used to obtain the SAFT parameters for polydisperse asphaltenes is similar to the monodisperse SAFT asphaltene characterization procedure given in Chapter 6. Within the SAFT model, polydisperse asphaltenes are modeled as three or four pseudo-components (depending on whether the resin fraction, which is the n-C₃₋₅ asphaltene sub-fraction, is included): an n-C₁₅₊ sub-fraction, an n-C₇₋₁₅ sub-fraction, an n-C₅₋₇ sub-fraction, and an n-C₃₋₅ sub-fraction. SAFT parameters are fit for the n-C₁₅₊ asphaltene sub-fraction to reproduce the experimental data on the minimum volume fraction precipitant needed to induce asphaltene instability (ϕ_V^{ppt}) or, equivalently, to reproduce the experimental data on the mixture refractive index at asphaltene instability onset (P_{RI}) for mixtures of n-C₁₅ insoluble asphaltene, toluene, and various n-alkanes. The asphaltenes made from the combination of n-C₁₅₊ and n-C₇₋₁₅ sub-fractions are assumed to represent the n-C₇ insoluble asphaltenes; a second set of SAFT parameters is fit for the n-C₇₋₁₅ sub-fraction to reproduce (together with the previously fitted n-C₁₅₊ sub-fraction) the experimental ϕ_V^{ppt} (or P_{RI}) data for a mixture of n-C₇ insoluble asphaltene, toluene, and n-alkane. Finally, a third set of SAFT parameters is fit to the n-C₅₋₇ sub-fraction so that the combination of the n-C₁₅₊ (previous fit), n-C₇₋₁₅ (previous fit), and n-C₅₋₇ sub-fractions represent the n-C₅ insoluble asphaltenes and will reproduce the experimental ϕ_V^{ppt} (or P_{RI}) data for a mixture of n-C₅ insoluble asphaltene, toluene, and n-alkanes. Due to lack of

precipitation data, the SAFT parameters for the resin (n-C₃₋₅) sub-fraction are obtained by decreasing the SAFT parameters (m and ϵ/k) of the n-C₅₋₇ asphaltene sub-fraction until a set of parameter is obtained that will make the resins insoluble in propane (tested at 10 bars) and soluble in n-pentane.

A flow chart of the fitting procedure is given in Figure 8.1. Note that inside the solid bracket "A", the ratio of m/MW and the n-C₁₅₊ SAFT asphaltene parameters are not changed. And inside the dashed bracket "B", the ratio of m/MW , the mass ratio of n-C₁₅₊ to n-C₇₋₁₅ asphaltenes, the n-C₁₅₊ SAFT asphaltene parameters, and the n-C₇₋₁₅ SAFT asphaltene parameters are not changed. Once a value has been assigned for the molecular weight of the n-C₁₅₊ asphaltene, the molecular weight of the other asphaltene sub-fractions depend only on the chain lengths of the pseudo-components representing those particular sub-fractions. As in the case for monodisperse asphaltenes, all binary interaction parameters between all species are set to zero. Furthermore, in light of the parameter uniqueness issues discussed in Chapter 7, the segment diameters of all asphaltene pseudo-components are set to the same value.

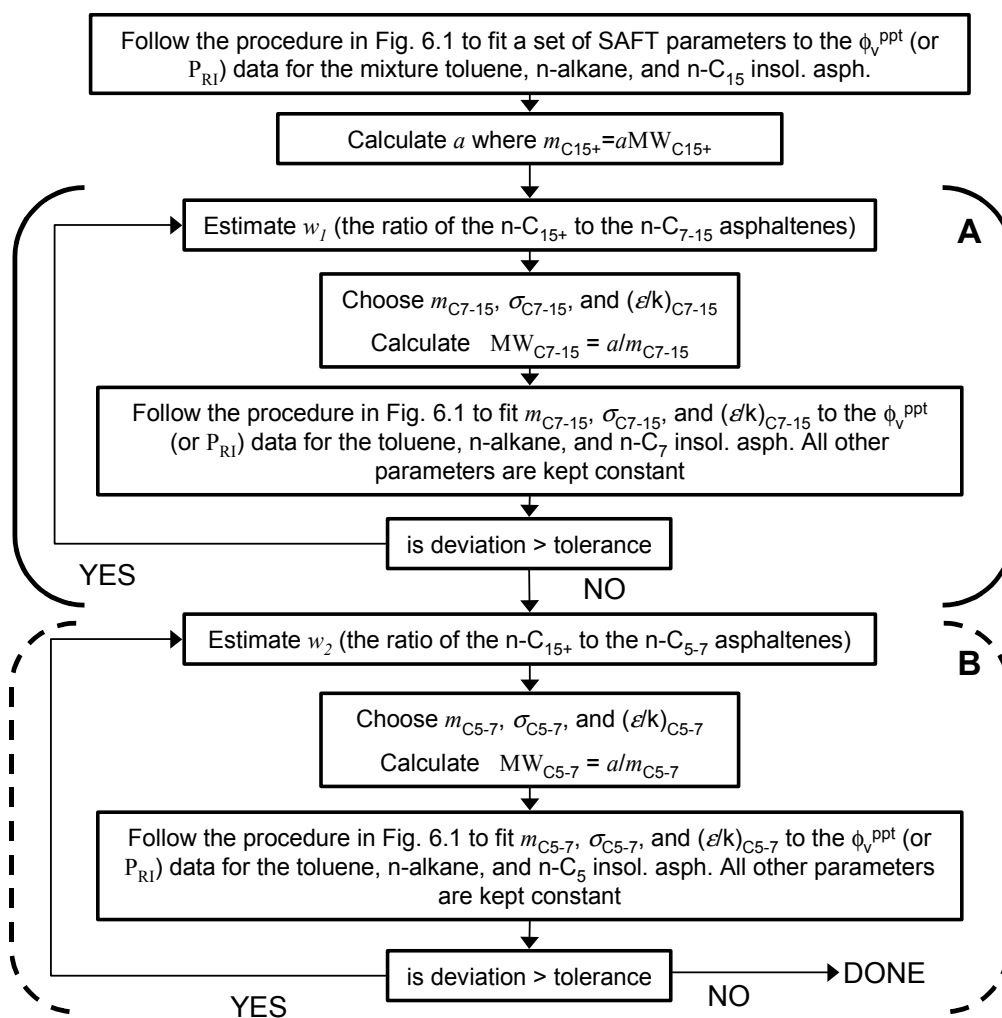


Figure 8.1 Fitting procedure for polydisperse asphaltenes with polydispersity captured using three asphaltene pseudo-components.

A comparison of the equation-of-state fitted and the experimental ϕ_V^{ppt} and P_{RI} data is shown in Figure 8.2, with the fitted SAFT asphaltene parameters listed in Table 8.1. The SAFT P_{RI} s' in Figure 8.2 were calculated using the method described in Chapter 3.4. Compared to other SAFT calculated ϕ_V^{ppt} and P_{RI} plots shown in the previous chapters, the curves in Figure 8.2 appear to be smoother because only results for the odd carbon number n-alkane precipitants are

presented. As seen in the figure, the agreement between SAFT calculated and measured ϕ_V^{ppt} (and P_{RI}) is qualitative. SAFT is able to describe the change in magnitude (and to a lesser extent, the curvature) of the ϕ_V^{ppt} vs. n-alkane carbon number curve between n-C₁₅ insoluble and n-C₅ insoluble asphaltenes. For the precipitation onsets with n-C₇ and n-C₅ extracted asphaltenes, SAFT does not accurately describe the experimental ϕ_V^{ppt} (and P_{RI}) data in cases where larger n-alkanes (undecane and higher) are used to induce asphaltene precipitation; SAFT consistently under-predicts the volume fraction of n-alkane precipitants needed to induce asphaltene instability.

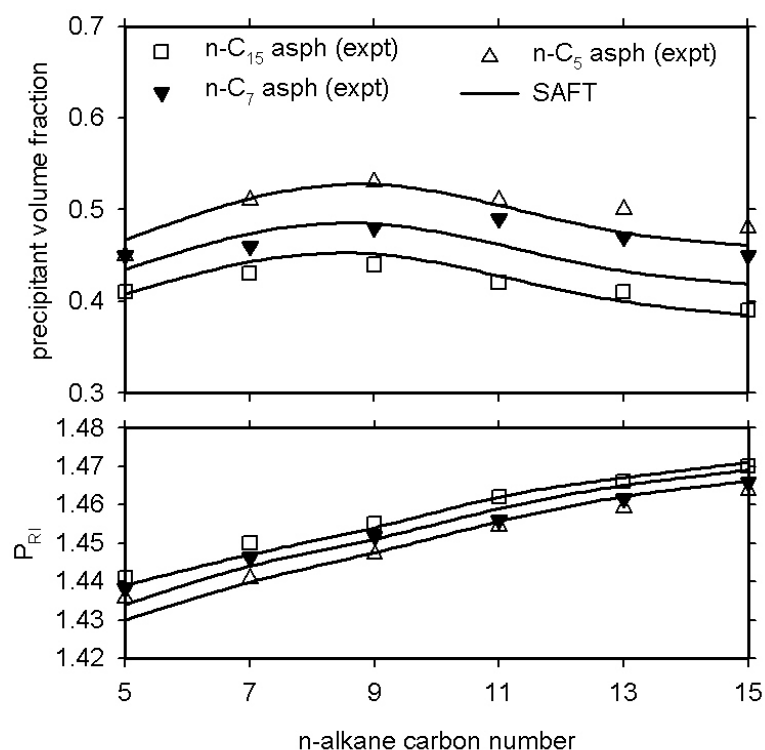


Figure 8.2 Comparison of SAFT and measured precipitant volume fraction and mixture refractive index (P_{RI}) at asphaltene instability onset for Lagrave asphaltene-toluene-n-alkane mixtures (20°C and 1 bar). The asphaltene/toluene ratio is 1g/100mL. Experimental data are from Wang^[5].

Table 8.1 SAFT parameters for the various asphaltene sub-fractions (including resins).

Asph sub-fraction	MW	SAFT Parameters				δ (MPa ^{0.5})	ρ (g/cm ³)
		M	σ (Å)	ϵ/k (K)			
n-C ₁₅₊	2500	54	4.00	350.5	22.17	1.150	
n-C ₇₋₁₅	1852	40	4.00	340.0	21.52	1.137	
n-C ₅₋₇	1806	39	4.00	335.0	21.25	1.133	
Resin	556	12	4.00	330.0	20.41	1.103	

A comparison of SAFT and measured mass distribution of the asphaltene sub-fractions is shown in Figure 8.3. For the column labeled “experimental”, the mass of each asphaltene sub-fraction was inferred from the difference in the measured amount of asphaltenes precipitated with different precipitants. Within the SAFT model, the amount of each asphaltene sub-fraction was optimized (together with the sub-fraction’s asphaltene SAFT parameters) to fit the experimental ϕ_V^{ppt} (P_{RI}) data in Figure 8.2. It is interesting to note the large discrepancy in the amount of n-C₅₋₇ asphaltene sub-fraction between experimental inferred and SAFT calculated n-C₅ extracted asphaltenes; to get a reasonable fit to experimental ϕ_V^{ppt} (P_{RI}) data, SAFT requires three times as much low molecular weight asphaltenes (n-C₅₋₇ sub-fraction) as was inferred from experiments.

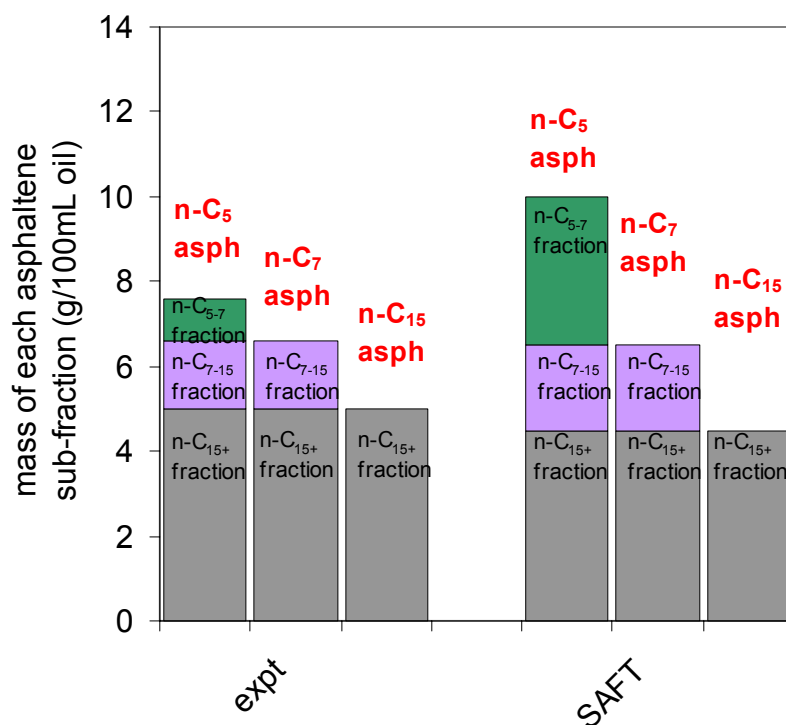


Figure 8.3 Comparison of SAFT and experimental mass distribution of each asphaltene sub-fraction in Lagrave asphaltenes. The column label above the columns identify the precipitants used to extract the asphaltenes. Experimental data are from Wang^[5].

Several factors may contribute to the poor agreement in the amount of low molecular weight asphaltenes in the asphaltene fraction shown in Figure 8.3. Experimentally, the measured amount of asphaltenes precipitated may contain not only asphaltenes that should precipitate with the precipitant used but also small amounts of entrained resins, oil, and other asphaltene fractions; variations in the amount of asphaltenes precipitated exist even for the same oil using the same extraction procedure. On the modeling side, because there are insufficient data to uniquely fit all of the model parameters for polydisperse asphaltenes, certain approximations and relationships have to be made. For instance, the

molecular weights of all SAFT asphaltene sub-fractions were set to be linearly dependent on chain length. This was done because the experimental molecular weight of each asphaltene sub-fraction is not known and because chain length has been shown to be roughly linearly dependent on molecular weight for polynuclear aromatics (see Chapter 4). The constant of proportionality ($MW=m/0.0216$) used in this work was set to give the n-C₁₅₊ asphaltene sub-fraction a molecular weight of 2,500. In another approximation, the segment diameters of all asphaltene sub-fractions were set to 4 Angstroms. The rationale behind setting the segment diameter to 4 was that for most polynuclear aromatics and polynuclear aromatics derivatives, the average value for the SAFT parameter σ is about 4.

A plot of the SAFT parameters ϵ/k vs. m for the various SAFT asphaltene fractions and resin (the n-C₃₋₅ sub-fraction) shows a well-defined trend between ϵ/k and m (Figure 8.4). The asphaltene precipitated by the lower molecular weight n-alkanes tend to be smaller in size and have lower segment energy.

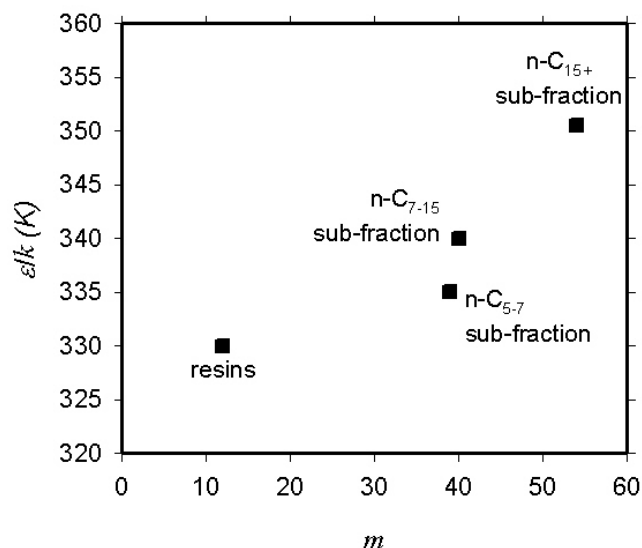


Figure 8.4 Plot of ϵ/k vs. m for the various SAFT asphaltene sub-fractions and resin.

8.3 Effects of Asphaltene Polydispersity and Resin Addition

To investigate the roles resins and asphaltene polydispersity play on asphaltene phase behavior in oil, the asphaltene solubility behavior of four model oil mixtures with monodisperse or polydisperse asphaltenes are compared. In these model systems, toluene is used as the model oil (with different amounts of n-alkane precipitants added) and the asphaltene parameters were fit to experimental ϕ_v^{ppt} data for Lagrave asphaltenes. The properties and asphaltene/resin contents of these systems are listed in Table 8.2 and are discussed in the following paragraph. We use a mixture of 7.5g asphaltenes in 100mL of toluene in these investigations because the total amount of n-pentane insoluble asphaltenes in Lagrave oil is 7.5g. All binary interaction parameters between all species used in the SAFT calculations in this section are set to zero.

The biggest difference between the various systems in Table 8.2 is that asphaltenes in Systems 1 and 2 are monodisperse, while the asphaltenes in Systems 3 and 4 are polydisperse. More specifically, the asphaltene used in Model System 1 is monodisperse and was fit to experimental $\phi_V^{\text{ppt}}(P_{\text{RI}})$ data for the n-C₁₅ insoluble Lagrave asphaltenes (also called the n-C₁₅₊ asphaltene fraction in this work). The asphaltene used in Model System 2 is monodisperse and was fit to experimental $\phi_V^{\text{ppt}}(P_{\text{RI}})$ data for the n-C₅ insoluble Lagrave asphaltenes. The asphaltene used in Model System 3 is polydisperse and the SAFT parameters for each asphaltene sub-fraction was fit to the experimental $\phi_V^{\text{ppt}}(P_{\text{RI}})$ data of the fractionated asphaltenes. Model System 4 is similar to Model System 3 with the exception that 10g of resin per 100mL oil (about 2 moles resin/100moles toluene) is added to the system. The amount of resin added (10g resin per 100mL oil) is arbitrary because the actual amount of resin in Lagrave oil is not available in literature.

Table 8.2 Oil and asphaltene properties of four representative model oils tested to study the effects of asphaltene polydispersity and resin addition.

Model System 1	
Ratio of asphaltene/toluene:	7.5 g/100mL (20°C, 1 bar)
Asphaltene type:	Monodisperse, fitted n-C ₁₅₊ asphaltene (see Table 8.1 for parameters)
Resins in system:	No
Model System 2	
Ratio of asphaltene/toluene:	7.5 g/100mL (20°C, 1 bar)
Asphaltene type:	Monodisperse, n-C ₅ asphaltene ($m = 46$; $\sigma = 4.0 \text{ \AA}$; $\epsilon/k = 350.5 \text{ K}$; $MW = 2080$; $\rho = 1.12 \text{ g/cm}^3$; $\delta = 22.13 \text{ MPa}^{0.5}$) This asphaltene was fit to experimental ϕ_v^{ppt} data for n-C ₅ insoluble Lagrave asphaltenes
Resins in system:	No
Model System 3	
Ratio of asphaltene/toluene:	7.5 g/100mL (20°C, 1 bar)
Asphaltene type:	Polydisperse with 3 sub-fractions: n-C ₁₅₊ , n-C ₇₋₁₅ , and n-C ₅₋₇ Lagrave asphaltenes (see Table 8.1 for parameters)
Mass ratio of asph fractions:	4.5 : 2.0 : 3.5 (n-C ₁₅₊ :n-C ₇₋₁₅ : n-C ₅₋₇)
Resins in system:	No
Model System 4	
Ratio of asphaltene/toluene:	7.5 g/100 mL (20°C, 1 bar)
Asphaltene type:	Polydisperse with 3 sub-fractions: n-C ₁₅₊ , n-C ₇₋₁₅ , and n-C ₅₋₇ Lagrave asphaltenes (see Table 8.1 for parameters)
Mass ratio of asph fractions:	4.5 : 2.0 : 3.5 (n-C ₁₅₊ :n-C ₇₋₁₅ : n-C ₅₋₇)
Resins in system:	Yes (see Table 1 for parameters)
Ratio of resin/toluene:	10 g/100 mL (20°C, 1 bar)

The effects of n-alkane addition on the amount of asphaltenes precipitated (at 20°C and 1 bar) for the four model oil mixtures are shown in Figures 8.5 and 8.6. For systems containing monodisperse asphaltenes (Figure 8.5), the change in asphaltene solubility is dramatic: asphaltenes go from completely soluble to almost completely insoluble in the model oil when the volume fraction of the n-alkane precipitant is increased slightly past the asphaltene instability onset point.

As expected, the lower molecular weight asphaltenes (the monodisperse asphaltene fit to the n-C₅ insoluble asphaltene ϕ_v^{ppt} data) are more soluble than the higher molecular weight asphaltene (the monodisperse, n-C₁₅ insoluble asphaltene) in terms of the amount of precipitant needed to induce asphaltene instability. When sufficiently large amount of n-alkanes are added to the model oil, all asphaltenes will precipitate.

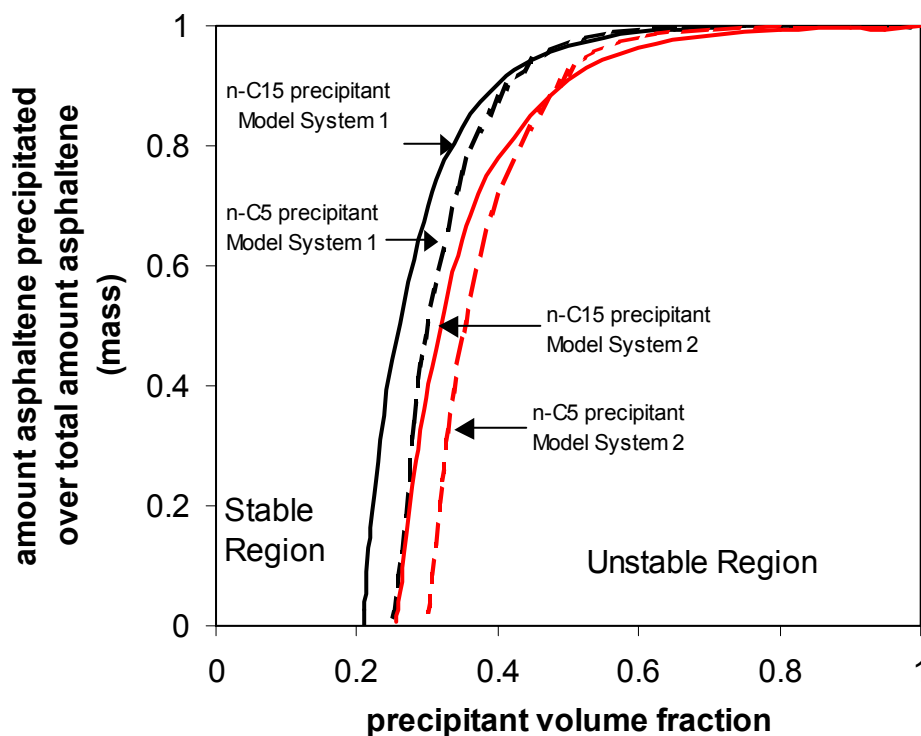


Figure 8.5 Solubility of monodisperse asphaltenes in model Lagrave oil (7.5g asphaltene/100mL toluene) mixed with n-alkanes at 20°C and 1 bar.

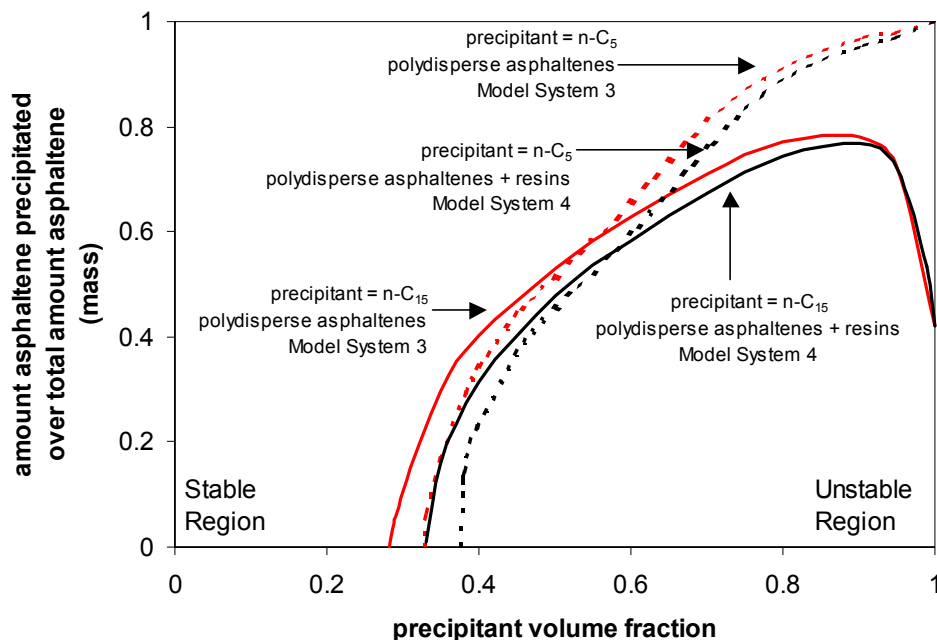


Figure 8.6 Solubility of polydisperse asphaltenes (with or without resins) in model Lagrave oil (7.5g total asphaltene/100mL toluene) mixed with n-alkanes at 20°C and 1 bar.

A large change in the amount of precipitated asphaltene vs. precipitant volume fraction can be seen when the effect of asphaltene polydispersity (and resin addition) is taken into consideration (Figure 8.6). By treating asphaltene as a polydisperse species, the amount of asphaltenes precipitated increases much more gradually with precipitant addition. A significant amount of asphaltenes will stay in solution even at high precipitant volume fractions, and more asphaltenes can be precipitated using lower molecular weight n-alkanes. It is interesting to note that when n-C₁₅ is used as the precipitant, SAFT predicts the existence of a solubility minimum around $\phi_v^{\text{ppt}}=0.9$.

A comparison of the SAFT-predicted behavior of polydisperse asphaltenes with and without resins show that the presence of resins will increase the amount of precipitant needed to induce the onset of asphaltene instability (Figure 8.6). Furthermore, at lower precipitant volume fractions in the oil, the amount of asphaltenes that will precipitate is less when resins are present. Even though only dispersion interactions are considered in our models, the lower molecular weight asphaltenes and especially resins will stabilize the heavier asphaltenes in the oil. It can be seen in Figure 8.6 that the effects of resins on asphaltene phase behavior in the oil become less pronounced as the oil becomes more dilute with precipitants.

A plot of the mass distribution of the asphaltene sub-fractions as a function of precipitant volume fraction is shown in Figure 8.7. As seen in the figure, near the initial asphaltene instability onset, the precipitated phase is composed mostly of the heaviest asphaltene fractions (in this case, the n-C15+ sub-fraction). As the amount of precipitant is increased further, more and more lower molecular weight asphaltenes will precipitate.

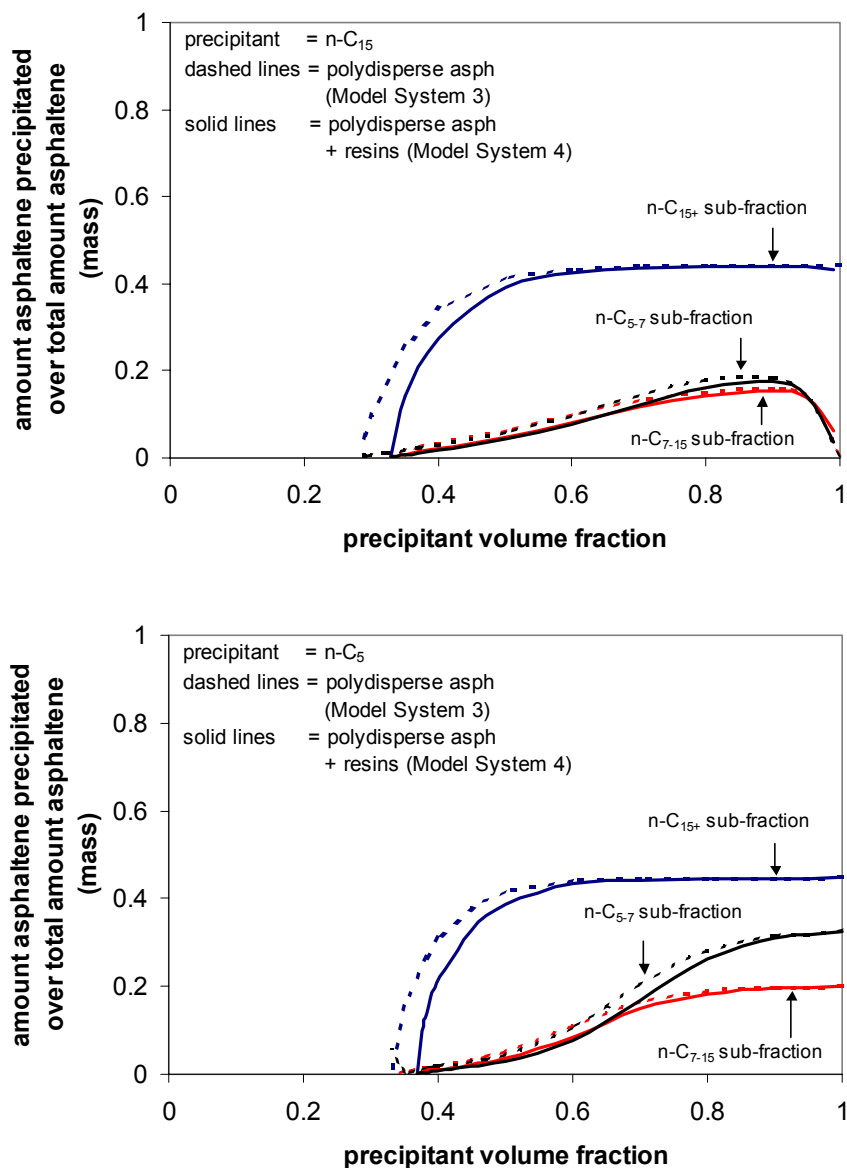


Figure 8.7 Normalized distribution of the asphaltene sub-fractions in the precipitated phase as a function of volume fraction precipitant in the model oil mixtures.

8.4 Summary

In this chapter, we investigated the effects of asphaltene polydispersity on the thermodynamic phase behavior of oil. At this stage of the research, we represented polydisperse asphaltene in SAFT with four pseudo-components: the

n-C₃₋₅ (the resins), the n-C₅₋₇, the n-C₇₋₁₅, and the n-C₁₅₊ sub-fractions. Using an extension of the monodisperse SAFT asphaltene parameter fitting procedure, we were able to assign a set of SAFT parameters to represent each of the four sub-fractions. The volume fractions of precipitants at asphaltene instability onset calculated using these parameters qualitatively agree with experimental findings.

SAFT calculations show that the lower molecular weight asphaltenes and resins play a large role in stabilizing higher molecular weight asphaltenes in oil. This is despite the inclusion of only dispersion interactions in the SAFT model. Resin's stabilizing effects on polydisperse asphaltene is greatest in the region of incipient asphaltene instability; when sufficiently large amounts of n-alkane precipitants are added, similar amounts of asphaltenes would precipitate regardless of the presence of resins in the oil. An analysis of the mass distribution of the asphaltene sub-fractions in the precipitated phase shows that the largest asphaltenes will precipitate first, followed by the precipitation of smaller asphaltenes upon further oil dilution.

CHAPTER 9. REFORMULATION OF THE SAFT DISPERSION TERM FOR POLYDISPERSITY

9.1 Introduction

Thermodynamic phase equilibria calculations for systems containing many species are computationally expensive and difficult because the number of equations that need to be solved increases with the number of species present. For example, in an iteration of the flash calculation, the chemical potential of each species in each phase must be calculated. To address this issue, Jog and Chapman^[127] proposed a reformulated cloud point algorithm that takes advantage of the form of the SAFT equation of state using the Chen and Kreglewski^[103] dispersion term. In the reformulation, the chemical potentials of the pseudo-components in a polydisperse mixture are shown to be linearly related to chain length m of the pseudo-components. Hence, computation time for systems with polydisperse species becomes independent of the number of pseudo-components in the polydisperse species. The simplification follows from the assumptions that all pseudo-components in a polydisperse species have the same segment diameter σ and have m that are linearly proportional to their molecular weight.

In this chapter, we will show that the SAFT equation of state with the dispersion contribution of Gross and Sadowski^[62] can be similarly extended to

include an arbitrary number of pseudo-components with minimal impact on computation time. Since the hard-sphere and the chain contributions are the same for SAFT with Chen & Kreglewski and SAFT with Gross & Sadowski dispersions, the reader should refer to Jog and Chapman^[127] for the hard-sphere and chain terms.

9.2 Algorithm Extension

The extension of the Gross and Sadowski^[62] dispersion contribution described below assumes that: (1) m for a pseudo-component is linear with molecular weight (i.e. $m = \alpha MW + b$ where MW is the molecular weight of a pseudo-component, and α, b are constants), (2) the segment properties (σ and ϵ/k) are the same for all pseudo-components in a polydisperse species, and (3) the binary interaction parameters k_{ij} between pseudo-components of the same polydisperse species are zero. With these assumptions, we can write, for the overall mixture

$$\bar{m} = \sum_i x_i m_i = x_p m(\overline{Mn}) + \sum_{j \rightarrow \text{solvents}} x_j m_j \quad (9.1)$$

$$\eta = \frac{\pi}{6} \rho x_p m(\overline{Mn}) d_{pp}^3 + \sum_{j \rightarrow \text{solvents}} x_j m_j d_{jj}^3 \quad (9.2)$$

where

$$x_p = \sum_{j \rightarrow \text{pseudocomp}} x_j \quad (9.3)$$

$$\overline{Mn} = \frac{\sum_{j \rightarrow \text{pseudocomp}} x_j MW_j}{x_p} \quad (9.4)$$

In the above equations, η is the packing fraction, ρ is the mixture's density, $m(\overline{Mn})$ is m for a pseudo-component with the average molecular weight \overline{Mn} , and d is the temperature-dependent segment diameter. The subscript p denotes polydisperse species and over-line bars are added to show average properties. Equations in this chapter are written with the assumption that the mixture has only one polydisperse specie (with many pseudo-components); the extension to multiple polydisperse species is straightforward.

The Gross and Sadowski dispersion contribution to the residual compressibility factor $Z^{disp,res}$ can be written as^[62]

$$Z^{disp,res} = -2\pi\rho\overline{m^2\varepsilon\sigma^3} \frac{\partial(\eta I_1)}{\partial\eta} - \pi\rho\overline{m} \left(C_1 \frac{\partial(\eta I_2)}{\partial\eta} + C_2 \eta I_2 \right) \overline{m^2\varepsilon^2\sigma^3} \quad (9.5)$$

using the notations in their work. With the assumptions listed above, Eqn. 9.5 can be simplified for systems containing polydisperse species:

$$\begin{aligned} \overline{m^2\varepsilon\sigma^3} &= \frac{\varepsilon_{pp}}{kT} \sigma_{pp}^3 x_p^2 (m(\overline{Mn}))^2 + 2m(\overline{Mn})x_p \sum_{j \rightarrow solv} x_j m_j \frac{\varepsilon_{pj}}{kT} \sigma_{pj}^3 + \\ &\sum_{i \rightarrow solv} \sum_{j \rightarrow solv} x_i x_j m_i m_j \frac{\varepsilon_{ij}}{kT} \sigma_{ij}^3 \end{aligned} \quad (9.6)$$

$$\begin{aligned} \overline{m^2\varepsilon^2\sigma^3} &= \left(\frac{\varepsilon_{pp}}{kT} \right)^2 \sigma_{pp}^3 x_p^2 (m(\overline{Mn}))^2 + 2m(\overline{Mn})x_p \sum_{j \rightarrow solv} x_j m_j \left(\frac{\varepsilon_{pj}}{kT} \right)^2 \sigma_{pj}^3 + \\ &\sum_{i \rightarrow solv} \sum_{j \rightarrow solv} x_i x_j m_i m_j \left(\frac{\varepsilon_{ij}}{kT} \right)^2 \sigma_{ij}^3 \end{aligned} \quad (9.7)$$

$$C_1 = \left[1 + \overline{m} \frac{8\eta - 2\eta^2}{(1-\eta)^4} + (1-\overline{m}) \frac{20\eta - 27\eta^2 + 12\eta^3 - 2\eta^4}{[(1-\eta)(2-\eta)]^2} \right]^{-1} \quad (9.8)$$

$$C_2 = -C_1^2 \left[\bar{m} \frac{-4\eta^2 + 20\eta + 8}{(1-\eta)^5} + (1-\bar{m}) \frac{2\eta^3 + 12\eta^2 - 48\eta + 40}{[(1-\eta)(2-\eta)]^3} \right] \quad (9.9)$$

$$I_2 = \sum_{i=0}^6 \eta^i b_i(\bar{m}) \quad (9.10)$$

$$\frac{\partial(\eta I_1)}{\partial \eta} = \sum_{j=0}^6 a_j(\bar{m})(j+1)\eta^j \quad (9.11)$$

$$\frac{\partial(\eta I_2)}{\partial \eta} = \sum_{j=0}^6 b_j(\bar{m})(j+1)\eta^j \quad (9.12)$$

$$a_j(\bar{m}) = a_{0j} + \frac{\bar{m}-1}{\bar{m}} a_{1j} + \frac{\bar{m}-1}{\bar{m}} \frac{\bar{m}-2}{\bar{m}} a_{2j} \quad (9.13)$$

$$b_j(\bar{m}) = b_{0j} + \frac{\bar{m}-1}{\bar{m}} b_{1j} + \frac{\bar{m}-1}{\bar{m}} \frac{\bar{m}-2}{\bar{m}} b_{2j} \quad (9.14)$$

In Eqns. 9.13 and 9.14, a and b are fixed constants given in Gross and Sadowski^[62]. A close look at the various contributions to Eqn. 9.5 shows that the only variables for the polydisperse component needed in the calculations are the segment properties (which are independent of the distribution of the pseudo-components), x_p , and \overline{Mn} . Hence, at a fixed temperature, the dispersion contribution to the compressibility factor can be calculated given x_p , $\{x_{solvents}\}$, \overline{Mn} , and the segment properties of all components.

The residual chemical potential for each (polydisperse or monodisperse) component in a mixture can be written as

$$\frac{\mu_k^{disp,res}(T, \nu)}{kT} = \frac{A^{disp,res}}{NkT} + Z^{disp,res} + \frac{\partial \hat{a}^{disp,res}}{\partial x_k} - \sum_{j \rightarrow \text{all species}} x_j \left(\frac{\partial \hat{a}^{disp,res}}{\partial x_j} \right) \quad (9.15)$$

where the chemical potential is for species k and the expression for $Z^{disp,res}$ is given above. The residual Helmholtz energy is

$$\frac{A^{disp,res}}{NkT} = -2\pi\rho I_1 \overline{m^2 \epsilon \sigma^3} - \rho \pi \overline{m} C_1 I_2 \overline{m^2 \epsilon^2 \sigma^3} \quad (9.16)$$

$$I_1 = \sum_{i=0}^6 a_i(\overline{m}) \eta^i \quad (9.17)$$

At a given temperature, all the terms in Eqn. 9.16 depend only on x_p , $\{x_{solvents}\}$, \overline{Mn} , and the segment properties of all components (see Eqns. 9.1, 9.2, 9.6-8, 9.10, 9.13, and 9.17 for the various contributions to $A^{disp,res}$).

The derivative $\frac{\partial \hat{a}^{disp,res}}{\partial x_k}$ for the k th species can be written as the sum of six

terms:

$$\begin{aligned} \frac{\partial \hat{a}^{disp,res}}{\partial x_k} = & -2\pi\rho \left[I_{1,xk} \overline{m^2 \epsilon \sigma^3} + I_1 \left(\overline{m^2 \epsilon \sigma^3} \right)_{,xk} \right] - \pi\rho m_k C_1 I_2 \overline{m^2 \epsilon^2 \sigma^3} - \\ & \pi\rho \overline{m} C_{1,xk} I_2 \overline{m^2 \epsilon^2 \sigma^3} - \pi\rho \overline{m} C_1 I_{2,xk} \overline{m^2 \epsilon^2 \sigma^3} - \pi\rho \overline{m} C_1 I_2 \left(\overline{m^2 \epsilon^2 \sigma^3} \right)_{,xk} \end{aligned} \quad (9.18)$$

For $k = a$ solvent component, we denote $k = s$ and the terms in Eqn. 9.18 can be simplified:

$$I_{1,xk} = \sum_{i=0}^6 a_i(\overline{m}) i \frac{\pi}{6} \rho m_s d_{ss}^3 \eta^{i-1} + \left[\frac{m_s}{\overline{m}^2} a_{1i} + \frac{m_s}{\overline{m}^2} \left(3 - \frac{4}{\overline{m}} \right) a_{2i} \right] \eta^i \quad (9.19)$$

$$\left(\overline{m^2 \epsilon \sigma^3} \right)_{,xk} = 2m_s \left[x_s m_s \sigma_{ss}^3 \frac{\epsilon_{ss}}{kT} + \frac{\epsilon_{sp}}{kT} \sigma_{sp}^3 x_p m(\overline{Mn}) \right] \quad (9.20)$$

$$C_{1,xk} = C_2 \left(\frac{\pi}{6} \rho m_s d_{ss}^3 \right) - C_1^2 \left(m_s \frac{8\eta - 2\eta^2}{(1-\eta)^4} - m_s \frac{20\eta - 27\eta^2 + 12\eta^3 - 2\eta^4}{[(1-\eta)(2-\eta)]^2} \right) \quad (9.21)$$

$$I_{2,xk} = \sum_{i=0}^6 b_i(\bar{m})i \frac{\pi}{6} \rho m_s d_{ss}^3 \eta^{i-1} + \left[\frac{m_s}{\bar{m}^2} b_{1i} + \frac{m_s}{\bar{m}^2} \left(3 - \frac{4}{\bar{m}}\right) b_{2i} \right] \eta^i \quad (9.22)$$

$$\left(\overline{m^2 \varepsilon^2 \sigma^3} \right)_{xk} = 2m_s \left[x_s m_s \sigma_{ss}^3 \left(\frac{\varepsilon_{ss}}{kT} \right)^2 + \left(\frac{\varepsilon_{sp}}{kT} \right)^2 \sigma_{sp}^3 x_p m(\overline{Mn}) \right] \quad (9.23)$$

As seen from Eqns. 9.6-10, 9.17, and 9.19-23, at a given temperature, each term in Eqn. 9.18 depends only on x_p , $\{x_{solvents}\}$, \overline{Mn} , and the segment properties (σ and ε/k) of all components. Recall that d is the temperature dependent σ given in Eqn. 4.6.

For $k =$ a pseudo-component (in the polydisperse species), we let $k = p_n$ for the n th pseudo-component and the terms in Eqn. 9.18 can be written as

$$I_{1,xk} = m_{p_n} \sum_{i=0}^6 \left(a_i(\bar{m})i \frac{\pi}{6} \rho d_{pp}^3 \eta^{i-1} + \left[\frac{a_{1i}}{\bar{m}^2} + \frac{a_{2i}}{\bar{m}^2} \left(3 - \frac{4}{\bar{m}}\right) \right] \eta^i \right) \quad (9.24)$$

$$\left(\overline{m^2 \varepsilon \sigma^3} \right)_{xk} = 2m_{p_n} \left[x_p m(\overline{Mn}) \sigma_{pp}^3 \frac{\varepsilon_{pp}}{kT} + \sum_{j \rightarrow solvents} x_j m_j \sigma_{pj}^3 \frac{\varepsilon_{pj}}{kT} \right] \quad (9.25)$$

$$C_{1,xk} = m_{p_n} \left(C_2 \frac{\pi}{6} \rho d_{pp}^3 - C_1^2 \left[\frac{8\eta - 2\eta^2}{(1-\eta)^4} - \frac{20\eta - 27\eta^2 + 12\eta^3 - 2\eta^4}{[(1-\eta)(2-\eta)]^2} \right] \right) \quad (9.26)$$

$$I_{2,xk} = m_{p_n} \sum_{i=0}^6 \left(b_i(\bar{m})i \frac{\pi}{6} \rho d_{pp}^3 \eta^{i-1} + \eta^i \left[\frac{b_{1i}}{\bar{m}^2} + \frac{b_{2i}}{\bar{m}^2} \left(3 - \frac{4}{\bar{m}}\right) \right] \right) \quad (9.27)$$

$$\left(\overline{m^2 \varepsilon^2 \sigma^3} \right)_{xk} = 2m_{p_n} \left[x_p m(\overline{Mn}) \sigma_{pp}^3 \left(\frac{\varepsilon_{pp}}{kT} \right)^2 + \sum x_j m_j \sigma_{pj}^3 \left(\frac{\varepsilon_{pj}}{kT} \right)^2 \right] \quad (9.28)$$

Hence, for each pseudo-component in a polydisperse mixture, each term in Eqn. 9.18 depends explicitly on the chain length of that pseudo-component and on x_p , $\{x_{solvents}\}$, \overline{Mn} , and the segment properties (σ and ε/k) of all components.

To recap, we have

$$\frac{\mu_k^{disp,res}(T, v)}{kT} = \frac{A^{disp,res}}{NkT} + Z^{disp,res} + \frac{\partial \hat{a}^{disp,res}}{\partial x_k} - \sum_{j \rightarrow \text{all species}} x_j \left(\frac{\partial \hat{a}^{disp,res}}{\partial x_j} \right) \quad (9.15)$$

which, for a pseudo-component in the polydisperse species, has the following dependency in each of its terms:

$$\frac{A^{disp,res}}{NkT} = \frac{A^{disp,res}}{NkT} \left(T, \rho, x_p, \{x_{solvents}\}, \overline{Mn}, \alpha, \{\sigma_{solvents}\}, \{(\mathcal{E}/k)_{solvents}\}, \sigma_p, (\mathcal{E}/k)_p \right) \quad (9.29)$$

$$Z^{disp,res} = Z^{disp,res} \left(T, \rho, x_p, \{x_{solvents}\}, \overline{Mn}, \alpha, \{\sigma_{solvents}\}, \{(\mathcal{E}/k)_{solvents}\}, \sigma_p, (\mathcal{E}/k)_p \right) \quad (9.30)$$

$$\frac{\partial \hat{a}^{disp,res}}{\partial x_k} = m_{p_n} \frac{\partial \hat{a}^{disp,res}}{\partial x_k} \quad (9.31)$$

where

$$\frac{\partial \hat{a}^{disp,res}}{\partial x_k} = \frac{\partial \hat{a}^{disp,res}}{\partial x_k} \left(T, \rho, x_p, \{x_{solvents}\}, \overline{Mn}, \alpha, \{\sigma_{solvents}\}, \{(\mathcal{E}/k)_{solvents}\}, \sigma_p, (\mathcal{E}/k)_p \right) \quad (9.32)$$

and

$$\sum_{j \rightarrow \text{all species}} x_j \left(\frac{\partial \hat{a}^{disp,res}}{\partial x_j} \right) = \left[\sum_{j \rightarrow \text{solvents}} x_j \left(\frac{\partial \hat{a}^{disp,res}}{\partial x_j} \right) \right] + \left(\frac{\partial \hat{a}^{disp,res}}{\partial x_p} \right) x_p m(\overline{Mn}) \quad (9.33)$$

In Eqn. 9.33, the terms in the summation over all solvents all depend only on $(T, \rho, x_p, \{x_{solvents}\}, \overline{Mn}, \alpha, \{\sigma_{solvents}\}, \{(\mathcal{E}/k)_{solvents}\}, \sigma_p, (\mathcal{E}/k)_p)$. Furthermore, the derivative in the second term of the right hand side of Eqn. 9.33 is constant for all pseudo-components and also depend only on $(T, \rho, x_p, \{x_{solvents}\}, \overline{Mn}, \alpha, \{\sigma_{solvents}\}, \{(\mathcal{E}/k)_{solvents}\}, \sigma_p, (\mathcal{E}/k)_p)$.

For a solvent (a monodisperse species), the residual chemical potential has the following dependency in each of its terms:

$$\frac{A^{disp,res}}{NkT} = \frac{A^{disp,res}}{NkT} \left(T, \rho, x_p, \{x_{solvents}\}, \overline{Mn}, \alpha, \{\sigma_{solvents}\}, \{(\epsilon/k)_{solvents}\}, \sigma_p, (\epsilon/k)_p \right) \quad (9.34)$$

$$Z^{disp,res} = Z^{disp,res} \left(T, \rho, x_p, \{x_{solvents}\}, \overline{Mn}, \alpha, \{\sigma_{solvents}\}, \{(\epsilon/k)_{solvents}\}, \sigma_p, (\epsilon/k)_p \right) \quad (9.35)$$

$$\frac{\partial \hat{a}^{disp,res}}{\partial x_k} = \frac{\partial \hat{a}^{disp,res}}{\partial x_k} \left(T, \rho, x_p, \{x_{solvents}\}, \overline{Mn}, \alpha, \{\sigma_{solvents}\}, \{(\epsilon/k)_{solvents}\}, \sigma_p, (\epsilon/k)_p \right) \quad (9.36)$$

$$\sum_{j \rightarrow \text{all species}} x_j \left(\frac{\partial \hat{a}^{disp,res}}{\partial x_j} \right) = \left[\sum_{j \rightarrow \text{solvents}} x_j \left(\frac{\partial \hat{a}^{disp,res}}{\partial x_j} \right) \right] + \left(\frac{\partial \hat{a}^{disp,res}}{\partial x_p} \right) x_p m(\overline{Mn}) \quad (9.33)$$

The dependencies of the various terms in Eqn. 9.33 has been described above.

Finally, if we are to lump the various terms together, we get

$$\frac{\mu_k^{disp,res}}{kT} = W_A + W_B \quad \text{for } k = \text{solvents} \quad (9.34)$$

and
$$\frac{\mu_k^{disp,res}}{kT} = W_A + m_k W_c \quad \text{for } k = \text{pseudo-components} \quad (9.34')$$

where the W 's are function only of $(T, \rho, x_p, \{x_{solvents}\}, \overline{Mn}, \alpha, \{\sigma_{solvents}\}, \{(\epsilon/k)_{solvents}\}, \sigma_p, (\epsilon/k)_p)$. Jog and Chapman^[127] showed similar dependencies in the chain and hard-sphere contributions to the chemical potential:

$$\frac{\mu_k^{hs,res}}{kT} = W_D \quad \text{for } k = \text{solvent}$$

$$\frac{\mu_k^{hs,res}}{kT} = m_k W_E \quad \text{for } k = \text{pseudo-components}$$

and

$$\frac{\mu_k^{chain,res}}{kT} = W_F \quad \text{for } k = \text{solvent}$$

$$\frac{\mu_k^{chain,res}}{kT} = W_G + m_k W_H \quad \text{for } k = \text{pseudo-components}$$

Since Eqns. 9.34 and 9.34' have the same functional form as the dispersion term in Jog and Chapman^[127], the cloud point curve acceleration algorithm proposed in their work can be applied here. Furthermore, since the residual chemical potential for the pseudo-components in each polydisperse species is a linear function of chain length m_i , the natural logarithm of the partition coefficient K_i for the i th pseudo-component (see Chapter 4) is also a linear function of m_i . Hence, only two parameters need to be solved for each polydisperse species (having an arbitrary number of pseudo-components) in the flash calculations.

CHAPTER 10. MODIFICATIONS TO THE SAFT ASSOCIATION TERM – IMPLICATIONS TO MIXTURES CONTAINING WATER

10.1 Introduction

The main focus of our investigation so far has been on mixtures dominated by molecular size and van der Waals interactions. For these systems, the local fluid structures are dominated by the species' repulsive interactions and to a lesser degree by nonpolar interactions. However, for mixtures containing associating species such as water, intermolecular attraction (due to hydrogen bonding) plays a larger role in determining the structure of the fluid. These attraction forces are highly orientation dependent and will constrain the orientations of the interacting molecules.

Of all the mixtures containing associating species, we are especially interested in modeling the thermodynamic phase behavior of water-hydrocarbon mixtures. We are interested in this system because (1) it is of considerable importance in refining and petrochemical operations; (2) it is important in the treatment of industrial waste water and in other environmental engineering operations; (3) considerable amounts of water are present in some oil and gas reservoirs whose presence may affect the phase behavior of other reservoir components; and (4) at its present state, SAFT cannot describe the solubility of hydrocarbon in a water-rich phase^[128,129].

Water-hydrocarbon mixtures are difficult to model because of the unique properties of water due to its strong hydrogen bonding tendencies. For instance, the solubility of water in hydrocarbon is orders of magnitude larger than the solubility of hydrocarbon in water. Furthermore, there is a minimum solubility of hydrocarbons in water (as a function of temperature) while water solubility in hydrocarbon is a monotonic function of temperature.^[129-133] The extremely nonideal behaviors in these systems are due to extensive cooperative bonding of water (which forms a space-filling, open network^[134]) in the water-rich phase. Thus, to be able to model the phase behavior of water-hydrocarbon systems, an equation of state must be able to take into account the considerable degree of long range order (due to hydrogen bonding) in the water-rich phase. This long range structural order in water is responsible for such unique properties as the density maximum of water (0.999972 g/cm^3 at 3.98°C and atmospheric pressure) and the isothermal compressibility minimum near 46.5°C and atmospheric pressure.^[135]

Traditionally, the phase behavior of mixtures containing water are modeled using either an excess Gibbs energy model such as the Wilson equations^[24] or a cubic equation of state model with modifications to include the energy effects due to hydrogen bonding^[136,137]. The main advantage of the excess Gibbs energy models is their ability to represent experimental data with simple empirical equations. These models are not predictive because they are

empirical in nature and the equations work well only within a range of temperatures and pressures. The cubic equation of state models rely on elaborate mixing rules (such as the local composition mixing rule of Huron and Vidal^[138]) or large binary interaction parameters with questionable predictive capabilities. For instance, Economou, *et al.*^[130] showed that while the Peng-Robinson equations with the Huron-Vidal mixing rule provided qualitative improvement over the van der Waals mixing rule in modeling 1-hexene solubility in water, its prediction for water in 1-hexene became worse. Because of the low solubility of hydrocarbons in water, experimental phase equilibrium data are often described in terms of Henry's constants and it is common to recast theory calculations in terms of theory-calculated Henry's constants.

In the last decade, theories based on Wertheim's TPT1 theory^[56-59] (namely SAFT) have been used to model systems containing water. For instance, Economou and Tsonopoulos^[139] found that while SAFT adequately describes the solubility of water in various hydrocarbons, the equation of state fails to describe the solubility of hydrocarbons in water. This is true regardless of whether a 3-site or 4-site model is used to describe water in SAFT. The results of this and other similar studies^[128,129,139,140] are surprising. Truskett, *et al.*^[141] attributed this in part to the theory's inability to reproduce the distinguishing thermodynamic features of liquid water (such as its density maxima), which are indications that SAFT cannot adequately describe the long range cooperative bonding behavior of liquid water. In the following section, we will discuss some

potential reasons for SAFT's shortcomings and introduce a more rigorous form of the equation of state that explicitly accounts for the longer-range interactions in the hydrogen bonding term.

10.2 Theory Modifications

The association contribution to the Helmholtz energy (A^{assoc}) for a pure fluid with multiple bonding sites can be written as^[55]

$$\frac{A^{assoc}}{RT} = \sum_A \left(\ln X^A - \frac{X^A}{2} \right) + \frac{M}{2} \quad (10.1)$$

from Wertheim's first order perturbation theory^[56-59] where M is the number of association sites on each molecule, X^A is the mole fraction of molecules not bonded at site A , R is the gas constant, and T is temperature. The other terms in the Helmholtz energy expression can be found in Chapter 4. X^A is calculated from the recursive relationship

$$X^A = [1 + \sum_B \rho X^B \Delta^{AB}]^{-1} \quad (10.2)$$

where
$$\Delta^{AB} = \int g_R(12) f^{AB}(12) d(12) \quad (10.3)$$

$$= 4\pi \int_{\sigma}^{r_c} g_R(r) r^2 \frac{\iint f^{AB}(12) d\omega_1 d\omega_2}{\iint d\omega_1 d\omega_2} dr$$

and
$$f^{AB} = \exp(-\phi^{AB}(r_{AB})/kT) - 1 \quad (10.4)$$

In Eqn. 10.2, ρ is the number density of molecules and the summation is over all sites B . In Eqn. 10.2 to 10.4, Δ^{AB} is the strength of association, f^{AB} is the Mayer f -function, $g_R(12)$ is the reference fluid pair correlation function,

$$d(12) = \frac{4\pi r^2 d\omega_1 d\omega_2 dr}{\iint d\omega_1 d\omega_2} \text{ where } \omega \text{ denotes the orientation contributions, and } \phi^{AB} \text{ is}$$

the intermolecular potential between molecules A and B . $d(12)$ is an unweighted angle average of the orientations. The pair correlation function (also called the radial distribution function) is a factor that multiplies the bulk density of the fluid to give the local fluid density about some fixed molecule. The integral in Eqn. 10.3 is taken from the surface of the molecule to a cutoff distance r_c and the equation requires the radial distribution of the reference fluid in the range where bonding occurs. The free energy relationship (Eqns. 10.1 to 10.4) is exact within the first order molecular framework described by Wertheim. The assumptions and limitations of the first order perturbation theory are given in Chapter 4.

If one assumes that the reference fluid consists of hard spheres (with a spherical diameter of σ) and that the site-site intermolecular interaction has the form given in Figure 10.1, then the integral in Eqn. 10.3 can be simplified and renormalized:[142]

$$\Delta^{AB} = K\sigma^3 F^{AB} \int_1^{r^*} r^2 g_{hs}(r) dr \quad (10.5)$$

$$\text{where } K = 4\pi \frac{(1 - \cos\theta_c)^2}{4} \quad (10.6)$$

$$\text{and } F^{AB} = \exp(\epsilon^{AB} / kT) - 1 \quad (10.7)$$

In Eqn. 10.6, θ_c is the angle cutoff of the associating “cone” (see Fig. 10.1). The form of the SAFT association term used in literature is the result of an additional

simplification made by Chapman, *et al.*[55]; they assumed that $r^2 g_{ref} \approx \text{constant}$ since association is effective only in a small region near the molecular surface so that

$$\Delta \approx \kappa F^{AB} g_{ref}(\sigma) \quad (10.8)$$

The volume parameter κ and energy parameter ϵ^{AB} can be determined by fits to the fluid's liquid densities and vapor pressures.

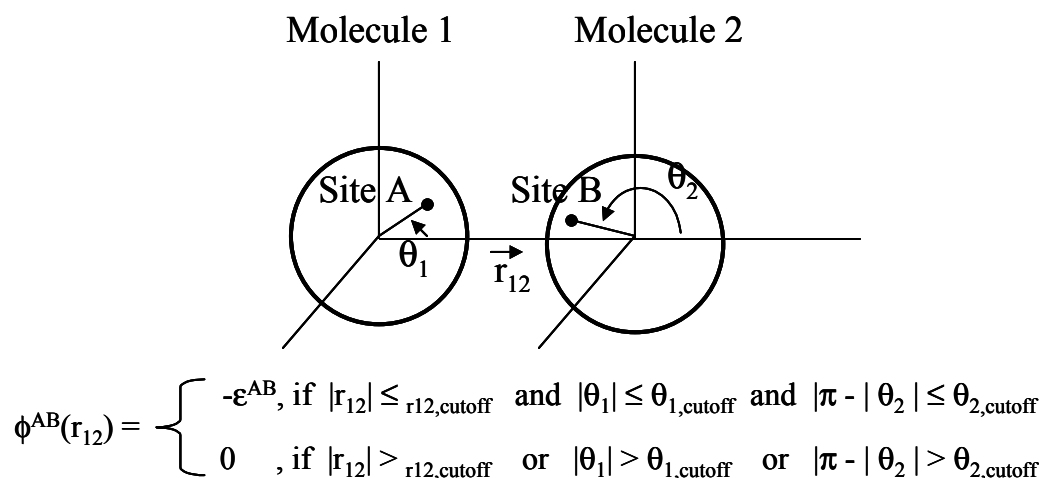


Figure 10.1 Intermolecular potential model for molecules with square-well sites with angular cutoff. The figure is reproduced from Jackson, *et al.*[142]

The idea of treating water as hard spheres with multiple bonding sites (similar to that shown in Figure 10.1) is similar to the simple point charge (SPC) model for water used in literature. In the SPC models, water is treated as a Lennard-Jones sphere located on the oxygen atom with two positive partial charges and one or two negative charges. As shown in Figure 10.2, the hard spheres + association model for water used in this study can qualitatively

describe the radial distribution of bulk water. The experimental data in Figure 10.2 were obtained at 25°C by Soper and Phillips^[143] for the oxygen-oxygen distribution. The simulation was run using 864 hard spheres with 4 bonding sites per molecule for 100 million configurations. Each molecule has a bonding ϵ of 6, a θ_{cutoff} of 27°, a hard sphere diameter of 2.55 Angstrom, and a reduced density of 0.555 (equivalent to 1 g/cm³ with the aforementioned σ). The van der Waals diameter of water molecule was found to be between 2.8 and 3.9 Angstroms, depending on orientation.^[134]

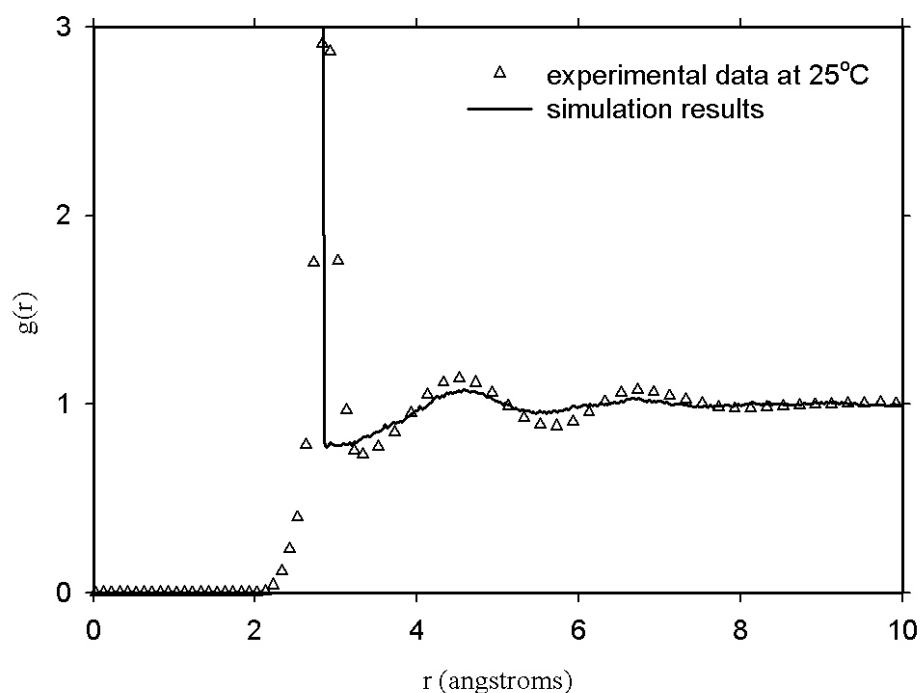


Figure 10.2 The hard spheres + association model of water used in this work can qualitatively describe the local structure of bulk water.

To improve the equation of state's ability to model strongly associating fluids such as water, we can (1) apply Wertheim's second order perturbation

theory^[144] and/or (2) remove the assumptions used to obtain Eqn. 10.8 and use the expression for Δ^{AB} in Eqn. 10.5 instead. Although calculations made with the second order theory show better agreement with simulation results, the improvements made in going from first to second order theory is small. ^[142] Furthermore, the inclusion of the second order terms would require analytic expressions for the triplet correlation functions that are much more complex than the expressions for the pair correlations. This will become apparent in the next few paragraphs. Thus we will concentrate our effort on the second approach. By considering the fluid structure over a large distance in the calculation of the strength of association between two potential bonding sites, we should be able to capture the long range bonding behavior of liquid water.

To use Eqn. 10.5 to calculate the strength of association between two bonding sites, we need an analytic expression for $g(r)$ of the reference hard sphere fluid. While $g(r)$ can be tabulated in computer simulations, its exact solution cannot be determined analytically. An approximation to $g(r)$ for hard spheres was solved by Wertheim^[145] and Thiele^[146] using Percus-Yevick (PY) equation. (The solution is exact in the PY framework.) Succinctly, they applied the PY equation

$$c(r) = g(r) - y(r) \quad (10.9)$$

$$\text{where} \quad y(r) \equiv \exp(\phi(r)/kT)g(r) \quad (10.10)$$

to the Ornstein-Zernike (OZ) integral equation to “close” the OZ equation:

$$h(r_{12}) = c(r_{12}) + \rho \int c(r_{13})h(r_{23})dr_3 \quad (10.11)$$

In the above equations, $c(r)$, $y(r)$, and $h(r)$ are the direct, the cavity, and the total correlation function, respectively. The OZ equation essentially says that the total correlation between two molecules is the sum of a direct contribution and an indirect contribution that depends on all other molecules. Note that the solution to the PY equations is exact but the integral equation theory is only approximate.

The solution to $g(r)$ given by Wertheim and Thiele is difficult to use because the radial distribution function is given in terms of its Laplace transforms and the function itself contains imaginary terms. Using Baxter's factorization method^[147], Chang and Sandler^[148] parameterized these expressions in terms of real functions. We will use the form given by Chang and Sandler but limit the range of integration to within 2σ because of the presence of poles at integral multiples of σ (i.e. at $\sigma, 2\sigma, 3\sigma \dots$). This cutoff distance is about 6.3 Angstroms in terms of SPC water diameter (Figure 10.2).

Comparison between computer simulations and the solution to $g(r)$ given by Wertheim and Thiele shows that the latter suffers from three defects at higher fluid densities.^[149] These are: (1) the pair correlation function is too small near the core ($r \rightarrow \sigma$), (2) the pair correlation function oscillates slightly out of phase with respect to simulation results, and (3) the main maximum is too high compared to simulation results. We will use an empirical shifting algorithm proposed by Verlet and Weis^[149] to "correct" for these defects in the Wertheim-Thiele solutions (Figure 10.3). If we denote $g(r/\sigma, \eta)$ as the true pair correlation

function and $g_{wt}(r/\sigma, \eta)$ as the pair correlation function calculated using the Wertheim-Thiele solution, then

$$g(r/\sigma, \eta) = g_{wt}(r/\sigma_{wt}, \eta_{wt}) + \delta g_1(r) \quad (10.12)$$

where
$$\eta_{wt} = \eta - \frac{1}{16}\eta^2 \quad (10.13)$$

$$\delta g_1(r) = (A/r) \exp[-\mu(r - \sigma)] \cos \mu(r - \sigma) \quad (10.14)$$

$$\frac{A}{\sigma} = \frac{3 \eta_{wt}^2 (1 - 0.7117\eta_{wt} - 0.114\eta_{wt}^2)}{4 (1 - \eta_{wt})^4} \quad (10.15)$$

and
$$\mu\sigma = \frac{24(A/\sigma)}{\eta_{wt} g_{wt}(1, \eta_{wt})} \quad (10.16)$$

As seen in Figure 10.3, the Verlet-Weis correction agrees very well with simulation data.

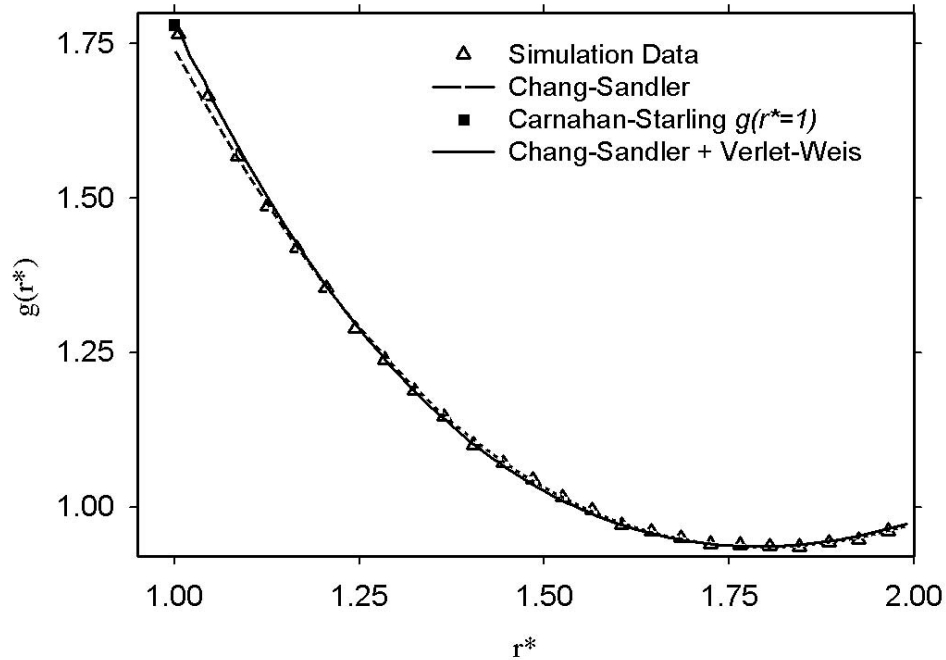


Figure 10.3 Comparison of the pair correlation functions obtained from different methods at a reduced density of 0.39 ($\eta = 0.2042$). r^* is the reduced distance. The simulation was run for 4 million configurations with 256 molecules.

Using the Chang and Sandler parameterization with the Verlet-Weis shift, the integral in Eqn. 10.5 becomes

$$\int_{\sigma}^{r_c} r^2 g_{ref}(r) dr = \sigma^3 (A^{**} + B^{**}) \quad (10.17)$$

where

$$B^{**} = \left(\frac{A}{\sigma} \right) \left[\frac{1}{2C} + e^{C(1-\frac{r}{\sigma})} \left(\frac{1}{2} \left(C \frac{r_c}{\sigma} + 1 \right) \sin \left(C \left(\frac{r_c}{\sigma} - 1 \right) \right) - \frac{r_c}{\sigma} \frac{1}{2C} \cos \left(C \left(\frac{r_c}{\sigma} - 1 \right) \right) \right) \right]$$

$\frac{A}{\sigma}$ is given in Eqn. 10.15

$$C = \frac{24(A/\sigma)}{\eta_{wt} g_{wt}(1, \eta_{wt})}$$

η_{wt} is given in Eqn. 10.13

$$g_{wt}(1, \eta_{wt}) = \frac{-(1+2\eta_{wt})^2}{(1-\eta_{wt})^4} + \frac{6\eta_{wt}(1+\eta_{wt}/2)^2}{(1-\eta_{wt})^4} - \frac{\eta_{wt}(1+2\eta_{wt})^2}{2(1-\eta_{wt})^4}$$

and where

$$A^{**} = I_1 + I_2 + I_3$$

$$I_1 = \frac{a_1 e^{-A}}{A^2 (\eta/\eta_{wt})^{2/3}} \left[e^{A(\eta/\eta_{wt})^{1/3} (r_c/\sigma)} \left(A \left(\frac{\eta}{\eta_w} \right)^{1/3} \left(\frac{r_c}{\sigma} \right) - 1 \right) - e^{A(\eta/\eta_{wt})^{1/3}} \left(A \left(\frac{\eta}{\eta_w} \right)^{1/3} - 1 \right) \right]$$

$$I_2 = a_2 e^{-B} \left[e^{B(\eta/\eta_{wt})^{1/3} (r_c/\sigma)} \left[\left(B^3 \left(\frac{\eta}{\eta_w} \right)^{1/3} \left(\frac{r_c}{\sigma} \right) - B^2 + BC^2 \left(\frac{\eta}{\eta_w} \right)^{1/3} \left(\frac{r_c}{\sigma} \right) + C^2 \right) \cos \left(C \left(\left(\frac{\eta}{\eta_w} \right)^{1/3} \left(\frac{r_c}{\sigma} \right) - 1 \right) \right) \right. \right. \\ \left. \left. + C \left(B^2 \left(\frac{\eta}{\eta_{wt}} \right)^{1/3} \left(\frac{r_c}{\sigma} \right) - 2B + C^2 \left(\frac{\eta}{\eta_{wt}} \right)^{1/3} \left(\frac{r_c}{\sigma} \right) \right) \sin \left(C \left(\left(\frac{\eta}{\eta_w} \right)^{1/3} \left(\frac{r_c}{\sigma} \right) - 1 \right) \right) \right] \\ - e^{B(\eta/\eta_{wt})^{1/3}} \left[\left(B^3 \left(\frac{\eta}{\eta_{wt}} \right)^{1/3} - B^2 + BC^2 \left(\frac{\eta}{\eta_{wt}} \right)^{1/3} + C^2 \right) \cos \left(C \left(\left(\frac{\eta}{\eta_{wt}} \right)^{1/3} - 1 \right) \right) \right. \\ \left. \left. + C \left(B^2 \left(\frac{\eta}{\eta_{wt}} \right)^{1/3} - 2B + C^2 \left(\frac{\eta}{\eta_{wt}} \right)^{1/3} \right) \sin \left(C \left(\left(\frac{\eta}{\eta_{wt}} \right)^{1/3} - 1 \right) \right) \right] \right] / \left[\left(\frac{\eta}{\eta_{wt}} \right)^{2/3} (B^2 + C^2)^2 \right]$$

$$I_3 = a_3 e^{-B} \left[e^{B(\eta/\eta_{wt})^{1/3}} \left[C \left(B^2 \left(\frac{\eta}{\eta_{wt}} \right)^{1/3} - 2B + C^2 \left(\frac{\eta}{\eta_{wt}} \right)^{1/3} \right) \cos \left(C \left(\left(\frac{\eta}{\eta_{wt}} \right)^{1/3} - 1 \right) \right) \right. \right. \\ \left. \left. - \sin \left(C \left(\left(\frac{\eta}{\eta_{wt}} \right)^{1/3} - 1 \right) \right) \left(B^3 \left(\frac{\eta}{\eta_{wt}} \right)^{1/3} - B^2 + BC^2 \left(\frac{\eta}{\eta_{wt}} \right) + C^2 \right) \right] \\ + e^{B(\eta/\eta_{wt})^{1/3} (r_c/\sigma)} \left[\left(B^3 \left(\frac{\eta}{\eta_{wt}} \right)^{1/3} \left(\frac{r_c}{\sigma} \right) - B^2 + BC^2 \left(\frac{\eta}{\eta_{wt}} \right) \left(\frac{r_c}{\sigma} \right) + C^2 \right) \sin \left(C \left(\left(\frac{\eta}{\eta_{wt}} \right)^{1/3} \left(\frac{r_c}{\sigma} \right) - 1 \right) \right) \right]$$

$$-C \cos\left(C\left(\frac{\eta}{\eta_{wt}}\right)^{1/3}\left(\frac{r_c}{\sigma}\right)-1\right)\left(B^2\left(\frac{\eta}{\eta_{wt}}\right)^{1/3}\left(\frac{r_c}{\sigma}\right)-2B+C^2\left(\frac{\eta}{\eta_{wt}}\right)^{1/3}\left(\frac{r_c}{\sigma}\right)\right)\left/\left[\left(\frac{\eta}{\eta_{wt}}\right)^{2/3}(B^2+C^2)^2\right]\right]$$

The variables used in I_1 , I_2 , and I_3 are

$$A = \frac{-2\eta_w + Z_d}{1 - \eta_w}$$

$$B = \frac{-2\eta_w - Z_d / 2}{1 - \eta_w}$$

$$C = \frac{Z_s \sqrt{3}}{2(1 - \eta_{wt})}$$

$$Z_d = y_+ - y_-$$

$$Z_s = y_+ + y_-$$

$$y_{\pm} = (2\eta f)^{1/3} \left[\left(\frac{2\eta^4}{f^2} + 1 \right)^{1/2} \pm 1 \right]^{1/3}$$

$$f = 3 + 3\eta_{wt} - \eta_{wt}^2$$

$$a_1 = \frac{-2\eta_{wt}(1 - \eta_{wt} - 3\eta_{wt}^2) + (1 - 3\eta_{wt} - 4\eta_{wt}^2)Z_d + (1 + \eta_{wt}/2)Z_d^2}{3(2\eta_{wt}^2 + Z_d^2)(1 - \eta_{wt})^2}$$

$$a_2 = \frac{\eta(2 + 4\eta_{wt} - 3\eta_{wt}^2) - (1 - 3\eta_{wt} - 4\eta_{wt}^2)Z_d + 2(1 + \eta_{wt}/2)Z_d^2}{3(2\eta_{wt}^2 + Z_d^2)(1 - \eta_{wt})^2}$$

$$a_3 = \frac{(1 - 3\eta_{wt} - 4\eta_{wt}^2)(4\eta_{wt}^2 + Z_d^2) + \eta_{wt}(2 - 5\eta_{wt}^2)Z_d}{Z_s(2\eta_{wt}^2 + Z_d^2)(1 - \eta_{wt})^2 \sqrt{3}}$$

The variables (r_c/σ) and θ_c , which is the dimensionless cutoff distance and the cutoff angle, can be determined from fits to saturated vapor pressures and liquid

densities of water. The various derivatives of Δ^{AB} such as $(\partial\Delta/\partial\rho)_{T,N}$ can be determined numerically.

CHAPTER 11. CONCLUSIONS AND FUTURE RESEARCH

The main focus of this research is to develop an equation of state model that can describe and predict the phase behavior of asphaltenes in crude oil under both ambient and reservoir conditions. The hypothesis underlying this work is that molecular size and nonpolar van der Waals interactions dominate asphaltene phase behavior in reservoir fluids. We chose the SAFT equation of state (with the inclusion of only van der Waals interactions) as our starting point because of its theoretical basis and its ability to model systems dominated by large differences in molecular size. Along the way, a robust and efficient stability-flash algorithm was developed (Chapter 4) to calculate equilibrium phase compositions for systems of interest in this work (namely multi-component systems with large differences in molecular properties and/or composition).

To trace out the asphaltene stability boundary under reservoir conditions for comparison with SAFT predictions, the asphaltene stability and bubble point curves of a recombined oil (stock-tank oil with separator gas added back in) and a model live oil (asphaltene-toluene-methane mixture) were measured as functions of pressure, temperature, and dissolved gas concentration (Chapter 3). Significant temperature effects on asphaltene stability were observed, and increasing the temperature of the system seemed to improve asphaltene stability. Furthermore, at each temperature, the asphaltene instability onset pressures were nearly linear functions of mixture gas concentration. This suggested that

the asphaltene instability boundaries could be roughly estimated from a few data points. Finally, an analysis of the experimental data showed that at a constant temperature, the mixture refractive indices do not change much along the asphaltene instability onset curves.

To investigate the applicability of the SAFT equation of state for use in asphaltene phase behavior modeling, SAFT's ability to describe the thermodynamic phase behavior of a variety of model systems were tested (Chapter 5). In the first set of investigation, we tested SAFT's ability to describe the phase behavior of long-chain short-chain alkane mixtures. We were interested in this system because the bulk of crude oil is made up of saturates components and because these mixtures will test SAFT's ability to model the effects of size on solubility. In spite of its deficiencies in modeling of the critical region, SAFT was clearly the better equation of state for predicting the phase behavior of highly asymmetric mixtures of alkanes compared to conventional cubic equations. Using a binary interaction parameter of 0, SAFT provided good estimates of liquid phase compositions up to within 5-10 bars of the predicted mixture critical points. This meant that good predictions of crude oil thermodynamic properties should be possible using SAFT with binary interaction parameters set to 0 between all alkanes in oil (with the exception of the lighter fractions).

In the second set of model system investigations, we tested SAFT's ability to describe the phase behavior of polystyrene-hexane and polystyrene-toluene-ethane. The system polystyrene-toluene-ethane was particularly interesting because it resembled our model live oil system (asphaltene-toluene-methane). Comparison between theory and experiments showed that SAFT was capable of describing and predicting the phase behavior of these binary and ternary systems (which consisted of species with very large size disparities); the effects of pressure, temperature, and composition changes on phase stability were accurately described using SAFT. Furthermore, by comparing the phase behavior of asphaltenes with that of polystyrene, we could explain many asphaltene behaviors in the framework of polymer thermodynamics (such as the L/UCST behavior).

In the last set of model system investigations, we looked at the phase behavior (solid-liquid-vapor equilibria) of phenanthrene-methane-decane mixture. This system was of significant interest because phenanthrene shares structural similarities with asphaltene and this system would provide insights into SAFT's ability to describe the solubility behavior of polynuclear aromatics. An analysis showed that SAFT (together with a solid fugacity model) was able to describe the solubility behavior of polynuclear aromatics. Furthermore, the combination of SAFT (in modeling of the fluid phases) and the solid fugacity model (in modeling of the solid phase) was able to predict the pressure-solubility behavior of phenanthrene in which increasing pressure leads to lower solubility.

Before SAFT could be applied to model crude oil systems containing asphaltenes, a lumping scheme needed to be developed to divide the recombined oil into pseudo-components and a characterization scheme needed to be developed to model asphaltenes for use in SAFT. In this work, the recombined oil was modeled as a six-component mixture, with three pseudo-components for the stock-tank oil fraction and three pseudo-components for the separator gas. The average molecular weight and the amount of each sub-fraction were determined from gas-chromatography, saturates-aromatics-resins-asphaltenes fractionation, and gas-oil-ratio information. The SAFT parameters for each sub-fraction (except for the asphaltenes) were obtained from correlations with molecular weight for each class of compounds. The SAFT-predicted densities for the stock-tank oil and the recombined oils agree very well with experimental measurements.

The mixture refractive indices at the onset of asphaltene precipitation during ambient condition titrations (P_{RI}) were used to characterize asphaltene's SAFT parameters; the parameters were optimized so that SAFT would reproduce the mixture's P_{RI} (alternatively the composition of the mixture) at the onset of asphaltene precipitation. If the mechanism responsible for asphaltene precipitation under reservoir depressurization is consistent with the mechanism in titration experiments, thermodynamic models that correctly account for the interaction forces should be able to predict the depressurization results based on

matching the results of the titration experiments. For both the model oil and the stock-tank oil, good agreements were obtained between experimental and fitted P_{RI} even with a binary interaction parameter of zero between asphaltenes and the other species.

For both the model live oil and the recombined oil systems, SAFT predicted asphaltene instability, oil bubble points, and other fluid properties agree well with experiments. Good agreements were obtained between experiment and model predictions on the effects of temperature, pressure, and dissolved gas concentration on asphaltene stability. Furthermore, both SAFT calculated and experiment derived mixture solubility parameters/refractive indices along the asphaltene instability curves were nearly constant at a given temperature.

Since asphaltene is actually a polydisperse collection of molecules, the effects of asphaltene polydispersity on the thermodynamic phase behavior of oil need to be examined. At this stage, we represented polydisperse asphaltene in SAFT using four pseudo-components: the n-C₃₋₅ (the resins), the n-C₅₋₇, the n-C₇₋₁₅, and the n-C₁₅₊ sub-fractions. Using an extension of the monodisperse SAFT asphaltene parameter fitting procedure, we were able to assign a set of SAFT parameters to represent each of the four sub-fractions.

A SAFT investigation into the effects of asphaltene polydispersity showed that the lower molecular weight asphaltenes and resins played a significant role

in stabilizing higher molecular weight asphaltenes in oil. This was despite the inclusion of only dispersion interactions in the SAFT model. Resin's stabilizing effects on polydisperse asphaltene was greatest in the region of incipient asphaltene instability; when sufficient n-alkane precipitants were added, similar amounts of asphaltenes would precipitate regardless of the presence of resins in the oil. An analysis of the mass distribution of the asphaltene sub-fractions in the precipitated phase showed that the largest asphaltenes would precipitate first, followed by the precipitation of smaller asphaltenes upon further oil dilution. It is important to keep in mind that although the SAFT predicted asphaltene mass distributions are qualitatively correct, no experimental data is available at this point to quantitatively validate these numbers.

The underlying hypothesis of our approach is that molecular size and nonpolar van der Waals interactions dominate asphaltene phase behavior in reservoir fluids. A comparison of our monodisperse and polydisperse modeling results with experimental observations supports this hypothesis. An equation of state that can correctly account for the nonpolar van der Waals interactions in titration experiments should be able to also predict asphaltene stability during depressurization.

The next logical step for the research program is to further validate the monodisperse and polydisperse models presented in this work. The asphaltene instability boundaries of at least a few more oils need to be calculated and

compared with experimental results to gauge the model's abilities. It will also be interesting to look at oils whose asphaltene precipitation problems are due to CO₂ injection.

While the monodisperse asphaltene precipitation model is relatively straightforward to implement, two issues need to be resolved for the polydisperse asphaltene model. One should concurrently work on implementing the modifications made in Chapter 9 (so that the equation of state can be made to accept an arbitrary number of asphaltene pseudo-components) and on finding better ways to isolate the various asphaltene pseudo-components for use in SAFT characterization.

Finally, since asphaltene problems are ultimately only problems if they deposit onto pipeline surfaces, the bulk phase precipitation model presented in this work need to be combined with a deposition model. While deposition may or may not occur with asphaltene precipitation, asphaltene precipitation is mostly likely a pre-requisite for deposition.

REFERENCES

- 1 Boussingault, M., *Ann. Chim. Phys.* **64**, 141 (1837).
- 2 Mansoori, G. A., Jiang, T. S., and Kawanaka, S., *Arabian J. Sci. Eng.* **13**, 17-34 (1988).
- 3 Wiehe, I. A. and Liang, K. S., *Fluid Phase Equil.* **117**, 201-221 (1996).
- 4 ASTM, (American Society for Testing and Materials, 1980).
- 5 Wang, J. X., *Predicting Asphaltene Flocculation in Crude Oils*. Ph.D. Thesis, New Mexico Institute of Mining & Technology, 2000.
- 6 Artok, L., Su, Y., Hirose, Y., Hosokawa, M., Murata, S., and Nomura, M., *Energy & Fuels* **13**, 287-296 (1999).
- 7 Speight, J. G. and Plancher, H., in *Intl. Symp. on the Chem. of Bitumens* (1991), pp. 154.
- 8 Wiehe, I. A., *Fuel Sci. Tech. Intl.* **14**, 289-312 (1996).
- 9 Groenzin, H. and Mullins, O. C., *J. Phys. Chem. A.* **103**, 11237-11245 (1999).
- 10 Brandt, H. C., Hendriks, E. M., Michels, M. A. J., and Visser, F., *J. Phys. Chem.* **99**, 10430-10432 (1995).
- 11 Mohamed, R. S., Ramos, A. C. S., and Loh, W., *Energy & Fuels* **13**, 323 (1999).
- 12 Burke, N. E., Hobbs, R. D., and Kashou, S. F., in *Soc. Pet. Eng. Annual Tech. Conf. and Exhib.* (Houston, TX, 1988).

- 13 Hirschberg, A., deJong, L. N. J., Schipper, B. A., and Meijer, J. G., *Soc. Pet. Eng. J.* **24**, 283-293 (1984).
- 14 Kokal, S. L. and Sayegh, S. G., in *Soc. Pet. Eng. Middle East Oil Show* (Bahrain, 1995).
- 15 Haskett, C. E. and Tartera, M., *J. Pet. Tech.* **17**, 387-391 (1965).
- 16 Tuttle, R. N., *J. Pet. Tech.* **35**, 1192-1196 (1983).
- 17 Thaver, R., Nicoll, D. C., and Dick, G., in *Soc. Pet. Eng. Intl. Symp. Oilfield Chem.* (Houston, TX, 1989).
- 18 Lichaa, P. M., in *CIM Conf. on Oil Sands of Canada and Venezuela* (1977), pp. 609-624.
- 19 Adialalis, S., *Investigation of physical and chemical criteria as related to the prevention of asphalt deposition in oil well tubings*. Ph.D. Thesis, Imperial College, 1982.
- 20 Chavez, A. J. L. and Lory, M. A., *Revista del Instituto Mexicano del Petroleo* **23**, 1 (1991).
- 21 Escobedo, J. and Mansoori, G. A., in *SPE Annual Technical Conference and Exhibition* (Dallas, TX, 1995).
- 22 von Albrecht, C., Salathiel, W. M., and Nierode, D. E., *CIM Special Volume* , 55-62 (1977).
- 23 Wu, J., *Molecular Thermodynamics of Some Highly Asymmetric Liquid Mixtures*. Ph.D. Thesis, University of California at Berkeley, 1998.

- 24 Prausnitz, J. M., Lichtenthaler, R. N., and de Azevedo, E. G., *Molecular Thermodynamics of Fluid-Phase Equilibria*, 2nd ed. P T R Prentice-Hall, Inc., 1986.
- 25 Reed, T. M. and Gubbins, K. E., *Applied Statistical Mechanics* Butterworth-Heinemann, 1973.
- 26 Israelachvili, J., *Intermolecular & Surface Forces*, 2nd ed. Academic Press Inc., 1992.
- 27 Khryashev, A. N., Popov, O. G., Posadov, N. A., and Rozental, D. A., *Pet. Chem.* **31**, 601-604 (1991).
- 28 Moore, E. W., Crowe, C. W., and Hendrickson, A. R., *J. Pet. Tech.* **17**, 1023-1028 (1965).
- 29 Chang, C. L. and Fogler, H. S., in *Soc. Pet. Eng. Intl. Symp. on Oilfield Chem.* (New Orleans, LA, 1993).
- 30 Akbarzadeh, K., Ayatollahi, S., Moshfeghian, M., Alboudwarej, H., Svrcek, W. Y., and Yarranton, H. W., in *Amer. Inst. Chem. Eng. Spring National Meeting* (New Orleans, LA, 2002), pp. 218-224.
- 31 Cimino, R., Corraera, S., and Sacomani, P. A., in *Soc. Pet. Eng. Intl. Symp. on Oilfield Chem.* (San Antonio, TX, 1995).
- 32 Nghiem, L. X., Hassam, M. S., Nutakki, R., and George, A. E. D., in *Soc. Pet. Eng. Annual Tech. Conf. and Exhib.* (Houston, TX, 1993), pp. 375-384.

- 33 Leontaritis, K. J. and Mansoori, G. A., in *Soc. Pet. Eng. Intl. Symp. on Oilfield Chem.* (San Antonio, TX, 1987).
- 34 Victorov, A. I. and Firoozabadi, A., *Amer. Inst. Chem. Eng. J.* **42**, 1753-1764 (1996).
- 35 Nghiem, L. X. and Coombe, D. A., *Soc. Pet. Eng. J.* **2** (1997).
- 36 Chung, F., Sarathi, P., and Jones, R., (National Institute for Petroleum and Energy Research, Bartlesville, 1991).
- 37 Burke, N. E., Hobbs, R. E., and Kashou, S. F., *J. Pet. Tech.* **42**, 1440-1446 (1990).
- 38 Firoozabadi, A., *Thermodynamics of hydrocarbon reservoirs* McGraw-Hill, New York, 1999.
- 39 Ting, P. D., Wang, J., Buckley, J. S., Creek, J., Hamammi, A., Hirasaki, G. J., and Chapman, W. G., *In Preparation* (2003).
- 40 Buckley, J. S., Hirasaki, G. J., Liu, Y., von Drasek, S., Wang, J., and Gill, B. S., *Pet. Sci. Tech.* **16**, 251-285 (1998).
- 41 Katz, D. L. and Firoozabadi, A., *J. Pet. Tech.* , 1649 (1978).
- 42 Feynman, R. P., Leighton, R. B., and Sands, M., *The Feynman Lectures on Physics* Addison-Wesley Publishing Co., 1989.
- 43 Vedam, K. and Limsuwan, P., *J. Chem. Phys.* **69**, 4772-4778 (1978).
- 44 *CRC Handbook of Chemistry and Physics*, Vol. , edited by Weast, R. C., Astle, M. J., and Beyer, W. H. (CRC Press, Inc., Boca Raton, 1987).

- 45 Barton, A. F. M., *CRC Handbook of Solubility Parameters and Other Cohesion Parameters*, 2nd ed. CRC Press, Boca Raton, 1991).
- 46 Wang, J. X. and Buckley, J. S., in OCS (Houston, TX, 2001).
- 47 Gray, C. G. and Gubbins, K. E., *Theory of Molecular Fluids I*. Clarendon Press, Oxford, 1984.
- 48 McQuarrie, D. A., *Statistical Mechanics*. Harper & Row Publishers, New York, 1976.
- 49 Smith, J. M. and van Ness, H. C., *Introduction to Chemical Engineering Thermodynamics*, 4th ed. McGraw-Hill, Inc., 1987.
- 50 Peng, D. Y. and Robinson, D. B., *Ind. Eng. Chem. Fund.* **15**, 59-63 (1976).
- 51 Barker, J. A. and Henderson, D. J., *J. Chem. Phys.* **47**, 2856-2861 (1967).
- 52 Barker, J. A. and Henderson, D. J., *J. Chem. Phys.* **47**, 4714-4721 (1967).
- 53 Chapman, W. G., Jackson, G., and Gubbins, K. E., *Mol. Phys.* **65**, 1057-1079 (1988).
- 54 Chapman, W. G., Gubbins, K. E., Jackson, G., and Radosz, M., *Fluid Phase Equil.* **52**, 31-38 (1989).
- 55 Chapman, W. G., Gubbins, K. E., Jackson, G., and Radosz, M., *Ind. Eng. Chem. Res.* **29**, 1709-1721 (1990).
- 56 Wertheim, M. S., *J. Stat. Phys.* **35**, 19 (1984).
- 57 Wertheim, M. S., *J. Stat. Phys.* **35**, 35 (1984).
- 58 Wertheim, M. S., *J. Stat. Phys.* **42**, 459 (1986).
- 59 Wertheim, M. S., *J. Stat. Phys.* **42**, 477 (1986).

- 60 Joslin, C. G., Gray, C. G., Chapman, W. G., and Gubbins, K. E., *Mol. Phys.* **62**, 843-860 (1987).
- 61 Mansoori, G. A., Carnahan, N. F., Starling, K. E., and Leland, T. W., *J. Chem. Phys.* **54**, 1523 (1971).
- 62 Gross, J. and Sedowski, G., *Ind. Eng. Chem. Res.* **40**, 1244-1260 (2001).
- 63 Dickman, R. and Hall, C., *J. Chem. Phys.* **89**, 3168-3174 (1988).
- 64 Gao, J. and Weiner, J. H., *J. Chem. Phys.* **91**, 3168-3173 (1989).
- 65 Gross, J. and Sadowski, G., *Ind. Eng. Chem. Res.* **40**, 1244-1260 (2001).
- 66 Economou, I. G., *Ind. Eng. Chem. Res.* **41**, 953-962 (2002).
- 67 Muller, E. A. and Gubbins, K. E., *Ind. Eng. Chem. Res.* **40**, 2193-2212 (2001).
- 68 Ting, P. D., Joyce, P. C., Jog, P. K., Chapman, W. G., and Thies, M. C., *Fluid Phase Equil.* (2002).
- 69 DIPPR, (AIChE,).
- 70 Huang, S. H. and Radosz, M., *Ind. Eng. Chem. Res.* **29**, 2284-2294 (1990).
- 71 Xu, G., Brennecke, J. F., and Stadtherr, M. A., *Ind. Eng. Chem. Res.* **41**, 938-952 (2002).
- 72 Dlugniewski, J. H. and Adler, S. B., *Chem. E. Symp. Ser.* **35**, 4 (1972).
- 73 *Genetic algorithms in engineering and computer science*, edited by Quagliarella, D., Periaux, J., Poloni, C., and Winter, G. (John Wiley & Sons, New York, 1997).

- 74 Banga, J. R. and Seider, W. D., *Nonconvex optimization and its applications* **7**, 563-584 (1996).
- 75 Rachford, H. H. and Rice, J. D., *J. Pet. Tech.* **4**, 19 (1952).
- 76 Nelson, P. A., *Comp. Chem. Eng.* **11**, 581-591 (1987).
- 77 Mehra, R. K., Heidemann, R. A., and Aziz, K., *Can. J. Chem. Eng.* **61**, 590-596 (1983).
- 78 Ohanomah, M. O. and Thompson, D. W., *Comp. Chem. Eng.* **8**, 163 (1984).
- 79 Michelsen, M. L., *Fluid Phase Equil* **9**, 1-19 (1982).
- 80 Michelsen, M. L., *Fluid Phase Equil* **9**, 21-40 (1982).
- 81 Nocedal, J. and Wright, S. J., *Numerical Optimization* Springer, New York, 1999.
- 82 Baker, L. E., Pierce, A. C., and Luks, K. D., *Soc. Pet. Eng. J.* , 731 (1982).
- 83 Marano, J. J. and Holder, G. D., *Fluid Phase Equil.* **138**, 1-21 (1997).
- 84 Voulgaris, M. E., Peters, C. J., and de Swaan Arons, J., *Intl. J. Thermophys.* **16**, 629-642 (1995).
- 85 McHugh, M. A. and Krukonis, V. J., *Supercritical Fluid Extraction - Principles and Practice*, Butterworths, Boston, 1986.
- 86 Joyce, P. C. and Thies, M. C., *J. Chem. Eng. Data* **43**, 819-822 (1998).
- 87 Joyce, P. C., Gordon, J., and Thies, M. C., *J. Chem. Eng. Data* **45**, 424-427 (2000).

- 88 Peters, C. J., de Swaan Arons, J., Levelt Sengers, J. M. H., and Gallagher, J. S., *AIChE J.* **34**, 834-839 (1988).
- 89 Peters, C. J., de Roo, J. L., and de Swaan, A. J., *Fluid Phase Equil.* **72**, 251-266 (1992).
- 90 Kontogeorgis, G. M., Coutsikos, P., Harismiadis, V. I., Fredenslund, A., and Tassios, D. P., *Chem. Eng. Sci.* **53**, 541-552 (1998).
- 91 Floter, E., de Loos, T. W., and de Swaan Arons, J., *Ind. Eng. Chem. Res.* **37**, 1651-1992 (1998).
- 92 Pan, C. and Radosz, M., *Ind. Eng. Chem. Res.*, **37**, 3169-3179 (1998).
- 93 Huang, S. H. and Radosz, M., *Ind. Eng. Chem. Res.*, **30**, 1994-2005 (1991).
- 94 Benzaghrou, S., Passarello, J. P., and Tobaly, P., *Fluid Phase Equil.* **180**, 1-26 (2001).
- 95 Gregorowicz, J. and de Loos, T. W., *Ind. Eng. Chem. Res.* **40**, 444-451 (2001).
- 96 Reid, R. C., Prausnitz, J. M., and Poling, B. E., *The Properties of Gases & Liquids*, McGraw-Hill, Singapore, 1987.
- 97 Ambrose, D. and Tsonopoulos, C., *J. Chem. Eng. Data* **40**, 531-546 (1995).
- 98 Nikitin, E. D., Pavlov, P. A., and Popov, A. P., *Fluid Phase Equil.* **141**, 155-164 (1997).
- 99 Morgan, D. L. and Kobayashi, R., *Fluid Phase Equil.* **97**, 211-242 (1994).

- 100 API-42, (American Petroleum Institute, University Park, 1940-1966), pp. 1.
- 101 Stephenson, R. M. and Malanowski, S., *Handbook of the Thermodynamics of Organic Compounds*, Elsevier, New York, 1987.
- 102 Joyce, P. C., *Vapor-Liquid Equilibria for Long-Chain Hydrocarbons in Supercritical Alkane Solvents*. Ph.D. Thesis, Clemson University, 1999.
- 103 Chen, S. S. and Kreglewski, A., *Bunsen-Ges. Phys. Chem.* **51**, 1048 (1977).
- 104 Xiong, Y. and Kiran, E., *Polymer* **38**, 5185-5193 (1997).
- 105 Seckner, A. J., McClellan, A. K., and McHugh, M. A., *Amer. Inst. Chem. Eng. J.* **34**, 9-16 (1988).
- 106 Ratulowski, J., Personal Correspondence.
- 107 Coon, J. E., Troth, M., and McLaughlin, E., *J. Chem. Eng. Data* **32**, 233-240 (1987).
- 108 Pan, C. and Radosz, M., *Fluid Phase Equil.* **155**, 57-73 (1999).
- 109 API-708, (American Petroleum Institute, Washington, D.C., 1979).
- 110 Malone, P. V. and Kobayashi, R., *Fluid Phase Equil.* **55**, 193-205 (1990).
- 111 Reamer, H. H., Olds, R. H., Sage, B. H., and Lacey, W. N., *Ind. Eng. Chem.* **34**, 1526-1531 (1942).
- 112 Darwish, N. A., Gasem, K. A. M., and Robinson, R. L., *J. Chem. Eng. Data* **39**, 781-784 (1994).

- 113 Jacoby, R. H., in *Heavy Crude Oil Recovery*, Vol. 76, edited by E. Okandar (NATO, 1984), pp. 1-47.
- 114 Wiehe, I. A., Personal Correspondence.
- 115 Wu, J., Personal Correspondence.
- 116 Elbishlawi, M. and Spencer, J. R., *Ind. Eng. Chem.* **43**, 1811-1815 (1951).
- 117 Kidnay, A. F., Miller, R. C., Parrish, W. R., and Hiza, M. J., *Cryogenics* **15**, 531-540 (1975).
- 118 Reamer, H. H., Sage, B. H., and Lacey, W. N., *Ind. Eng. Chem.* **42**, 534 (1950).
- 119 Grauso, L., Fredenslund, A., and Mollerup, J., *Fluid Phase Equil.* **1**, 13-26 (1977).
- 120 Messow, U. and Engel, I., *Z. Phys. Chem.* **258**, 798 (1977).
- 121 Barton, A. F. M., *Handbook of Solubility Parameters & Other Cohesion Parameters*, 2nd ed. CRC Press, Boca Raton, 1991.
- 122 Azarnoosh, A. and McKetta, J. J., *J. Chem. Eng. Data* **8**, 494-496 (1963).
- 123 Miller, P. and Dodge, B. F., *Ind. Eng. Chem.* **32**, 434-438 (1940).
- 124 Glanville, J. W., Sage, B. H., and Lacey, W. N., *Ind. Eng. Chem.* **42**, 508 (1950).
- 125 Yarranton, H. and Masliyah, J. H., *AIChE J.* **42**, 3533-3543 (1996).
- 126 Larsen, J. W. and Li, S., *Energy Fuels* **9**, 760-764 (1995).
- 127 Jog, P. K. and Chapman, W. G., *Macromolecules* **35**, 1002-1011 (2002).

- 128 Boulougouris, G. C., Voutsas, E. C., Economou, I. G., Theodorou, D. N., and Tassios, D. P., *J. Phys. Chem. B* **105**, 7792-7798 (2001).
- 129 Voutsas, E. C., Boulougouris, G. C., Economou, I. G., and Tassios, D. P., *Ind. Eng. Chem. Res.* **39**, 797-804 (2000).
- 130 Economou, I. G., Heidman, J. L., Tsonopoulos, C., and Wilson, G. M., *AIChE J.* **43**, 535-546 (1997).
- 131 Dhima, A., de Hemptinne, J. C., and Jose, J., *Ind. Eng. Chem. Res.* **38**, 3144-3161 (1999).
- 132 Kobayashi, R. and Katz, D., *Ind Eng Chem* **45**, 440-451 (1953).
- 133 Tsonopoulos, C., *Fluid Phase Equil.* **156**, 21-33 (1999).
- 134 Nemethy, G. and Scheraga, H. A., *J. Chem. Phys.* **36**, 3382-3400 (1962).
- 135 Kell, G. S., in *Water, a comprehensive treatise*, Vol. 1, edited by F. Franks, Plenum Press, New York, 1972, pp. 363-404.
- 136 Poole, P. H., Sciortino, F., Grande, T., Stanley, H. E., and Angell, C. A., *Phys. Rev. Lett.* **73**, 1632-1635 (1994).
- 137 Zudkevitch, D. and Joffe, J., *AIChE J.* **16**, 112-119 (1970).
- 138 Huron, M. J. and Vidal, J., *Fluid Phase Equil.* **3**, 255 (1979).
- 139 Economou, I. G. and Tsonopoulos, C., *Chem. Eng. Sci.* **52**, 511-525 (1997).
- 140 Yakoumis, I. V., Kontogeorgis, G. M., Voutsas, E. C., Hendriks, E. M., and Tassios, D. P., *Ind. Eng. Chem. Res.* **37**, 4175-4182 (1998).

- 141 Truskett, T. M., Debenedetti, P. G., and Sastry, S., *J. Chem. Phys.* **111**, 2647-2656 (1999).
- 142 Jackson, G., Chapman, W. G., and Gubbins, K. E., *Mol. Phys.* **65**, 1-31 (1988).
- 143 Soper, A. K. and Phillips, M. G., *Chem. Phys.* **107**, 47-60 (1986).
- 144 Wertheim, M. S., *J. Chem. Phys.* **87**, 7323-7331 (1987).
- 145 Wertheim, M. S., *Phys. Rev. Lett.* **10**, 321-323 (1963).
- 146 Thiele, E. J., *J. Chem. Phys.* **38**, 1959 (1963).
- 147 Baxter, R. J., *Aust. J. Phys.* **21**, 563 (1968).
- 148 Chang, J. and Sandler, S. I., *Mol. Phys.* **81**, 735-744 (1994).
- 149 Verlet, L. and Weis, J. J., *Phys. Rev. A* **5**, 939-952 (1972).